이학박사 학위논문

Supernova Progenitor System from Intensive Monitoring Survey of Nearby Galaxies

가깝고 밝은 은하들에 대한 집중 모니터링 탐사연구를 통해 본 초신성의 기원

2021년 8월

서울대학교 대학원

물리·천문학부 천문학전공

최 창 수

Supernova Progenitor System from Intensive Monitoring Survey of Nearby Galaxies

지도교수 임 명 신

이 논문을 이학박사 학위논문으로 제출함

2021 년 8 월

서울대학교 대학원

물리천문학부 천문학전공

최 창 수

최창수의 박사 학위논문을 인준함

2021 년 8 월

위 원 장 구 본 철

부위원장 임 명 신

위 원 윤 성 철

위 원 박 수 종

위 원 고 종 완

Supernova Progenitor System from Intensive Monitoring Survey of Nearby Galaxies

by

Changsu Choi
(changsu@astro.snu.ac.kr)

A dissertation submitted in partial fulfillment of the requirements for the degree of

Doctor of Philosophy

in

Astronomy

in

Astronomy Program
Department of Physics and Astronomy
Seoul National University

Committee:

Professor	Bon-Chul Koo
Professor	Myungshin Im
Professor	Sung-Chul Yoon
Professor	Soojong Pak
Professor	Jongwan Ko

ABSTRACT

A supernova (SN) is the ending stage of a star, a stellar catastrophe. It is one of the most powerful event in the Universe. Much of its physical properties has been revealed thanks to former elaborated efforts in observations and theories. But the whole picture of SNe is not completed, especially on the progenitor star of SNe. Early light curves of supernovae hold keys for understanding on their progenitor star. IMSNG is designed to catch the shock-heated emission right after SN explosion imprinted in early time light curve. In this thesis work, I present establishment of observational systems of IMSNG. Among the SNe caught early in IMSNG, the results from analysis of the early light curves of a SN Ia, SN 2018kp and two SNe Ic, SN 2017ein and SN 2017gax are presented.

First, the characteristics and the performance of the new CCD camera system, SNUCAM-II (Seoul National University CAMera system II) are introduced. SNUCAM-II was installed on the Lee Sang Gak Telescope (LSGT) at the Siding Spring Observatory in 2016. SNUCAM-II consists of a deep depletion chip covering a wide wavelength from 0.3 μm to 1.1 μm with high sensitivity (QE at $> 80\%$ over 0.4 to 0.9 μm). It is equipped with the SDSS *ugriz* filters and 13 medium band width (50 nm) filters, enabling us to study spectral energy distributions (SEDs) of diverse objects from extragalactic sources to solar system objects. On LSGT, SNUCAM-II offers 15.7 $\times$ 15.7 arcmin field-of-view (FOV) at a pixel scale of 0.92 arcsec and a limiting magnitude of $g = 19.91$ AB mag and $z = 18.20$ AB mag at 5 σ with 180 sec exposure time for point source detection.

Second, We present optical observation of the nearby Type Ia SN 2018kp. SN 2018kp is a normal type Ia supernova discovered at NGC 3367 on 2018 January 24. As a main target of the Intensive Monitoring Survey of Nearby Galaxies (IMSNG project), NGC 3367 has been monitored with a high cadence (< 1 day) at the time of discovery, providing us with a valuable early light curve. From the early optical light curve analysis, we found that single power law model of the fire ball can explain early light curve

behavior and the little SHE emission evidence in the very early data, which suggest that SN 2018kp progenitor system is made with an exploding white dwarf and a companion star of around a few solar radius. This rules out a large size companion star like red giant star as a companion star, but still favors a single degenerate progenitor. We derive physical parameters and confirm SN 2018kp as normal SN Ia. The distance to host galaxy from long term light curve fitting of our data is 50 Mpc consistent with that of Tully-Fisher method.

Third, Type Ic supernovae are core-collapse supernovae without hydrogen and helium absorption lines in their spectra. The lack of the hydrogen and helium lines has been commonly attributed as a result of the explosion of the hydrogen- and helium-envelope stripped star. The Wolf-Rayet stars are compelling progenitor star for their efficient mass loss mechanism. But, direct observational evidence for SN Ic progenitor stars has been lacking. Moreover, recent works have suggested that deficiency the helium line in SN Ic may be just due to inefficient nickel mixing. The models suggest that the color evolution of the SN Ic early light curve can indicate the nickel mixing degree. And the progenitor star may have hidden helium contents. SN 2017ein and SN 2017gax are carbon-rich type Ic supernovae that occurred in NGC 3938 and NGC 1672 in 2017. IMSNG succeeded in catching the early optical light curve since within one day of the explosion. Analysis of this early light curve data reveals no strong shock-heated emission in early stage, and constrain the size of the progenitor to be compact (< 3 $R_{\odot}$). Furthermore, the early color evolution of two SNe are rather unique in a sense that it starts with a red color, becomes blue, and reddens again. It suggests that nickel mixing is weak or moderate for these SNe. In such a case, a small of amount of Helium could have existed around the progenitor system.

Taken the results together, early light curves obtained from IMSNG project give us the meaningful insight on the progenitor star of SNe. In the large telescope era, this results prove the merit of small telescope network.

Keywords: cosmology: observations – star: evolution – supernova: explosion– telescope: CCD camera – transient: survey

Student Number: 2009-30868

Contents

List of Figures

List of Tables

Chapter 1

Introduction

1.1 Supernova

A supernova (SN) is the ending stage of a star, a stellar catastrophe. It is one of the most powerful event in the Universe, whose peak luminosity is comparable to that of a galaxy. Almost all research fields in astronomy are connected with SNe. They allow us to investigate the inner structure of exploding stars. By studying them we can attain new insights on the stellar evolution. Supernovae play an important role in chemical evolution of the Universe. Heavy elements of higher atomic number than helium are synthesized in pre-explosion and explosion moments. In physical evolution of galaxies, SNe are a significant powerhouse. Long-lived SNRs (supernova remnants) like Cas A are formed by sweeping circumstellar (CSM) and interstellar matter (ISM). SNe may drive galactic winds and stimulate star-formation with the energy in the galaxy. Supernovae are very luminous, can be served as extragalactic distance indicator. Cosmic expansion history and hubble constant (H_0) were determined by the estimated distance to the extragalaxy hosting supernovae, supporting the accelerated cosmic expansion and the existence of dark energy (Riess et al. 1998; Perlmutter et al. 1999).

There are abundant historical records of SNe (SN 1006, SN 1054, SN 1181, SN1572; Tycho, SN 1604; Kepler etc,.) lasting from 1000 years ago. In the modern era, Badde and Zwicky identified a class of 10^5 times brighter "novae" (means " New Star") and called

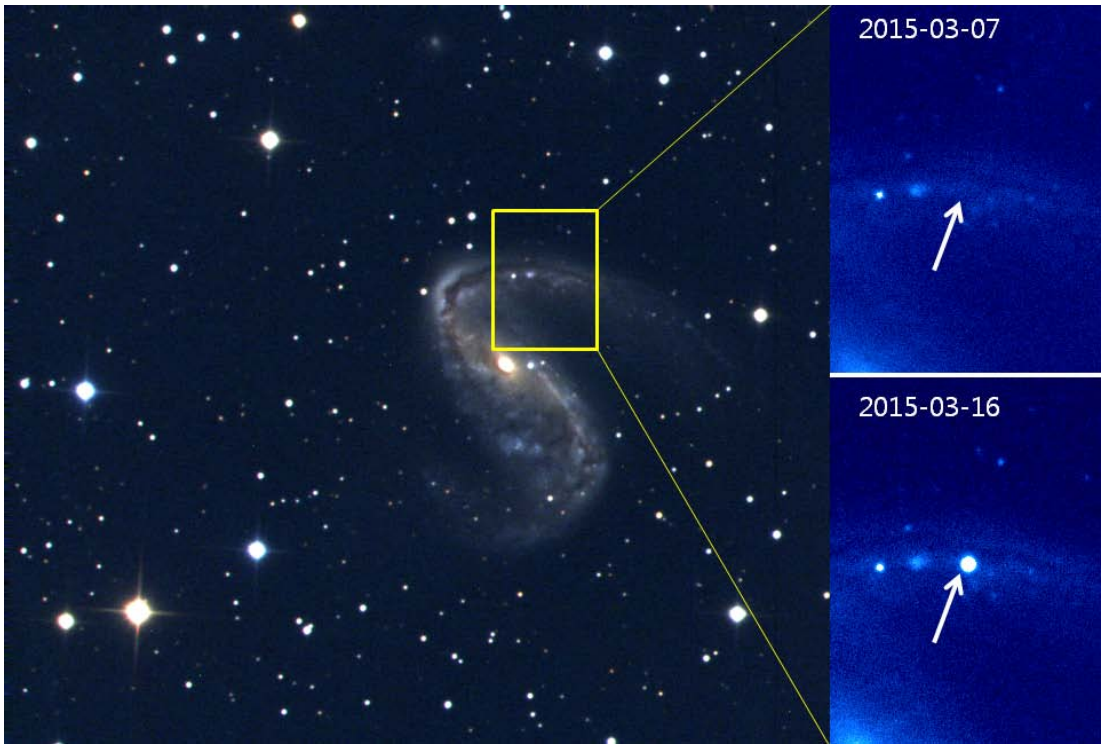

Figure 1.1. BVR composite image of NGC 2442 and the location of SN 2015F before and after its emergence (LSGT, *R*-band). Adopted from Im et al. (2015b)

them "Supernovae" after Lundmark. Basically they are transient objects, brightened and dimmed in short time scale, and it is hard to predict the explosion. However, recent technology developments enable us to capture them in large number and to gather extensive photometric and spectroscopic data. Figure 1.1 shows the moment of capturing SN 2015F in NGC 2442 via modern supernova search (Im et al. 2015b).

1.1.1 Classification of Supernova

The observational classification of SNe is based on the spectra when the SN luminosity arrived at peak, optically thick, photospheric status. Minkowski (1941) classified SNe as either type I and type II depending on whether they show H feature in their spectrum (type II SN, or SN II) or no such feature (type I SN, or SN I). More specific classifications are extended to Si lines, He lines and width of profiles. Figure 1.2 describes the brief

scheme of supernova classification.

The SN Ia show ionized Silicon feature around 6000Å. SNe Ib/c show no hydrogen. SNe Ib have HeI lines, SNe Ic do not. SNe IIb have transition from H-rich to He-rich spectra, meaning that their stellar envelopes are expelled before explosion. SN Ib/c and IIb are also referred as stripped envelope supernovae (SE SNe) (Clocchiatti & Wheeler 1997). SNe IIn and SNe Ibn have narrow emission lines. From late time light curve slope, if the light curve has a plateau phase, then it is classified SNe IIP, if the light curve linearly drops, it will be SNe IIL. In Figure 1.3, various light curve morphologies according to SN types are shown. There are more subclasses added recently, SN Ic-BL has SNe Ic with broad line width of high velocity and are generally associated with Gamma Ray Bursts (GRBs) and X-Ray Flashes (XRFs). The SNe that have extremely high luminosity ($M_{B,Peak} < -21$ mag) are classified as the superluminous supernovae (SLSNe; Gal-Yam (2012)).

1.1.2 Physical properties of SNe

Their physical interpretation and classification are related to their progenitor stars and explosion mechanisms. SN Ia is the thermonuclear explosion of a carbon-oxygen (CO) white dwarf (WD) star. At the end of low mass star ($M < 8M_{\odot}$) evolution, WD is formed. When it comes to Chandrasekhar mass ($M_{Ch} \sim 1.4M_{\odot}$) limit by mass accretion from companion star or merger of two WD, thermonuclear explosion can be triggered. Heavy elements of iron group are produced, kinetic energy of 10^{51} erg is released. Its luminosity is powered by the radioactive decay from Nickel to cobalt (half life 6.1 days). Later, cobalt to iron decay (half life 77.3 days) dominates light curve after peak. Since optical light curves of normal SNe Ia are homogeneous, duration and luminosity are correlated each other (Phillips relation; Phillips et al. 1999), SNe Ia can be standard candles. Other types, SN Ib/c, SN II and their subtypes are Core-Collapse (CCSNe) explosion of massive stars ($8M_{\odot} < M < 120M_{\odot}$). They are believed to be gravitational collapse of the iron core of massive star (Smartt 2009). However, the light curves and spectra are heterogeneous. From H-burning, massive stars evolve to form

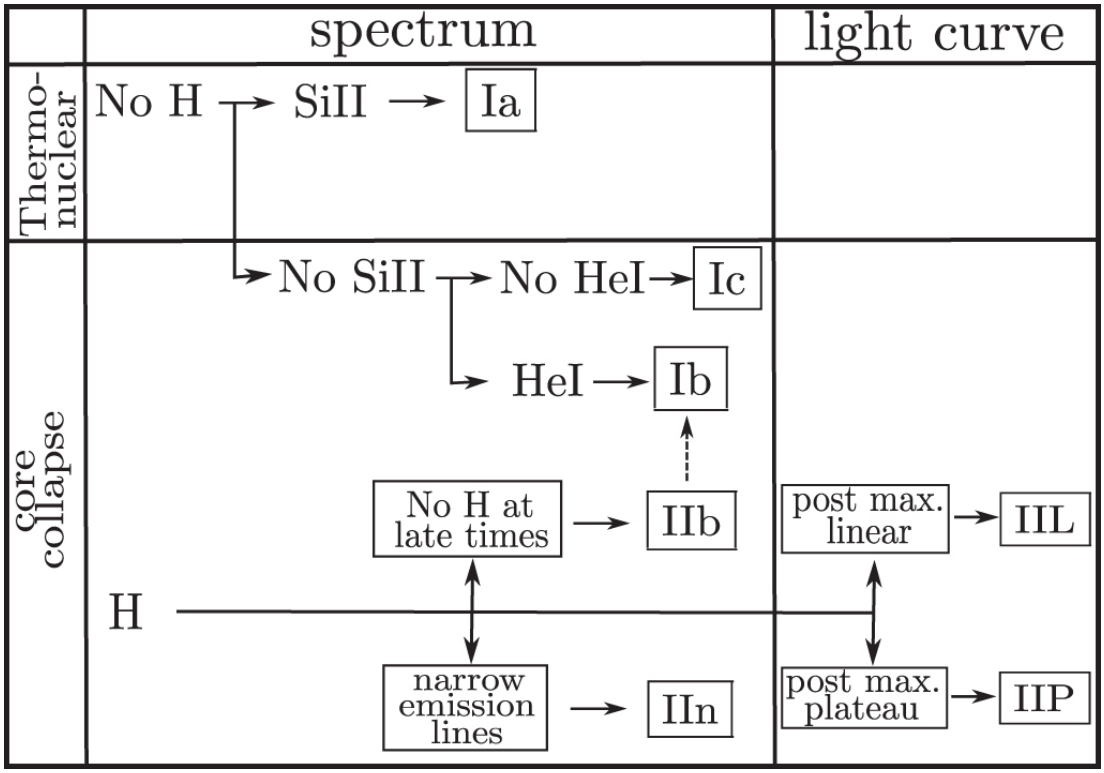

Figure 1.2. Scheme of supernova classification with spectral features and light curve shapes, Adopted from Coelho et al. (2015)

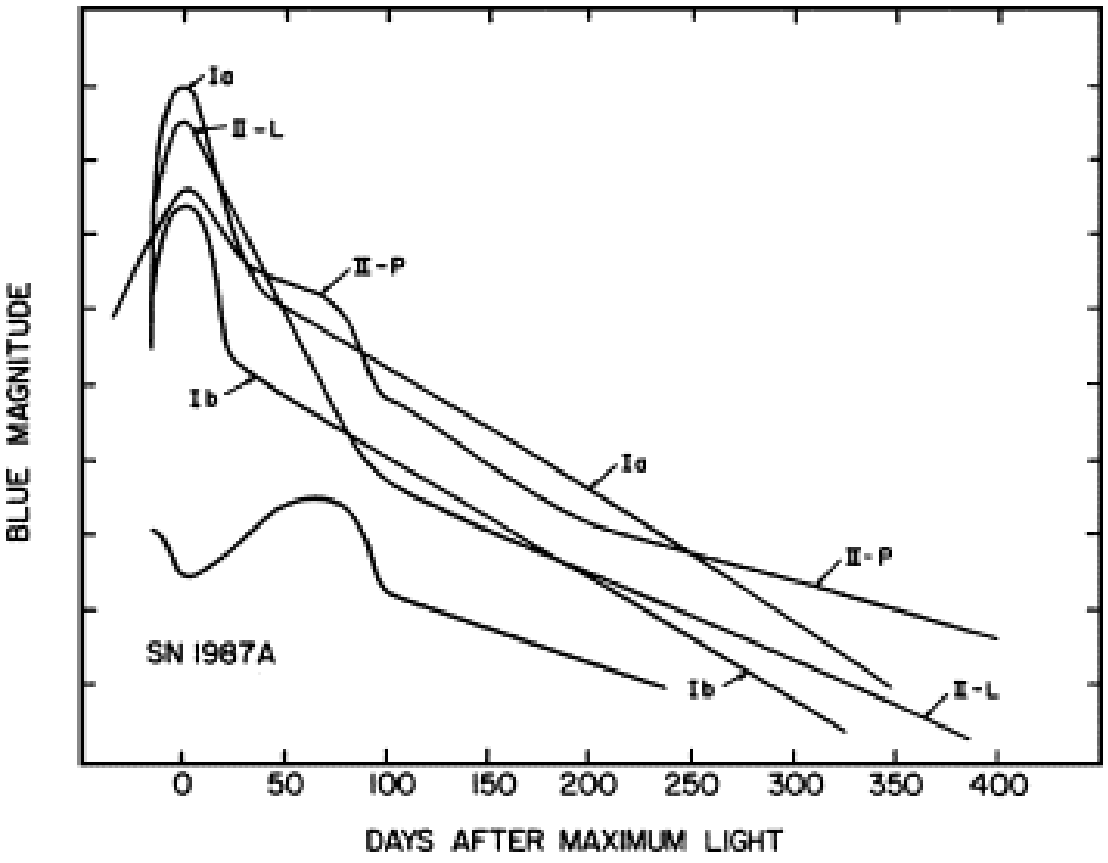

Figure 1.3. Light curves of each SN Types, Adopted from Wheeler & Harkness (1990)

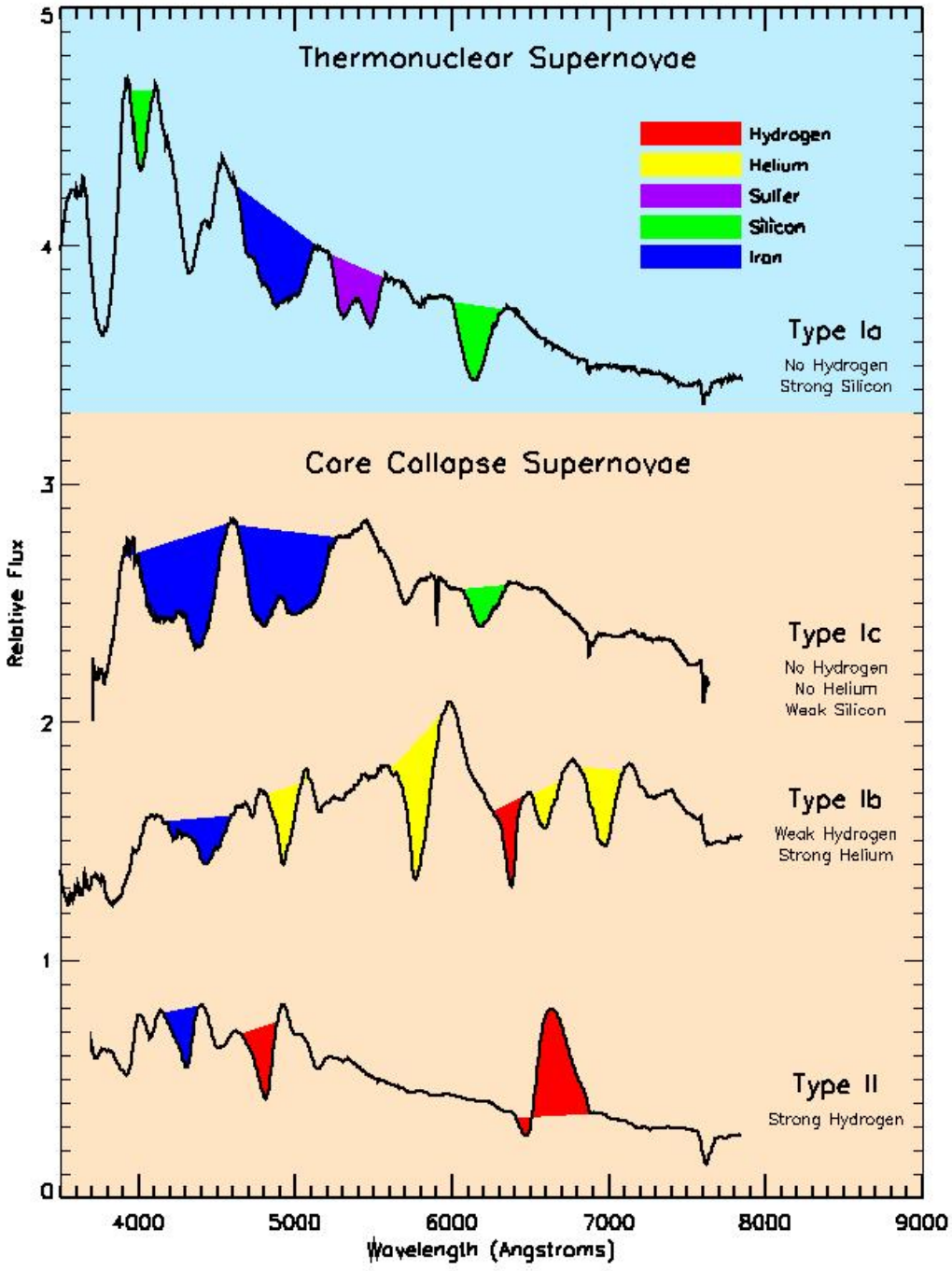

Figure 1.4. Early time SN spectra. Courtesy of D. Kasen

shell structure of intermediate elements like carbon, oxygen, magnesium and silicon. By electron capture, when there is no matter to burn for sustaining the pressure against gravity, gravitational collapse occurs. The first visible signals of CCSNe come from shock Break-out (SBO) For 1987A, its duration of SBO was estimated of 180s (Ensman & Burrows 1992). This SBO makes double peak shapes in light curves. Ni-Co-Fe radioactive decay powers CCSNe luminosity too.

SESNe (IIb, Ib/c) light curves resemble those of SNe Ia. But no strong relation between width and peak luminosity was found. SESNe lack of H lines in spectra and show ionized absorption lines from photosphere, meaning the presence of low ionized elements. Normal SNe Ib/c have 0.1 $M_{\odot}$ Ni mass from bolometric light curve, but GRB related or Broad line showing SNe Ib/c have almost 2-3 times Ni mass. The absence of hydrogen or helium (SNe Ic) indicates that the progenitor star must lose its matter prior to explosion via mass loss or binary interaction.

Type II SNe are known to be explosion of Giant Stars or super giant stars from a few direct detection of progenitor stars (Smartt 2009). RSG (Red Super Giant) stars with thick H-envelop are candidate of SN IIP. SN IIP and SN IIL are divided for light curve shapes, which come from Ni decay and the propagation of shock wave through the ejecta or matter after peak. The energy injected in hydrogen envelop of SN IIP slowly diffuses out and makes a plateau in light curve. SN IIL already has lost its hydrogen envelop, the energy radiates faster making linear slope in light curve. Type IIn SNe show narrow hydrogen emission lines attributed to slow moving CSM (few hundred km s^{-1}).

1.2 Progenitor Stars of Supernovae : Current Expectations

Our understanding of SNe is still far from the whole picture. The progenitor systems of SNe are the one of the biggest pieces of the puzzle. Issues on the progenitor systems of two major classes, thermonuclear and core-collapse SNe are described in the following

subsections.

1.2.1 Thermonuclear Supernovae

There are two broad classes of SNe Ia progenitor scenario, Single-Degenerate (SD) and Double-Degenerate (DD) scenario. Two scenarios focus on how to explode CO WD by growing its mass to M_{Ch}. SD scenario takes the way of accretion from a non-degenerated star (Whelan & Iben 1973). DD scenario suggest the merging of two WDs in a close binary system (Tutukov & Yungelson 1981).

1. Single-Degenerate scenario

   In this model, a non-degenarated companion star can be a main sequence star, a subgiant star or a red giant star. The mass accretion rate plays the biggest role here. Allowed accretion rate range is narrow for stable hydrogen burning on the WD surface ($\dot{M} = 10^{-7}\ M_{\odot}$ for $0.8 M_{\odot}$ WD, $\dot{M} = 5 \times 10^{-7}\ M_{\odot}$ for $1.4\ M_{\odot}$ WD, Maoz et al. 2014). If the accretion rate is lower than that, a nova eruption can happen causing the WD to lose its matter slowly (Yaron et al. 2005). On the other hand, the binary system may evolve into common envelope system, losing angular momentum and accelerating the accretion, possibly leading to rapid accretion that results in the thermonuclear explosion of the WD.

   This scenario has been favored traditionally. It gives natural explanation of the explosion path, can explain observables of light curve, and the observed color and the relative abundance of elements. But recently, this scenario was not applied in the case of SN 2011fe and SN 2014J which limit the companion star sizes to be small, though this scenario is not entirely ruled out for other SNe Ia (Bloom et al. 2012; Margutti et al. 2014).

2. Double-Degenerate scenario

   In a binary system with a close orbit, two WDs get closer by losing orbital energy in gravitational wave emission. They can merge in forms of tidal disruption, accretion to secondary WD or direct collision, which gives leads to the supernova explosion.

This model is consistent with the lack of hydrogen feature, X-ray emission, and radio emission in many SNe Ia (Chomiuk et al. 2012). Also, the long delay time, the merger rate of galactic WD binary, and non-surviving companion stars in some SNRs can be well explained with this scenario. However, it is not clear that how merging of WDs can lead to the explosion.

1.2.2 Core-Collapse Supernovae

Unlike SNe Ia, some of the nearby CCSNe progenitor stars have been detected directly from pre-explosion image. SN 1987A has a blue supergiant star of initial mass 14-20 $M_{\odot}$ (Smartt 2009). One of SNe IIb, SN 1993J progenitor system was revealed as a binary with stripped supergiant explosion (Maoz et al. 2014). With *HST* and ground telescopes, the progenitor of SNe II are detected often, specially SNe IIp has the largest fraction of pre-explosion discovery cases. These pieces of evidence show that SNe II progenitors are massive stars such as red, yellow and blue giant stars (Smartt 2009). The absence of SN II progenitors with mass larger than 17-18 $M_{\odot}$ is a major issue called the red supergiant problem (Smartt 2015)). According to the Salpeter initial mass function (Salpeter 1955), currently 30% of SN II progenitors are missing over the 17-18 $M_{\odot}$ limit. This may be caused by a direct collapse to a black hole of higher mass progenitor.

The Wolf-Rayet (WR) stars are known as the progenitor star of SN Ib/c for lack of hydrogen and helium lines in SNe Ib/c spectra (Filippenko 1997). WR stars are at an evolved stage of massive stars ($M > 25\ M_{\odot}$), they have strong winds (a few thousand km/s), large mass loss rates ($\sim 10^{-5}\ M_{\odot}/yr$) and strong emission lines of carbon, nitrogen and oxygen (Crowther 2007). Their outer envelops are stripped, effectively causing SN Ib/c features. However, recent studies indicated that a single WR progenitor only cannot account for all SN Ib/c numbers, and the binary evolution of low mass stars have become a favored channel for SNe Ib/c (Podsiadlowski et al. 1992; Eldridge et al. 2013; Yoon 2017). The growing pieces of evidence such as high binary fraction (Sana et al. 2012) or low ejecta masses (Lyman et al. 2016), suggest that low mass binary

channel is highly possible for SN Ib/c.

1.3 Detection of SN Progenitor stars : Observational Efforts So far

1.3.1 Direct Imaging of Progenitor Star

The most reliable method of progenitor detection is examination of pre-explosion image on supernova site (Smartt 2009). Mostly *HST* or ground telescope with high resolution data is used. After registration of images, one may locate progenitor candidate, confirm existence of progenitor and measure luminosity to constrain initial mass of progenitor star. In this way, a few dozens of SN II progenitor are found to have initial mass of 10-17 $M_{\odot}$. Though it is powerful method, there are many obstacles to it. There must be existing pre-explosion images of required depth of high resolution. In most cases, it is hard to find pre-explosion images of SNe in the archive. Even if a pre-SN image exist, there are more difficulties. An estimate of stellar mass depends on color-magnitude diagram, which involves many uncertainties. We need correct extinction values of Milky Way and host galaxy of SN first. Fitting SEDs is not simple because diverse temperature and radii can result in different SEDs. Moreover, stellar evolution models for inferring initial mass of progenitor star are sensitive to various parameters such as metallicity, multiplicity, rotation and so on. This method is limited to relatively local region, for example, a normal RSG SN progenitor can be resolved at maximum 20 Mpc. So this method can not be used for distant SNe. In this point of view, Indirect approach to detection of progenitor star is good alternative to probe progenitor star and explosion mechanism.

1.3.2 Shock Breakout and Shock Heated Emission

One can collect very important information on the progenitor system from very early time observation of SNe. Early time luminosity is dominated by shock break out (SBO) and shock cooling. The radius and internal structure of progenitor star can be con-

strained so that progenitor properties, explosion mechanism and last stage of evolution of progenitor can be revealed. After explosion, when generated shock touches the edge of star, it breaks out and make flash of X-ray or Ultraviolet. Its radiation is dependent on the size and density of progenitor star (Colgate & McKee 1969; Nakar & Sari 2010; Rabinak & Waxman 2011)). SBO emission may be extended to optical wavelength if progenitor star is large. SN 2008D, SNLS-04D2dc, PS1-13arp has been detected SBO emission in X-ray and UV (Schawinski et al. 2008; Soderberg et al. 2008; Gezari et al. 2015). SBO detection in optical is reported in KSN 2011d (Garnavich et al. 2016). However the flash has short time scale (a few sec - an hour).

Meanwhile, Shock cooling after SBO continued much longer and produces shock heated emission. As ejected matter expands and cools, SHE radiates. The companion star hit by SN ejecta also can make SHE too (Kasen 2010). SHE is very sensitive to the progenitor size just before explosion (Chevalier & Fransson 2008; Nakar & Piro 2014). SHE can last from days to a week and this can be used to constrain size of progenitor star for both of SN Ia and CCSNe. This feature is shown as excess or peak in early time light curve or color curve. A number of cases of SHE detection have been studied for identification of progenitor systems of SNe (Type Ia SN 2011fe; Nugent et al. 2011, Type Ib SN 1999ex; Stritzinger et al. 2002, Type IIb 2011bh; Arcavi et al. 2011 and so on). By obtaining early light curve, one can approach to progenitor system effectively even without pre-explosion image data.

1.4 IMSNG

Intensive Monitoring Survey of Nearby Galaxies (IMSNG) is targeted monitoring observation program to constrain the SN progenitor systems by inferring their sizes. With high cadence monitoring of the nearby galaxy which is highly probable to host supernova, IMSNG is designed to catch the shock-heated emission right after SN explosion (Im et al. 2019).

1.4.1 Target Selection

The list of IMSNG target galaxies is shown in Table 1.1. On average SN rate is of order of 0.01 SN yr^{-1} (Graur et al. 2017). To increase probability of catching SN, target galaxies are selected by criteria of SFR. It is known that high SFR and high stellar mass yield high SN rate in both SNe Ia and CCSNe (Botticella et al. 2012). NUV is good proxy for SFR. M_{NUV} = -18.4 AB mag cut corresponds to SFR = 1 $M_{\odot}$ yr^{-1}. And in order to detect SHE of small progenitor SN, distance to target galaxy is limited to 50 Mpc. Based on Rabinak & Waxman (2011) and Kasen (2010), IMSNG can resolve 1 $R_{\odot}$ size progenitor star at 50 Mpc. Another criteria is Galactic latitude for the purpose of avoiding Galactic extinction and contamination from Galactic stars. 60 galaxies were selected from Galaxy Evolution Explorer (GALEX) catalog (Gil de Paz et al. 2007; Bai et al. 2015), including two galaxies NGC 6946, ESO 182-G10 of prolific SN rate for exception. Figure 1.6 demonstrates predicted early light curve model of various progenitor size.

1. M_{NUV} < -18.4 AB mag
2. D < 50 Mpc
3. b > 20 deg

1.4.2 Telescopes and Observations

IMSNG use global network of 1-m class telescopes. It is necessary to cover different time zone for high monitoring. There are $\sim$ 10 telescopes in the network, size ranges from 0.25m to 1.5m diameter. The largest FOV of 2.35 ° × 2.35 °. The shortest time cadence is 2 hours between Korea and Australia. The exposure time vary among facilities, are set to the depth of 19.5 mag in R-band for point source. $BVRI$, $griz$ and medium band width filter are equipped, typically B, R, r -band filter are used for monitoring. When follow-up observation begins, other band filter observation is carried out together. Data acquisition and calibration process for one night is done by next day time. All raw data

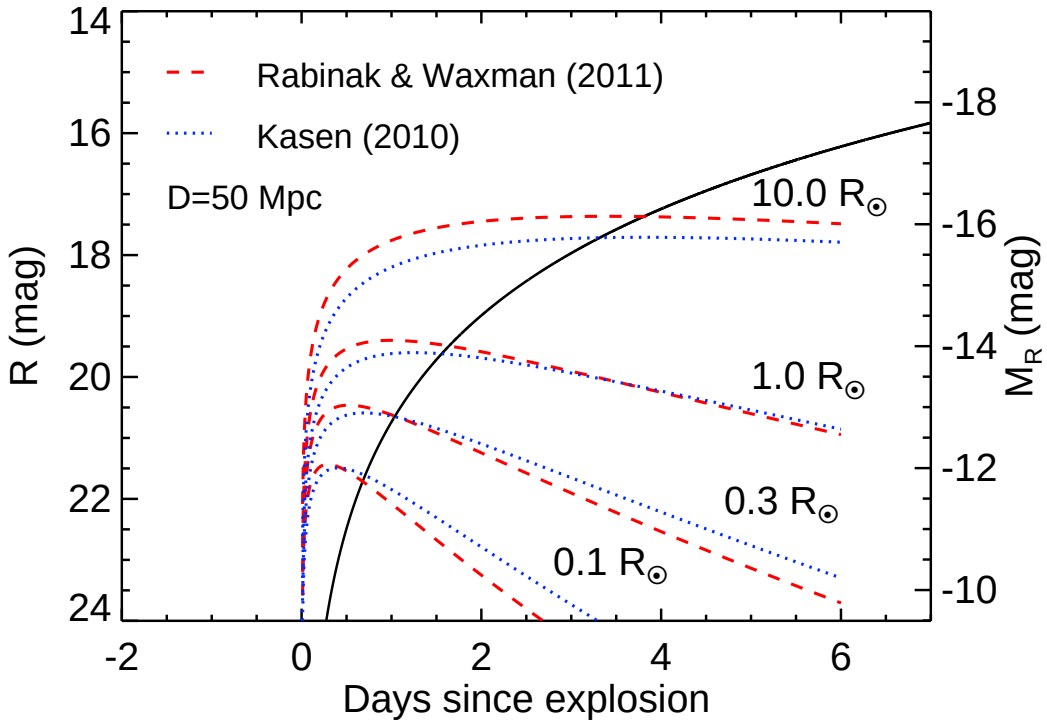

Figure 1.5. Early time light curve models of IMSNG prediction. Adopted from Im et al. (2019)

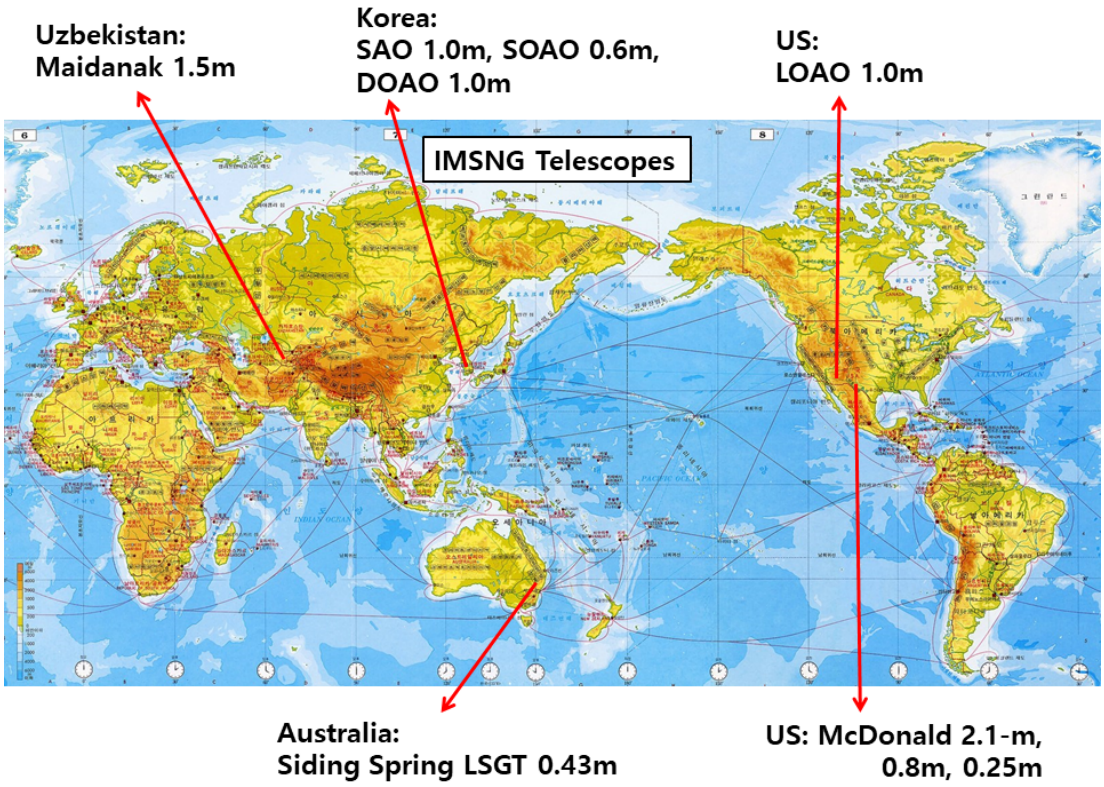

Figure 1.6. Global network of IMSNG telescopes. Adopted from Im et al. (2019)

is calibrated for Bias, Dark, flat, cosmic ray removal first, registration and stacking are following. After Calibrations, image subtraction and transient detection will be next step using reference frames made of former good quality images. Table 1.2 describes the detailed information of telescopes consisting of IMSNG network.

1.4.3 Performances

Currently, large telescopes ($>$ 8-m) are common, but small telescopes are still valuable for specialized study such as follow-up or long term monitoring. Large FOV and available time of small telescopes are strong points for transient observation. IMSNG started from 2014, there are 18 SNe occured in IMSNG galaxies up to 2019 Im et al. (2019). This number is somewhat larger than predicted SN rate 0.053 SN /yr^{-1}. In 2015, using LSGT, (Lee SANG GAK Telescope, Siding Spring Observatory, Australia, Im et

al. 2015a) the early light curve of SN 2015F was obtained and analyzed to study the progenitor system of Type Ia SN 2015F (Im et al. 2015b). Not only SNe but also other transients are aimed too. IMSNG galaxy has 22 AGNs (Active Galatic Nuclei) in list. IMSNG facilities carry out the monitoring observation of AGN reverberation mapping (Kim et al. 2019). Stellar transient like luminous blue variable (LBV) or luminous red nova (LRN) from evolved star are one of good object can be covered by IMSNG, since long term monitoring of high cadence can provide rich light curve that can provided information on the progenitor and physical origins. IMSNG is also well configurated for Gamma Ray Burst afterglow follow-up observation. IMSNG has served as one of important observing facilities for GW170817, gravitational wave (GW) electro-magnetic counter part too (Troja et al. 2017; Im et al. 2017). In the multi-messenger astronomy era, the follow-up optical observation of GW and neutrino sources can be conducted well by IMSNG with wide field of view and global telescope network. Besides, for solar object, variable star and even educational observation, IMSNG has proved its usefulness.

1.5 Description of the Thesis Work

In my thesis work, we established observational systems that can perform IMSNG, and performed the SNe monitoring program. Among the SNe caught early in IMSNG, I studied the early light curves of a SN Ia, SN 2018kp (Figure 1.7), and two SNe Ic, SN 2017ein and SN 2017gak (Figure 1.8 and 1.9) in IMSNG targets to understand the progenitor stars of these supernovae.

For IMSNG, I have performed many nights of observations using the IMSNG facilities such as the Maidanak 1.5-m, the LOAO 1-m, and the McDonald 30-inch, WIT, and 2.1-m telescopes, and derived an early image analysis pipeline to analyze the IMSNG data. Also, we installed the Lee Sang Gak Telescope (LSGT) in the Siding Spring Observatory in 2014 October, and I have been in charge of the operation of LSGT for several years since its installation. Shortly after the LSGT installation, I took a lead on upgrading the LSGT's imaging camera to the SNUCAM-II, which is a high per-

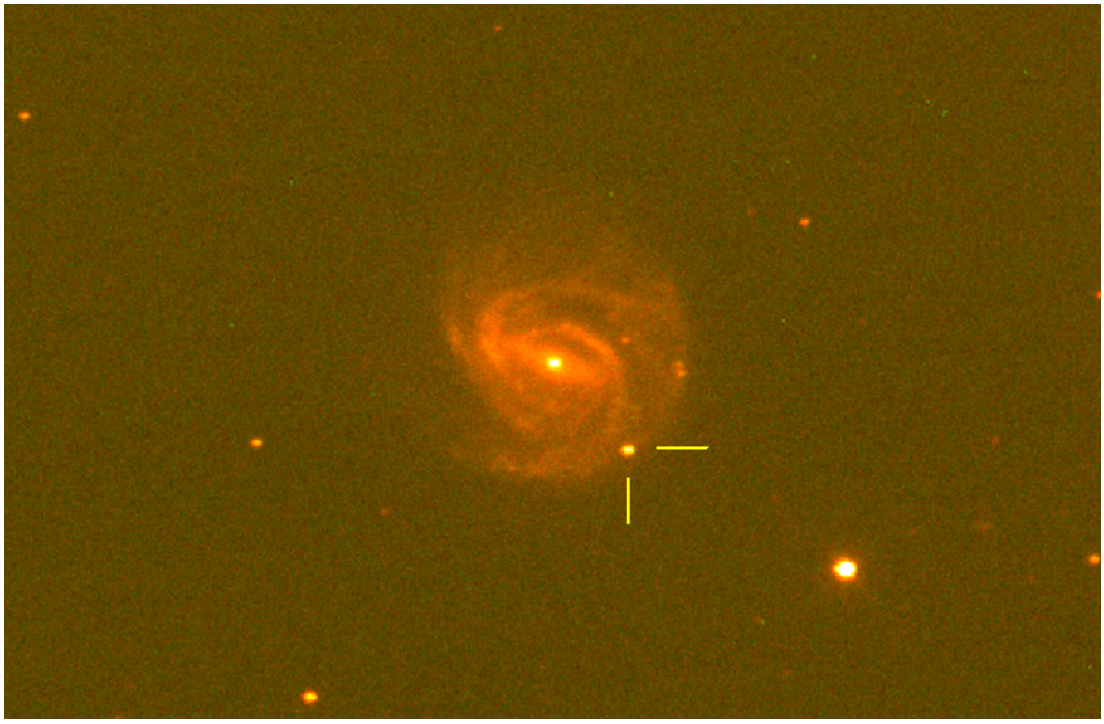

Figure 1.7. Color image of SN 2018kp in NGC 3367 from IMSNG.

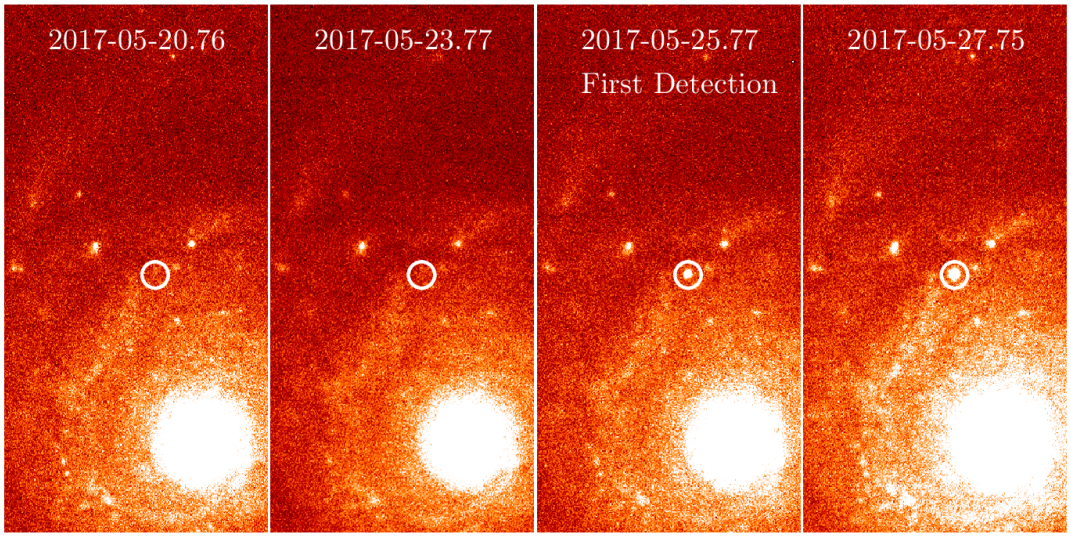

Figure 1.8. Emergency moments of SN 2017ein in NGC 3938 from IMSNG.

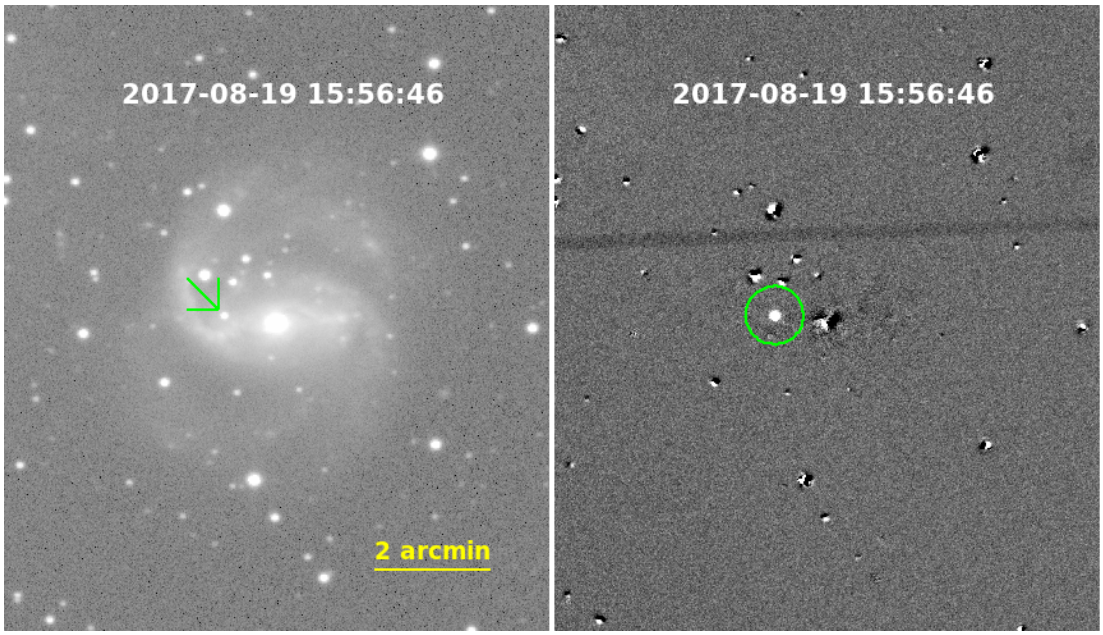

Figure 1.9. Identification of SN 2017gax in NGC 1672 from IMSNG

formance camera with a back-illuminated, deep depletion chip. In this thesis, we will detail the installation of SNUCAM-II and its performance on LSGT in Chapter 2.

From many nights of IMSNG monitoring observations, we succeeded in securing early light curves of more than a dozen nearby SNe. In this thesis, we will present the light curve analysis of a SN Ia, SN 2018kp in NGC 3367, and SNe Ic, SN 2017ein in NGC 3938 and SN 2017gax in NGC 1672. In particular, we will present how the early light curves constrain the radius of the progenitor stars in these SNe. We will ask the question if SNe Ia results from a SD system or DD system. If the progenitor system is a SD system, we will investigate if the companion star is a red giant or a smaller, main sequence star (Figure 1.10 shows the scenarios of possible SN Ia progenitor systems). For SNe Ic, we will investigate if the progenitor stars are small as expected in the stripped envelope stars, and if so, how large such a star can be (evolutionary path of possible massive binary system of SN Ib/c is shown in Figure 1.11). These results are presented in Chapters 3 and 4.

Finally, we will summarize our findings and future prospects in Chapter 5.

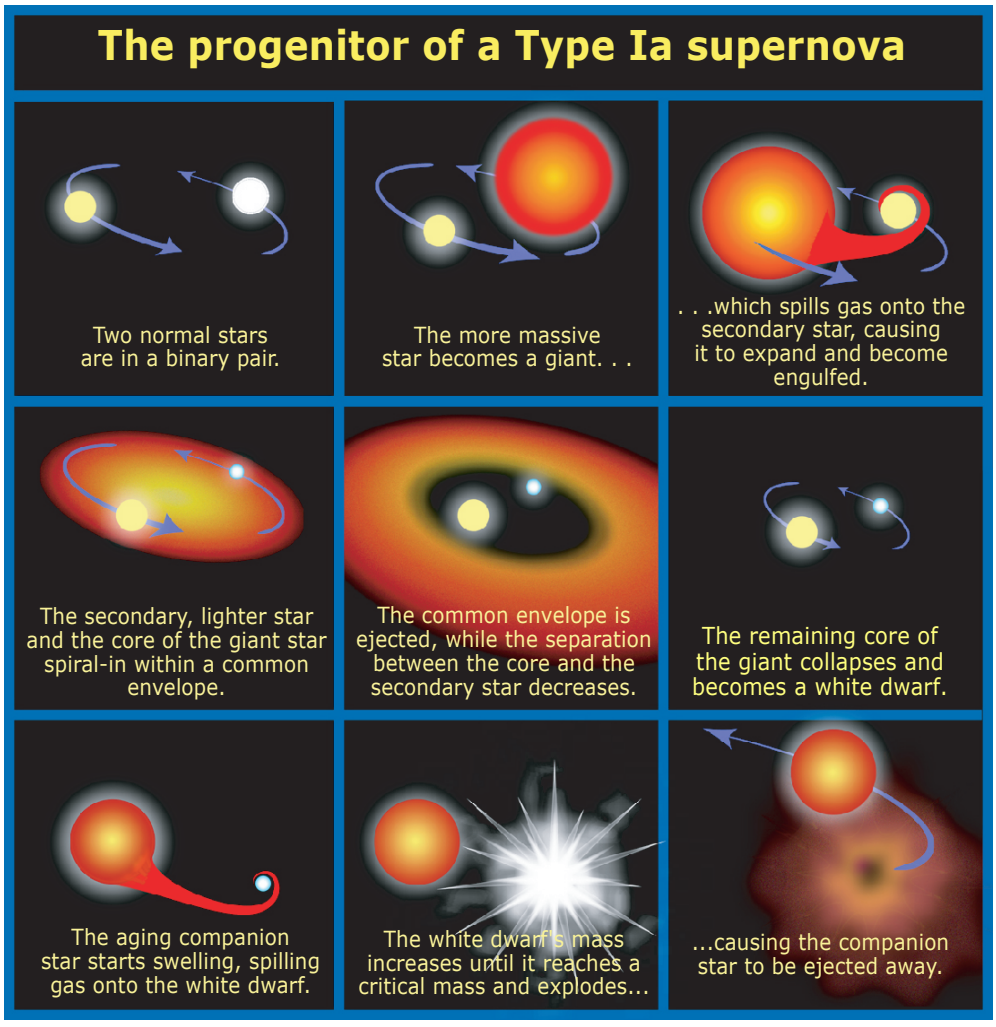

Figure 1.10. Infographics of the progenitor star of SN Ia, taken from hubblesite.org

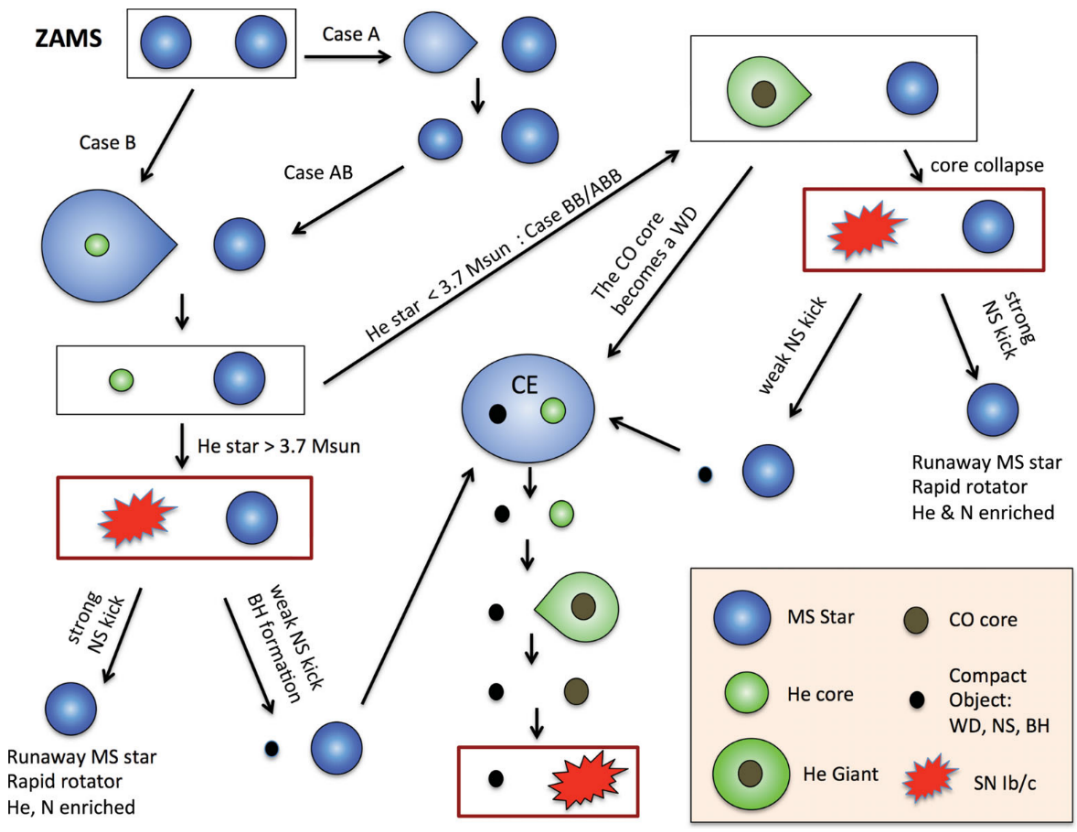

Figure 1.11. Evolutionary path of possible SN Ib/c massive binary progenitor, Adopted from Yoon (2015)

Table 1.1. IMSNG Target Galaxies

Name [AGN type]	RA (J2000)	Dec (J2000)	D_L (Mpc)	NUV (AB)	Past SNe
(1)	(2)	(3)	(4)	(5)	(6)
NGC 289	00:52:42.348	−31:12:20.92	24.0	-18.77	
NGC 337 [LIN]	00:59:50.100	−07:34:41.45	23.0	-18.64	1998dn, 2011dq, 2014cx
NGC 488	01:21:46.836	+05:15:24.48	38.0	-18.88	1976G, 2010eb
NGC 895	02:21:36.468	−05:31:17.00	37.0	-19.02	2003id
NGC 1097 [LIN]	02:46:19.092	−30:16:29.89	14.0	-18.55	1992bd, 1999eu, 2003B
NGC 1309	03:22:06.600	−15:24:00.07	29.0	-19.04	2002fk, 2012Z
NGC 1365 [S1.5]	03:33:36.396	−36:08:25.84	18.0	-19.33	1957C, 1983V, 2001du, 2012fr
UGC 2855	03:48:20.736	+70:07:58.30	14.0	-18.75	2014dg
NGC 1672 [S2]	04:45:42.516	−59:14:50.42	19.0	-19.34	2017gax
NGC 2207/IC 2163[a]	06:16:22.044	−21:22:21.76	38.0	-20.32	1975A, 1999ec, 2003H, 2010jp, 2013ai, 2018lab
NGC 2336 [S2]	07:27:04.068	+80:10:41.02	29.0	-18.83	1987L
NGC 2442 [LIN]	07:36:23.796	−69:31:50.70	21.0	-19.20	1999ga, 2015F

Table 1.1 (cont'd)

Name [AGN type]	RA (J2000)	Dec (J2000)	D_L (Mpc)	NUV (AB)	Past SNe
(1)	(2)	(3)	(4)	(5)	(6)
NGC 2775	09:10:20.100	+07:02:17.23	43.0	-18.69	1993Z
NGC 2776	09:12:14.508	+44:57:17.53	41.0	-19.34	
NGC 2782 [oLLAGN]	09:14:05.064	+40:06:49.57	41.0	-18.76	1994ak
NGC 2993/2992 [S2][a]	09:45:48.312	−14:22:06.17	34.0	-18.85	2003ao, AT2017ejx
IC 2537	10:03:51.876	−27:34:14.81	36.0	-18.40	2010lm
NGC 3147 [S2]	10:16:53.688	+73:24:02.63	40.0	-19.29	1972H, 1997bq, 2006gi, 2008fv
NGC 3169 [LIN]	10:14:14.892	+03:27:58.86	45.0	-19.25	1984E, 2003cg
NGC 3183	10:21:48.960	+74:10:37.16	49.0	-18.56	
NGC 3244	10:25:28.848	−39:49:39.00	38.0	-18.63	2010ev
NGC 3294	10:36:16.236	+37:19:28.63	30.0	-18.43	1990H, 1992G
NGC 3344	10:43:31.116	+24:55:19.74	20.0	-19.42	2012fh
NGC 3367 [S2]	10:46:35.004	+13:45:02.09	45.0	-19.84	1986A, 1992C, 2003aa, 2007am, 2018kp

Table 1.1 (cont'd)

Name [AGN type]	RA (J2000)	Dec (J2000)	D_L (Mpc)	NUV (AB)	Past SNe
(1)	(2)	(3)	(4)	(5)	(6)
NGC 3359	10:46:36.840	+63:13:26.83	23.0	-19.07	1985H
NGC 3445	10:54:35.712	+56:59:23.32	33.0	-18.55	
NGC 3629	11:20:31.776	+26:57:47.84	38.0	-18.55	
NGC 3646	11:21:43.092	+20:10:11.10	44.0	-19.47	1989N, 1999cd
NGC 3938	11:52:49.368	+44:07:14.88	19.0	-18.87	1961L, 1964I, 2005ay, 2017ein
NGC 4030	12:00:23.580	−01:06:00.00	27.0	-19.11	2007aa
NGC 4038 (Arp 244)	12:01:53.004	−18:52:04.76	21.0	-19.40	1921A, 1974E, 2004gt, 2007sr , 2013dk
NGC 4039 (Arp 244)	12:01:53.616	−18:53:11.11	21.0	-19.39	
NGC 4108	12:06:44.316	+67:09:46.12	41.0	-18.50	ASASSN-15lf
NGC 4254 (M 99) [LIN]	12:18:49.572	+14:24:59.08	16.0	-19.03	1967H, 1972Q, 1986I, 2014L
NGC 4303 (M 61) [S2]	12:21:54.936	+04:28:27.05	18.0	-19.54	1926A, 1961I, 1964F, 1999gn, 2006jv, 2008in, 2014dt
NGC 4314 [LIN]	12:22:31.980	+29:53:43.48	44.0	-18.46	1954A

Table 1.1 (cont'd)

Name [AGN type]	RA (J2000)	Dec (J2000)	D_L (Mpc)	NUV (AB)	Past SNe
(1)	(2)	(3)	(4)	(5)	(6)
NGC 4321 (M 100) [LIN]	12:22:54.768	+15:49:18.80	14.0	-18.65	2006X
NGC 4500	12:31:22.152	+57:57:52.81	48.0	-18.47	
NGC 4653	12:43:50.916	−00:33:40.54	39.0	-18.66	1999gk, 2009ik
NGC 4814	12:55:21.936	+58:20:38.80	40.0	-18.53	
NGC5194 [S2]/5195[a] (M51)	13:29:52.692	+47:11:42.54	8.4	-19.03	1945A[b], 1994I, 2005cs, 2011dh
NGC 5236 (M83)	13:37:00.876	−29:51:56.02	4.9	-18.82	1923A, 1945B, 1950B, 1957D, 1968L, 1983N
NGC 5371 [LIN]	13:55:39.936	+40:27:41.90	33.0	-19.09	1994Y
NGC 5430	14:00:45.720	+59:19:42.24	47.0	-18.70	PTF10acbu (PSN)
NGC 5457 (M101)	14:03:12.600	+54:20:56.62	6.9	-19.36	1909A, 1951H, 1970G, 2011fe
NGC 5584	14:22:23.772	−00:23:15.32	25.0	-18.43	1996aq, 2007af
NGC 5668	14:33:24.300	+04:27:01.19	25.0	-18.72	1952G, 1954B, 2004G
NGC 5850 [LIN]	15:07:07.644	+01:32:40.74	38.0	-18.65	1987B

Table 1.1 (cont'd)

Name [AGN type]	RA (J2000)	Dec (J2000)	D_L (Mpc)	NUV (AB)	Past SNe
(1)	(2)	(3)	(4)	(5)	(6)
NGC 5962	15:36:31.680	+16:36:28.15	30.0	-18.68	2016afa, 2017ivu
NGC 6070	16:09:58.680	+00:42:34.31	27.0	-18.58	
NGC 6555	18:07:49.188	+17:36:17.53	35.0	-18.54	
ESO 182-G10[c]	18:18:30.600	−54:41:39.41	49.0	-19.00	2006ci
NGC 6744 [LIN]	19:09:45.900	−63:51:27.72	9.3	-19.05	2005at
NGC 6814 [S1.5]	19:42:40.608	−10:19:25.32	23.0	-18.61	
NGC 6946[c,d]	20:34:52.572	+60:09:13.57	6.1	-19.12	1980K, 2002hh, 2004et, 2008S, 2017eaw
NGC 6951 [S2]	20:37:14.088	+66:06:20.45	25.0	-18.66	1999el, 2000E, 2015G
NGC 7083	21:35:44.592	−63:54:09.79	34.0	-18.98	1983Y, 2009hm
NGC 7479 [S2]	23:04:56.676	+12:19:22.12	30.0	-18.96	1990U, 2009jf
NGC 7552	23:16:10.776	−42:35:03.41	29.0	-18.84	2017bzc
NGC 7714/7715[a]	23:36:14.112	+02:09:18.07	41.0	-19.18	1999dn, 2007fo

Table 1.1 (cont'd)

Name [AGN type]	RA (J2000)	Dec (J2000)	D_L (Mpc)	NUV (AB)	Past SNe
(1)	(2)	(3)	(4)	(5)	(6)

Note. — (1) Galaxy name. The name in the parenthesis is another notable name of the galaxy, and the AGN types in the large parentheses are S (Seyfert), LIN (LINER), and oLLAGN; (2) & (3): Equatorial coordinates in J2000; (4) the luminosity distance; (5) NUV absolute magnitude in AB mag; (6) the past SNe in the galaxy.

[a] Galaxies in pair, the primary, NUV-selected galaxy number is given first; [b] In NGC 5195; [c] Low Galactic latitude target; [d] This object had five additional SNe before 1980: 1917A, 1939C, 1948B, 1968D, and 1969P.

Table 1.2. The current list of telescopes in the IMSNG network

Observatory/ Telescope	Instrument	Imager Field of view	Longitude/ Latitude	Altitude (m)
Maidanak Observatory	SNUCAM[b]	$18\farcm3 \times 18\farcm3$	66:53:47E	2593
1.5m[a]	4k x 4k		38:40:22N	
SNU Astronomical	SBIG STX-16803	$21\farcm2 \times 21\farcm2$	126:57:12E	190
Observatory (SAO) 1m[c]	4k x 4k		37:27:25.35N	
Deokheung Optical Astronomy				
Observatory (DOAO) 1m	SOPHIA			
2k x 2k	$13\farcm2 \times 13\farcm2$	127:26:48E		
37:31:35N	81			
Sobaeksan Optical Astronomy	PIXIS 2048B	$17\farcm6 \times 17\farcm6$	128:27:25.3	1340
Observatory (SOAO) 0.6m	2k x 2k		36:56:03.9N	

Table 1.2 (cont'd)

Observatory/ Telescope	Instrument	Imager Field of view	Longitude/ Latitude	Altitude (m)
Lee Sang Gak Telescope (LSGT) 0.43m[d]	SNUCAM-II[e] 1k x 1k	$15\farcm7 \times 15\farcm7$	149:03:52E 31:16:24S	1122
Mt. Lemmon Optical Astronomy Observatory (LOAO) 1m[f]	ARC CCD camera 4k x 4k	$28\farcm1 \times 28\farcm1$	110:47:19.3W 32:26:32.2N	2776
McDonald Observatory (McD) Otto-Struve 2.1m	SQUEAN/CQUEAN[g] 1k x 1k	$4\farcm7 \times 4\farcm7$	104:01:21.4W 30:40:17.4N	2076
McDonald Observatory (McD) 0.8m	CCD camera 2k x 2k	$46\farcm2 \times 46\farcm2$	104:01:19W 30:40:17N	2057
McDonald Observatory (McD) 0.25m	FLI16803 4k x 4k	$2.34^\circ \times 2.34^\circ$	104:01:19W 30:40:17N	2057

Table 1.2 (cont'd)

Observatory/ Telescope	Instrument	Imager Field of view	Longitude/ Latitude	Altitude (m)

Note. — Observatories are ordered toward E in longitude from the Prime Meridian.

[a] Ehgamberdiev (2018)

[b] Im et al. (2010)

[c] Im et al. (2021), in press

[d] Im et al. (2015a)

[e] Choi & Im (2017)

[f] Han et al. (2005)

[g] SQUEAN(Kim et al. 2016; Choi et al. 2015) is the upgraded system of CQUEAN(Park et al. 2012; Lim et al. 2013; Kim et al. 2011)

Chapter 2

Seoul National University Camera II (SNUCAM-II): The New SED Camera for Lee Sang Gak Telescope (LSGT)[†]

2.1 Introduction

Even in the era of giant telescopes, small telescopes – telescopes with aperture size $\lesssim 0.5$m – are still valuable observational facilities. They can cover a large field of view thanks to short focal lengths, and they can be dedicated for a few specific research projects due to the availability of the telescope time. Furthermore, small telescopes can be relatively easily deployed for robotic operations and save observation time for astronomers. Therefore, monitoring observations and rapid follow-up observations of objects like active galactic nuclei (AGNs), Gamma Ray Bursts (GRBs) and supernovae (SNe) are routinely carried out with small telescopes (Drake et al. 2009; Klotz et al. 2008; Shappee et al. 2014). The major disadvantage of small telescopes is the

[†]This chapter is a revised version of the article published in *Journal of the Korean Astronomical Society* in June 2017 (Choi & Im 2017).

lack of light gathering power. Currently, the best we can do to augment the lack of light gathering power of a single small telescope is to use CCD cameras with high Quantum Efficiency (QE). Yet, many small telescopes are equipped with commercially available font-illuminated CCD cameras that have very low QEs at short ($\sim$ 450 nm) and long ($>$ 800 nm) wavelengths. Recently, we have been operating a robotic 0.43m telescope, Lee Sang Gak Telescope (LSGT; Im et al. 2015a), and carrying out a monitoring survey of nearby galaxies with it. To maximize the observing efficiency of LSGT, we have assembled a new CCD camera system, Seoul National University CCD Camera II (SNUCAM-II), by utilizing a commercially available CCD camera with a deep depletion chip that has QEs at around 80% over 400 – 900 nm, and a 20 position filter wheel that can house 13 medium-band filters and five broad-band filters. The camera's QE represents improvement in QE by factors of 1.5 to 3 at 400 nm and 3 to 20 at 900 nm, in comparison to commonly available CCDs such as KAI-16000 and KAF-3200ME (see Figure 3 in Im et al. 2015a) making this telescope as one of the most sensitive small telescopes in the world in its class. The camera is named as a successor of SNUCAM (Im et al. 2010), a sensitive 4k x 4k CCD camera, and SNUCAM-II improves upon SNUCAM in sensitivity at long wavelengths out to Y-band regime, making it possible for this instrument to study high redshift quasars and GRBs (e.g., Choi et al. 2012). Another unique aspect of SNUCAM-II is the availability of many medium-band filters. The use of medium-band filters makes it possible to trace the SEDs of objects of interest, and this is especially advantageous for monitoring observation of AGNs where the time lag of the broad emission lines and the continuum flux can be traced efficiently for black hole mass measurement. We have demonstrated the power of the medium-band observation on a moderate-sized telescope using the SED Camera for Quasars in Early Universe (SQUEAN; Kim et al. 2016) on the 2.1m telescope at the McDonald observatory where 9 medium-band filters are installed. Specifically, we have shown that medium-band observation can select high redshift quasars effectively (Jeon et al. 2016), and we have been using the instrument to survey faint quasars at $z \sim 5$. Many other applications of the medium-band imaging are possible by tracing

Figure 2.1. SNUCAM-II after installation at LSGT.

SEDs of various objects such as asteroids, stars, galaxies, to name a few. In this paper we describe the overall characteristics of the SNUCAM-II system, and its performance that are derived from the laboratory testing and the on-sky observation using LSGT.

2.2 System

Here, we describe each component of SNUCAM-II. Those are CCD camera, band pass filters and a filter wheel. Software to control LSGT system and typical procedure of remote observation are explained here to help the potential observer.

2.2.1 CCD camera

Due to a wide variety of the applications we expect for SNUCAM-II, we employed a CCD camera with good sensitivity over a broad wavelength region from 300 nm to 1100 nm. We adopted the ANDOR[1] iKon-M DU934P BEX2-DD model CCD camera that uses a deep depletion, back illuminated and fringe suppression E2V CCD chip with extended range dual Anti Reflection coating on it. Its QE is about 90 % from 400 nm to 800 nm and even at longer wavelength 1000nm, QE is over 30 % thanks to the deep depletion chip (the black dashed line in Figure 2.2). Each pixel has a full well depth of 130,000 e^-. The CCD chip has 1024 $\times$ 1024 pixels and the physical size of each pixel is 13 μm $\times$ 13 μm, which translates into 0.92 arcsec pixel scale at the $f/6.8$ focal plane of LSGT. We use a model with thermoelectric cooling that can cool the CCD chip to -80 °C. For our nominal operation, we set its cooling temperature as -70 °C to achieve a reasonable balance between the QE at long wavelength and the reduction in dark current (see Park et al. 2012). The camera offers 4 different readout rates (5.0, 3.0, 1.0, 0.05 MHz) as a default, and users can choose parameters of Vertical Shift Speed (VSS), Horizontal Shift Speed (HSS) and Preamp Gain (PG). VSS and HSS can be set to one of 2.25, 4.25, 8.25, 16.25, 32.25, 64.25 μsec. PG has three kinds of values as $\times$1, $\times$2 and $\times$4. Also binning can be configured as one of following setting, 1$\times$1, 2$\times$2, 4$\times$4, 8$\times$8 and 16$\times$16. Shutter speed is at the default value of 30 msec at opening and closing and adjustable. For mechanical connection to the filter wheel, C mount is installed on top of CCD camera, so we used a custom made adapter for connecting CCD camera to the filter wheel. As for the setting of the parameters, we use the following values as default: PG of $\times$4 (gain $\sim 1.15 \pm 0.03$ e^-/ADU), 1 MHz readout rate, and the cooling temperature of -70 °C. VSS, HSS, and the shutter speed are set at 4.25 μsec, 2.25 μsec and 30 msec respectively as recommended by the manufacturer.

[1] http://www.andor.com

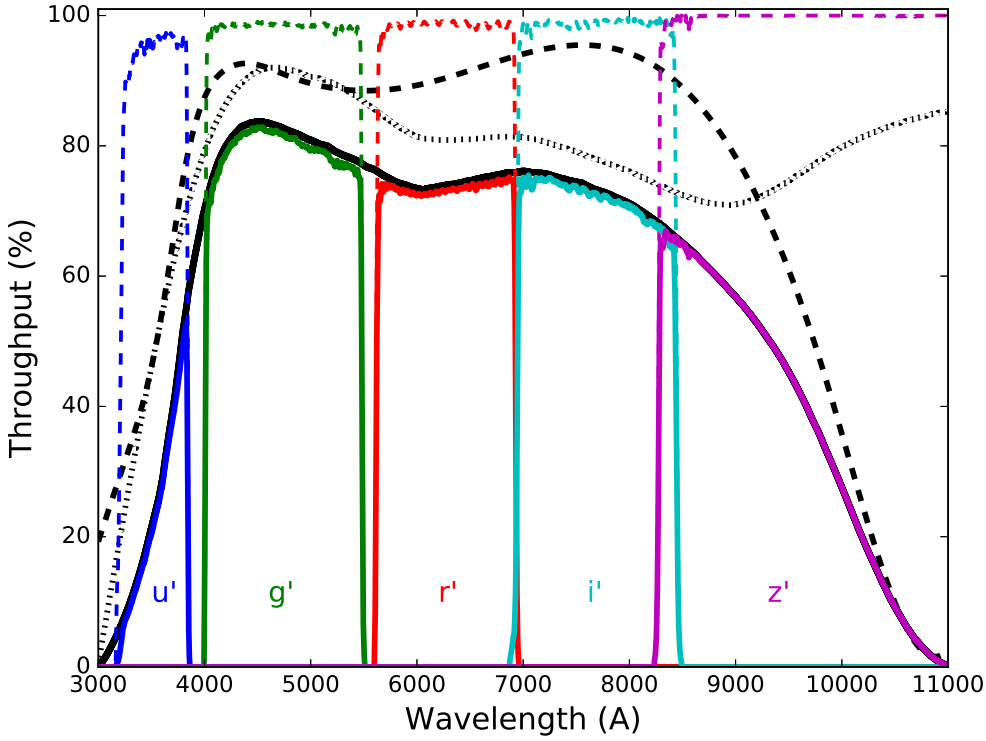

Figure 2.2. The transmission curves of the SDSS *ugriz* filters (the colored dashed/solid line) and the total throughput of the SNUCAM-II system (the thick solid solid line) taking into account of the CCD QE (the black dashed line) and the throughput of the telescope optics (the black dotted line; Im et al. 2015a). The colored solid lines show the filter transmission curves after taking into account of the CCD QE and the optics throughput.

2.2.2 Filters and Filter Wheel

The SNUCAM-II uses a default set of 18 circular filters with 25 mm diameter each: SDSS *ugriz* filters and 13 medium band filters. The filter transmission curves and the transmission curves multiplied by the CCD QE and the throughput of the telescope optics are presented in Figures 2.2 and 2.3. Table 2.1 shows the filter names, their effective wavelengths and FWHM (Full Width at Half Maximum) values. The SDSS *ugriz* filters are purchased from the Astrodon company (their Generation 2 Sloan filters).[2] The 13 medium band width (50 nm) filters spanning from 400nm to 1050nm are standard products from Edmund Optics [3]. We named them by adding the central wavelength in nm unit to the initial m meaning the medium band filter (e.g., m425 for the medium band filter with the central wavelength at 425 nm). These 18 filters are mounted on the Finger Lake Instrumentation LLC [4] (FLI) CenterLine-1-20 color filter wheel. The filter wheel has dual filter wheels Wheel 0 and Wheel 1, with 10 slots each. Keeping the first slot of each wheel as blank position, 18 filters can be installed. After installation of the filters, the physical positions of the filters and logical filter names used in programs are connected by naming in 'FLIfilters' program provided by the manufacturer.

2.2.3 Software and Data Collection

For the camera system control, we use commercial softwares: 'MaximDL pro 5' [5] and 'FLIfilter' programs. These programs and the telescope operating system software are integrated into the ACP Observatory Control Software for the command tasks necessary for the observations (observation program reservation, remote communication, actual performance of the system and the roof control). A web page is set up for system status monitoring, the observation plan, the observation program reservation and the weather information of SSO. An observer can configure all the parameters of the actual observation on the webpage and monitor activities of LSGT and SNUCAM-II in real

[2] http://www.astrodon.com
[3] http://www.edmundoptics.co.kr
[4] http://www.flicamera.com
[5] http://diffractionlimited.com/

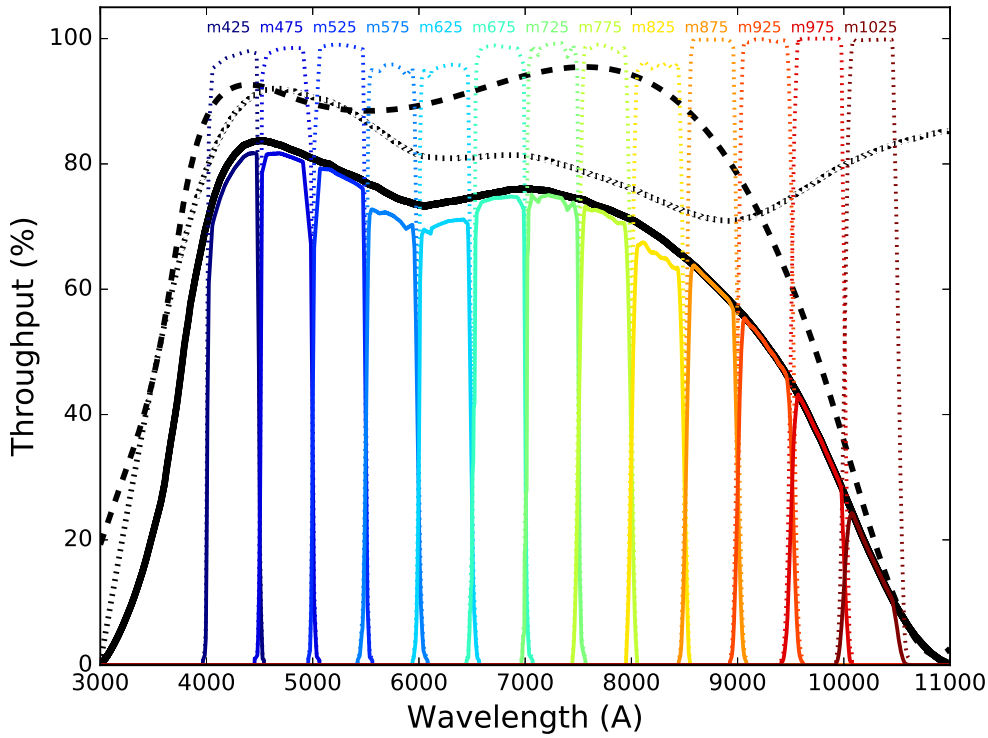

Figure 2.3. The transmission curves of the medium-band filters before (the colored dotted line) and after (the colored solid lines) taking into account the CCD QE and the telescope optics throughput. The meanings of the other lines are identical to those in Figure 2.2.

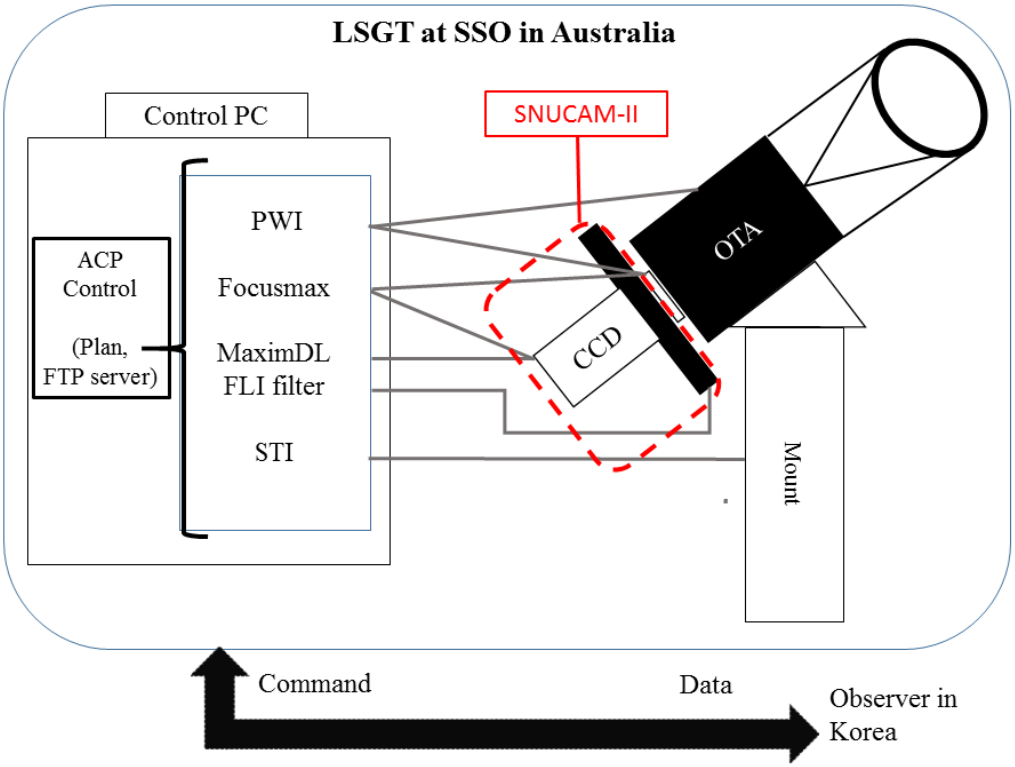

Figure 2.4. Schematic diagram showing the SNUCAM-II system.

time. A common mode of the observation uses the "plan" document that defines the target coordinate, the number of images to take, the filter, and the binning and the exposure times. This "plan" document is uploaded to the web-based reservation system for robotic observation of the target. When the observation plan is finished, the system sends an observation summary e-mail to observer along with the weather data figure, logs and the list of the obtained data. The images are uploaded on the data storage server where an observer can access with ID and password and download them. Currently, these systems run on the Window 7 operating system. The schematic diagram of the system is shown in Figure 2.4. The telescope and the computer system is under management of iTelescope.net.

2.3 Characteristics of SNUCAM-II

In this section, we characterize the properties of SNUCAM-II camera. The characteristics of SNUCAM-II are summarized in Table 2.2.

2.3.1 Dark Current

We took bias and flat images in the laboratory and on the sky. By combining the bias frame values and the flat images taken at two different epochs (B_1 and B_2 for bias, F_1 and F_2 for flats), we calculated the gain and the readout noise values using the equations below (Howell et al. 2006).

$$Gain = \frac{(\bar{F}_1 + \bar{F}_2) - (\bar{B}_1 + \bar{B}_2)}{\sigma^2_{F_1-F_2} - \sigma^2_{B_1-B_2}} \tag{2.1}$$

$$ReadNoise = \frac{Gain \cdot \sigma_{B_1-B_2}}{\sqrt{2}} \tag{2.2}$$

We find that the gain and the readout noise are 1.15 ± 0.03 e^-/ADU (Analog to Digital Unit) and 6.0 ± 0.1 e^-, consistent with the test report values from the manufacturer.

2.3.2 Bias, Dark and Flat

The dark current values were measured in the laboratory and in the dome during the daytime in dark condition with the dome light turned off. The temperature settings were varied from -80 °C to -30 °C, and the mean values of the frames from 300 sec exposures were recorded after bias subtraction. The result is shown in Figure 2.5, where the blue circles are measured values and the green circles are values from test report of the manufacturer. The laboratory values are consistent with the test report, with the dark current of 0.2 e^-/s/pixel at -70 °C setting. We checked the variability of the bias image, dark current and pixel-to-pixel variation of flat images. Compared to the readout noise of 6.6 e^- of the optimal setting from the test report, the measured value from multiple test bias data is 6.0 e^-, consistent with the test report results. And its

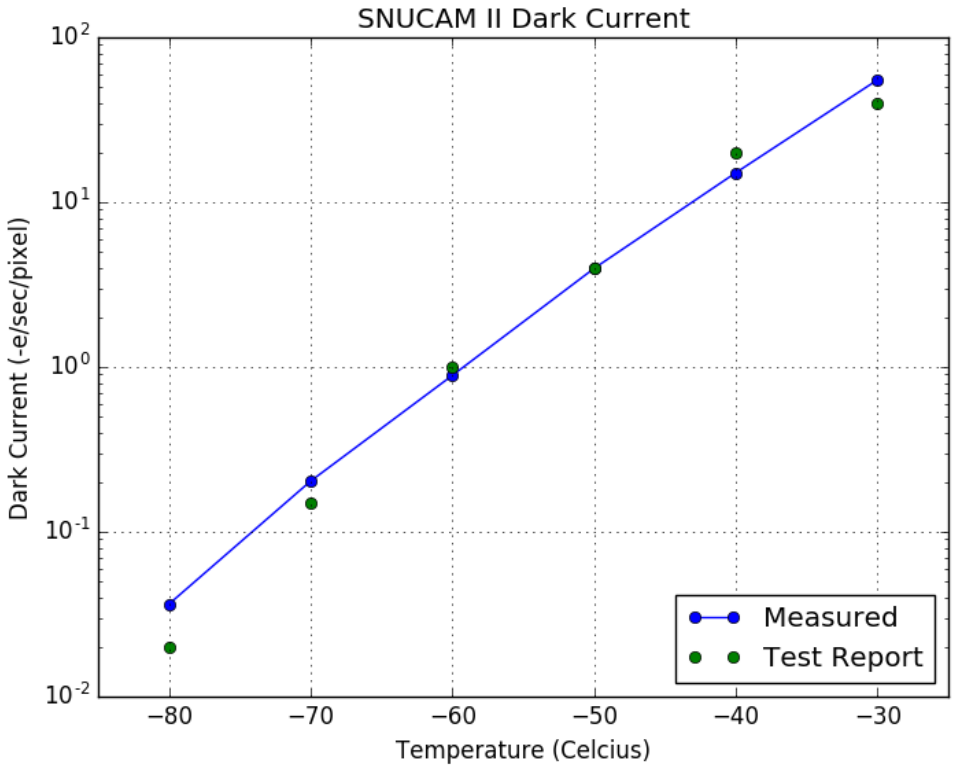

Figure 2.5. The dark current of SNUCAM-II, Note that the dark current is very small at -70 °C.

variation over different locations in a single image is up to 0.5%. There is a small amount of intra-night variability which may originate from electrical instability. We examined the bias variation over several hours and found that the mean bias fluctuation level is lower than 4 ADUs which is less than the readout noise value but not negligible. We also compared the flat images taken at different nights, and examined the pixel-to-pixel variation in normalized flat images. The peak-to-peak variation of flat images is less than 5% for all the filters. These calibration frames are taken regularly every month. So far, there is no noticeable variation in these frames for 6 months since the regular SNUCAM-II was started.

2.3.3 Linearity

We examined the linearity of the detector in the laboratory. In a dark room, a light source is placed to create a diffuse background light. Then, the mean values of the image are recorded by varying the exposure time. The result is plotted in Figure 2.6. The mean values are well fitted with a linear relation with a constant slope up to 60000 ADU level. Even at a low signal level of < 1000 ADU taken from sub second exposures, the detector shows good linearity at well within 2%.

2.3.4 Shutter Pattern

To examine at what exposure time the shutter pattern starts to show in the images, we obtained short exposure light images from 0.1 sec to a few sec. Figure 2.7 shows the light images taken with short exposures. One of the images is the division of the 0.1 sec images by the 6.0 sec image, which shows no significant change in the image pattern from 0.1 to 6.0 sec exposures. Considering the shutter speed is set at 30 msec for the open and close time each, shutter pattern may show up in exposure times well below 0.1 sec. So far, we can conclude that images taken with the exposure time as short as 0.1 sec is not affected by the shutter pattern.

2.4 PERFORMANCE

2.4.1 Standard Star Observation, Zero Points, and AB Offsets

We derived photometric zero points from standard star observations and AB magnitude offset. Standard stars were observed in dark clear nights of seeing condition of FWHM $\sim$ 2.5 arcsec. We observed an A0V star HIP 114918 (V = 9.05 mag) from the *HIPPARCOS* catalog (Perryman et al. 1997) in all the 18 filters on 2016 Oct 31, Nov 02 and 21. First, we calculated synthetic magnitudes in our filter system using the Vega model spectra of Kurucz (1993) based on equation (2.3), where F(λ) is the specific flux of Vega model in λ, and R(λ) is the throughput of the SNUCAM-II system consisting of filter transmission, CCD QE, and the telescope optics throughput. The AB magnitudes

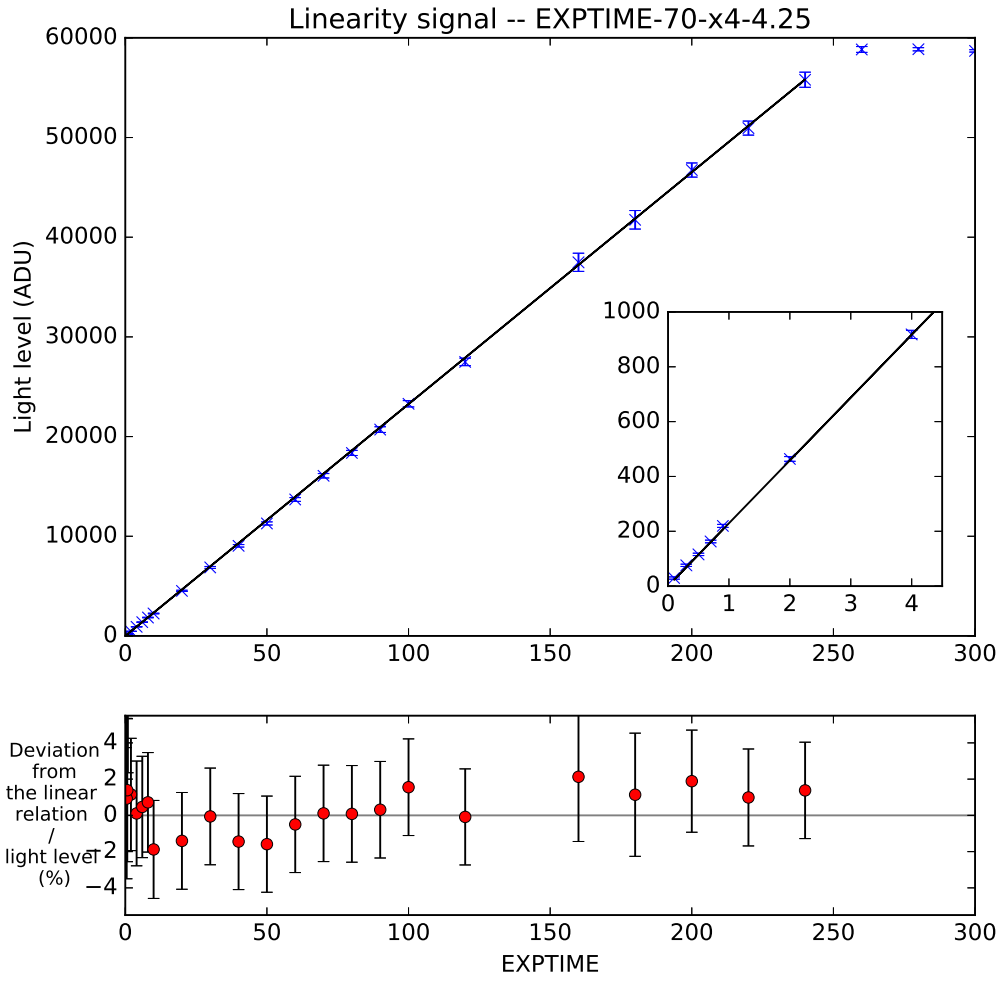

Figure 2.6. The linearity of the CCD as tested in the laboratory. The CCD shows a very good linearity from tens of ADU to the saturation value of $\sim$ 60,000 ADU.

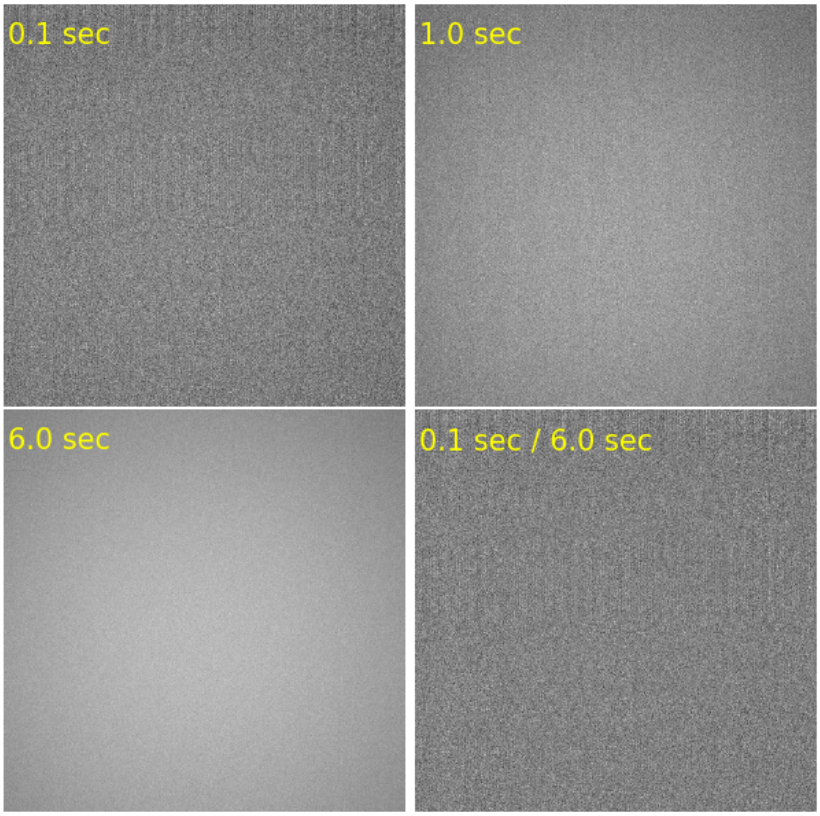

Figure 2.7. Short exposure time light frames that were taken during the laboratory test. The exposure times are indicated in each panel. No significant pattern is visible when 0.1 sec frame is divided by 6.0 sec frame, suggesting that the shutter pattern is negligible even in the 0.1 sec image.

of a zero magnitude star were estimated to find the AB offset from Vega magnitude by substituting $F(\lambda) = 10^{48.6/2.5}\mathrm{c}/\lambda^2$ for Vega model flux, where c is the speed of light.

$$\mathrm{m} = -2.5\log\frac{\int \mathrm{F}(\lambda)\mathrm{R}(\lambda)\mathrm{d}\lambda}{\int \mathrm{R}(\lambda)\mathrm{d}\lambda} + \mathrm{const} \tag{2.3}$$

$$\mathrm{M} = \mathrm{m} + \kappa(\mathrm{X} - 1) + \mathrm{C} \tag{2.4}$$

We measured the magnitudes of the standard star using Source Extractor (Bertin & Arnouts 1996) auto-mag following equation (2.4), where M is the apparent magnitude

of the star, m is the instrumental magnitude, κ is the atmospheric extinction coefficient, X is airmass term ($\sec Z$, where Z is the zenith distance) and C is the zero point at airmass 1. We measured the atmospheric extinction coefficients and the zero point of all the filters and they are presented in Table 2.3 along with AB offsets. The errors indicate the root mean square (rms) values of three nights data. Note that there was considerable variation in the atmospheric coefficient values in each night, and the presented values should serve only as a rough measure. Figure 2.8 shows the zero point of each filter at $X = 1$ along with the overall efficiency of the SNUCAM-II, including the telescope throughputs. The most sensitive band filter is g where the overall throughput of the system is the highest and the zero points generally follows the overall throughput of the system. The zero point of the long wavelength region is shallower than that of central wavelength region depending on throughput.

2.4.2 NGC6902 Observation: On-Sky Magnitude Calibration and Magnitude Limits

To Test the on-sky performance of SNUCAM-II, we took images of NGC6902 in all the filters. Figure 2.9 shows the images of NGC 6902 in all the 18 SNUCAM-II filters taken with 180 sec single exposure. They were taken one after another on the same night with the 'filter offset' option in a clear night with seeing FWHM $\sim$ 3 arcsec, where 'filter offset' means that the focus changes among various filters were made using a preset amount of the focus shift values between filters. We also derived the zero-point of the images and the image depths from the data. To derive the zero point, we downloaded the $BVgri$ photometric data of APASS (Henden et al. 2016) and J, H magnitudes of stars in the field of view of SNUCAM-II images, and selected stars at $12 < r < 15$ mag as photometric reference. The spectra of 175 stars from the stellar spectral library (Gunn & Stryker 1983) are fitted to the APASS+2MASS (Skrutskie et al. 2006) photometric data points (up to J-band), and the best-fit stellar spectra was chosen with a proper offset to the observed magnitude of the stars in the NGC 6902. Then, the photometric zero point of each filter was derived for each reference

star, by taking the mean of the zero points from the stars. The error in the zero point is estimated as the rms scatter of the zero points from different stars. The 5-σ point source detection limits are calculated assuming a seeing condition of 3 arcsec which is slightly worse than the median seeing of LSGT (Im et al. 2015a), the aperture diameter of 3 arcsec with the aperture correction included, and at the airmass as indicated. The zero points and the detection limits are shown in Table 2.4, and also plotted in Figure 2.8. The derived values agree with the standard star data result within 0.15 mag. The rms scatters in the zero points indicate that the photometric zero-points can be derived to an accuracy of 0.011 to 0.081 mag from the stars in the science images alone by using the APASS+2MASS data.

2.5 Scientific Programs

By virtue of many filters and the increased sensitivity, LSGT is now more powerful than before for various scientific observations. The 13 medium band filter photometry can provide low resolution spectroscopy of R $\sim$ 15 (Kim et al. 2016). Remote observation of the southern hemisphere has shown its promises for the transient observation of SNe, GRB afterglow (Choi et al. 2016) and gravitational wave sources. LSGT has been one of the main observational facilities of IMSNG (Intensive Monitoring Survey of Nearby Galaxy), which aims to discover newly appearing SNe and detect early shock-heated emission after explosion that can constrain the size of the SN progenitor star (Im et al. 2015b). AGN monitoring study can benefit from medium band photometry that can sample broad emission lines for the reverberation mapping study of AGN black hole masses, and the medium-band reverberation mapping of several AGNs is ongoing. SNUCAM-II on LGST has been used in small research projects for graduate student classes. Examples of the small projects include the SED study of asteroids, SN remnants, variable stars, and stellar clusters.

2.6 Summary

We have presented the characteristics and the performance of the SNUCAM-II system that is installed on LSGT at the Siding Spring Observatory in Australia. This upgraded system is more powerful than the front-illuminated CCD camera systems that have been in use earlier, with QE of > 80 % from 400 - 900 nm, factors of a few to tens improvement at short and long wavelengths. SNUCAM-II also boasts 18 filters, *ugriz* and 13 medium band pass filters from 400 nm to 1100 nm having 50 nm band width for the characterization of SEDs of many different kinds of sources. Under the adopted operation parameters, the CCD gain is 1.15 ± 0.03 e^-/ADU, the readout time is 0.9 sec for the 1k $\times$ 1k frame. The readout noise is 6.0 e^-, and the dark current is 0.2 e^-/sec at -70 °C. The SNUCAM-II system shows a good linearity (better than 98% at the currently measurable limit) ranging from tens of ADU $\sim$ 60000 ADU. The shutter pattern was also examined, and we find no visible shutter pattern in images even with exposure time as short as 0.1 s. Photometric calibration parameters were derived from the analysis of the data of a standard star and reference stars in the vicinity of NGC 6902, showing that SNUCAM-II on LSGT can reach the magnitude limit of $g = 19.91$ AB mag and $z = 18.20$ AB mag at 5-σ with 180 sec exposure time for point source detection. With its high sensitivity at short and long wavelengths, the availability of many medium-band filters, and the robotic operation capability, SNUCAM-II on LSGT can be used to perform unique scientific projects such as photometric reverberation mapping of AGNs and intensive monitoring of galaxies to catch the early light curve of SNe.

Table 2.1. Filter information of SNUCAM-II

Filter Name	Effective Wavelength (nm)	FWHM (nm)
u	363.1	25.7
g	474.5	147.5
r	627.7	131.4
i	767.7	149.8
z	915.4	157.2
$m425$	425.9	48.5
$m475$	475.0	48.6
$m525$	524.9	49.7
$m575$	574.3	48.5
$m625$	624.7	49.0
$m675$	675.7	48.6
$m725$	725.7	48.9
$m775$	774.8	49.4
$m825$	824.5	49.3
$m875$	875.4	48.2
$m925$	925.1	51.8
$m975$	973.4	49.1
$m1025$	1021.0	40.6

Note. — A list of the currently available SNUCAM-II filters. The effective wavelengths and the FWHM values of 18 filters are described together. The effective wavelengths are derived following the equation (3) of Fukugita et al. (1996) and the FWHM values are widths between 50 % of peak values of transmission curves.

Table 2.2. Characteristics of SNUCAM-II

Gain	1.15 ± 0.03 e^-/ADU
Read noise	6.0 e^-
Dark current	0.2 e^-/pixel/sec at -70 °C
Pixel scale	0.92 arcsec/pixel
FOV	15.7 arcmin x 15.7 arcmin
Pixel size	13 μm × 13 μm
Image area	13.312 mm × 13.312 mm
Cooling temperature	-70 °C
Digitization precision	16 Bit
Pixel number	1024 × 1024
A/D readout rate	1 MHz
Readout time	0.88 sec (1 × 1 binning)
Linearity	>> 98 % (0 - 60000 ADU)

Table 2.3. Photometric calibration parameters from standard star data (Vega system)

Filter name	AB offset	Atmospheric Extinction Coefficient	Zero Point (Vega)
u	0.864	-0.516 ± 0.142	18.698 ± 0.115
g	-0.106	-0.265 ± 0.078	22.178 ± 0.067
r	0.156	-0.120 ± 0.026	21.679 ± 0.074
i	0.383	-0.040 ± 0.104	21.195 ± 0.086
z	0.525	-0.072 ± 0.079	20.419 ± 0.089
$m425$	-0.155	-0.334 ± 0.068	20.894 ± 0.080
$m475$	-0.103	-0.158 ± 0.096	20.989 ± 0.075
$m525$	-0.039	-0.246 ± 0.012	20.894 ± 0.024
$m575$	0.054	-0.191 ± 0.035	20.736 ± 0.021
$m625$	0.149	-0.140 ± 0.006	20.536 ± 0.041
$m675$	0.267	-0.083 ± 0.069	20.325 ± 0.060
$m725$	0.321	-0.136 ± 0.037	20.178 ± 0.067
$m775$	0.401	-0.044 ± 0.050	19.843 ± 0.067
$m825$	0.479	-0.063 ± 0.078	19.602 ± 0.080
$m875$	0.519	-0.032 ± 0.027	19.350 ± 0.048
$m925$	0.499	-0.121 ± 0.113	18.769 ± 0.064
$m975$	0.546	-0.065 ± 0.097	18.106 ± 0.067
$m1025$	0.623	0.027 ± 0.070	16.910 ± 0.052

Table 2.4. Photometric calibration parameters from NGC 6902 data

Filter name	Zero Point (AB mag)	Zero Point Error	Airmass sec Z	Limiting Magnitude (AB mag)
u	19.646	0.081	1.024	18.39
g	22.073	0.023	1.155	19.91
r	21.747	0.016	1.135	19.51
i	21.450	0.024	1.112	18.96
z	20.867	0.012	1.024	18.20
$m425$	20.845	0.042	1.026	19.34
$m475$	20.906	0.027	1.030	19.34
$m525$	20.870	0.025	1.038	19.29
$m575$	20.742	0.020	1.051	19.01
$m625$	20.625	0.017	1.067	18.93
$m675$	20.504	0.018	1.087	18.84
$m725$	20.401	0.018	1.110	18.63
$m775$	20.166	0.011	1.135	18.27
$m825$	19.952	0.015	1.168	18.06
$m875$	19.766	0.009	1.202	17.74
$m925$	19.206	0.014	1.249	17.38
$m975$	18.548	0.014	1.295	16.74
$m1025$	17.409	0.031	1.349	15.61

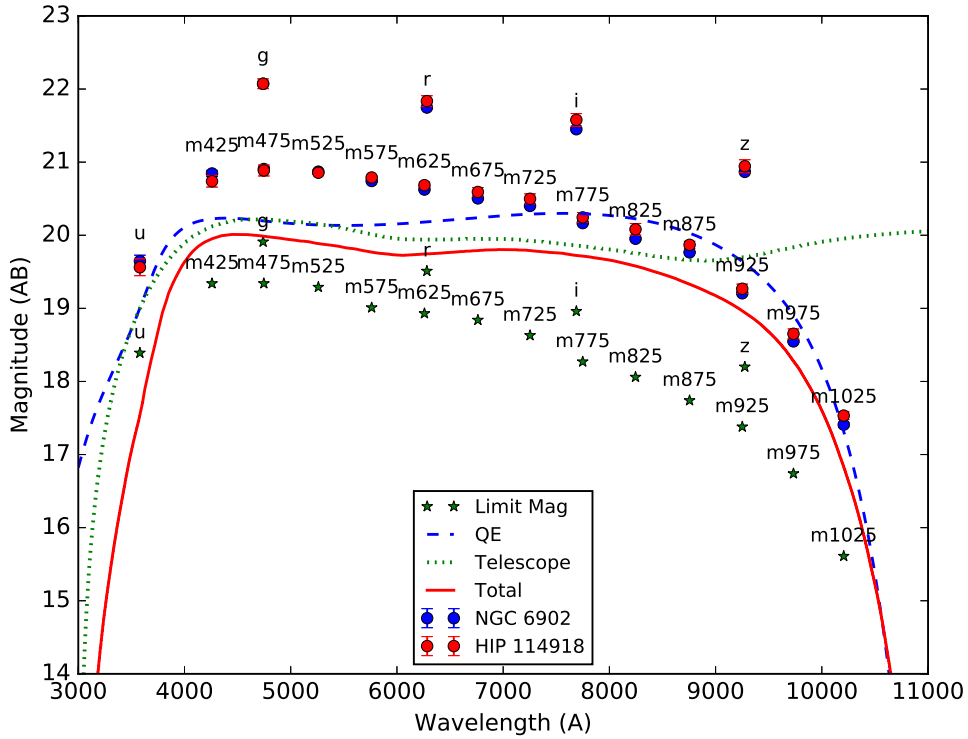

Figure 2.8. The limiting magnitudes (the green stars) and the magnitude zero points derived from the NGC 6902 field (the blue filled circles) and the HIP 114918 data (the red filled circles). The blue dashed line is QE of the CCD camera, the green dotted line is the telescope throughput and the red solid line is the overall throughput of the system. The lines are scaled to match the magnitude scale of the zero point values. The limiting magnitudes assume the exposure time of 180 sec and the 5-σ detection of a point source.

Chapter 3

On the progenitor star of SN 2018kp

3.1 Introduction

Being one of the most dramatic explosive events of the universe, supernovae (SNe) are holding keys for understanding various astrophysical phenomena from stellar evolution to the acceleration of cosmic expansion (e.g., Howell 2011). Nonetheless, their progenitor systems and explosion mechanisms are not fully understood (Maoz et al. 2014). Type Ia supernova (SN Ia) is known as the result of the thermonuclear explosion of a Carbon-Oxygen White Dwarf (CO-WD) star in a binary system. By their uniformity of progenitor system, their peak luminosity might be regarded similar to each other, but not identical enough to use the peak luminosity directly as a distance indicator. However, it is known that the width of the light curve (LC), Δm_{15}, and the B-band peak absolute magnitude ($M_{B,Max}$) have a tight correlation known as the Philips relation (Philips 1993). By taking into account this correlation, SNe Ia light curves can be transformed into the same shape, making it possible to use them as the standardized candle for cosmological studies.

But there are some counter arguments that SN Ia are not all of a kind (Jha et al. 2019). Their luminosity may be dependent on their environments or progenitor systems (Kim

et al. 2019). For better applications and understanding SN Ia, it is necessary to look into their explosion mechanisms and physical properties. In that sense, setting constraints on progenitor system will shed light on our knowledge on the SN Ia.

Two leading models of SN Ia progenitor systems are the single degenerated (SD) binary system that is made of one WD and a main sequence or red giant star (Whelan & Iben 1973; Nomoto 1982) and the double degenerated (DD) binary system that is made of two WDs (Maoz et al. 2014).

To test these two possibilities, the early phase light curve has been suggested as a useful indicator of progenitor star sizes (Rabinak et al. 2012; Kasen 2010; Piro & Nakar 2013, 2014). Early Light curve of SN Ia can be dominated by shock heated emission from a companion star for a duration of hours to days. Previous numerical and analytic studies suggest that the luminosity of the shock-heated emission is dependent on the radius of the progenitor system (namely the companion star of the exploding WD).

There are a dozen of observational studies which investigate the early light curves of SNe Ia (SN 2011fe; Bloom et al. 2012; Nugent et al. 2011, SN 2015F; Im et al. 2015b, SN 2012cg; Marion et al. 2016, iPTF16abc; Miller et al. 2018, ASASSN-14lp; Shappee et al. 2016). Many of these studies failed to detect the shock-heated emission, ruling out red giant stars as the companion star of the exploding WD. Yet, a few studies exist showing possible shock heated emission and supporting the SD model of SNe Ia (Im et al. 2015b; Li et al. 2019; Hosseinzadeh et al. 2017). These mixed results show the importance of building up a statistical landscape of the SNe Ia progenitors by enlarging the sample size of SNe Ia with early light curve data. Furthermore, obtaining deeper, higher cadence monitoring of the sky would allow us to probe short-lived, fainter shock-heated emission from smaller progenitors. To achieve such goals, we have been performing the Intensive Monitoring Survey of Nearby Galaxies (IMSNG), which is a < 8 hour cadence monitoring of 60 nearby galaxies at < 50 Mpc (Im et al. 2019). Here, we present the IMSNG optical light curve analysis results of SN 2018kp in NGC 3367. From these analyses, we will provide constraints on the progenitor system as well as general characteristics of this supernova. We present our results as follows. Section

1 describes on the SN 2018kp and its host galaxy. And section 2 describes the observations and data obtained. Section 3 describes the analysis of the light curve and results. We discuss the progenitor properties of SN 2018kp in Section 4. The conclusions are given in Section 5.

3.2 Observation & Analysis

3.2.1 SN 2018kp

SN 2018kp was discovered at the outskirt of NGC 3367 on 2018-01-24 08:42:06 (UTC) at RA = 10:46:33.070 and DEC = +13:44:30.73 by the SNhunt group (Drake et al. 2018). Figure 3.1 shows the color image of SN 2018kp taken by the Mt. Lemmon Optical Astronomy Observatory's 1 m telescope (hereafter, LOAO; Han et al. (2005)). It was classified as a SN Ia by Neill (2018). NGC 3367 is one of the high priority IMSNG targets and IMSNG has been observing it intensively from 2017. NGC 3367 is classified as a bared spiral galaxy and its redshift is $z = 0.0101$ (Lu et al. 1993). The distance modulus to NGC 3367 is $\mu = 33.2$ which corresponds to the distance of 43.5 Mpc (Tully & Fisher 1988). Around the time of discovery, NGC 3367 has been observed nearly every night from the 30 inch telescope of the McDonald observatory (hereafter, McD30INCH; IM et al. 2019), one of the IMSNG telescopes. Our data contain a pre-discovery detection (3 hours ahead) of SN 2018kp at 2018-01-24 05:55:48 UT. Figure 3.2 shows a time series images of SN 2018kp around the time of the discovery after subtracting a reference image.

3.2.2 Observation

The IMSNG facilities used for the observations of SN 2018kp are AZT-22 1.5 m telescope at Maidanak Astronomical Observatory (hereafter MAO; Im et al. 2010; Ehgamberdiev 2018) in Uzbekistan, the LOAO 1 m telescope in US, McD30INCH and the Wide-field IFU Telescope (hereafter, WIT; Im et al. 2021; Hwang et al. 2021) 0.25 m

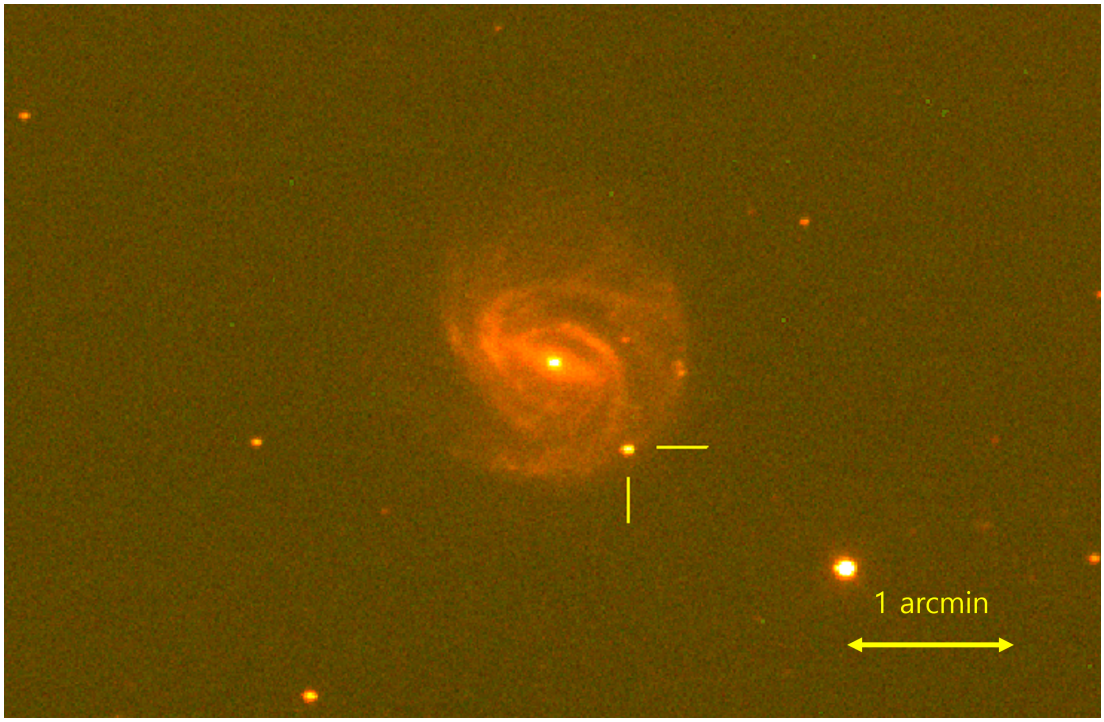

Figure 3.1. Color image of SN 2018kp on NGC 3367. The BVR images taken with LOAO were combined to create this image.

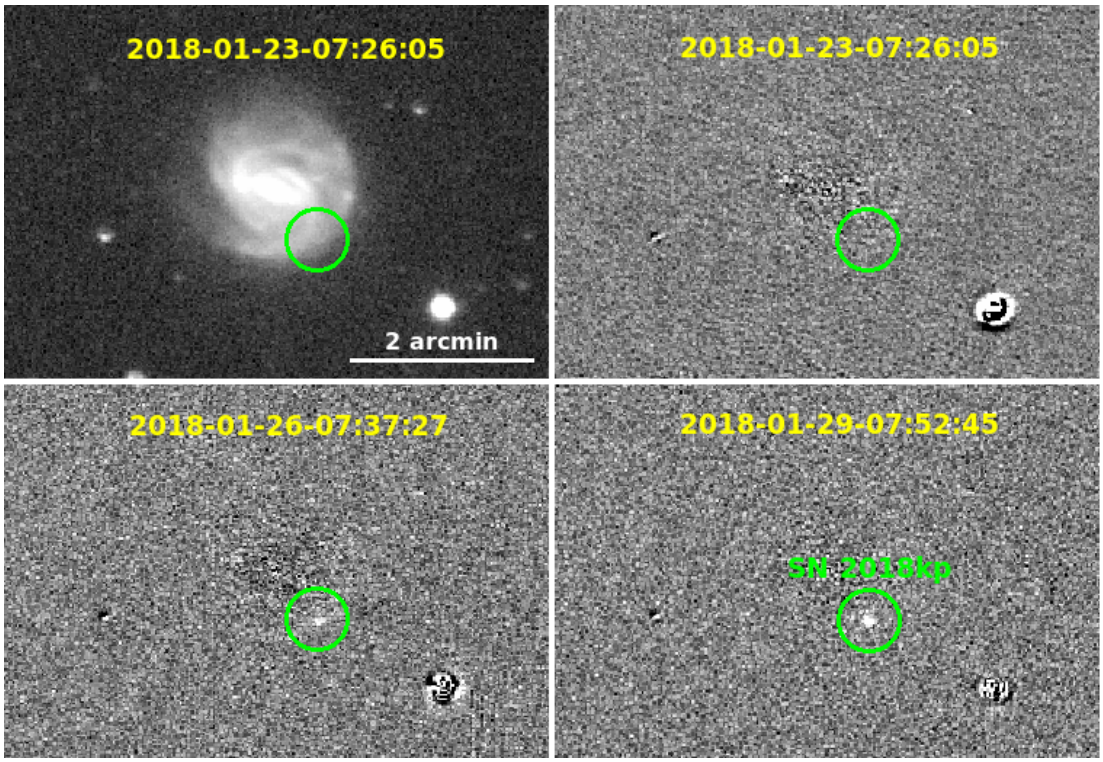

Figure 3.2. The first detection and difference images of SN 2018kp taken by McD30INCH. The difference images are created by subtracting a reference image from the observed images. The difference images show how detected signal of SN 2018kp changes with time.

Telescope (hereafter CCA250) at the McDonald Observatory in US, Mt. Sobaek 0.6 m Telescope (hereafter, SOAO; Im et al. 2019), the 1 m telescope of Deokheung Optical Astronomy Observatory (hereafter DOAO; Im et al. 2021) and 0.43 m Lee Sang Gak telescope of Siding Spring Observatory in Australia (hereafter, LSGT; Im et al. 2015). The daily observations around the discovery epoch were carried out in R-band with the McD30INCH, and after the discovery, we obtained the multi-band data from $BVRI$ to gri depending on the telescope. Depending on the telescope, a single epoch image depth for a point source detection at $5-\sigma$ varies from 19.5 mag to 20.5 mag by stacking 3-5 single images.

3.2.3 Data Analysis & Photometry

The images from the telescopes were pre-processed through standard procedure using the *IRAF/CCDPROC* and *astropy* packages. The procedure includes the zero, dark, flat calibrations and the WCS registration with the *astrometry.net* (Lang et al. 2010) and *Scamp* (Bertin 2010) softwares. We adopted the image template subtraction method to isolate and derive magnitudes of the SN utilizing the *HOTPANTS* software (Becker 2015). A reference image, created from high quality images well before or after the SN discovery (see below), was convolved with a Gaussian kernel and flux-scaled to match the seeing size and the zero-point of each epoch image. Then, the convolved reference image was subtracted to yield a difference image. We made the reference frames for each facility since that gives the best result in subtracting the host galaxy. To create the reference images, we stacked images of good qualities (those with the best seeing and image depths) from each facility that had been taken more than 3 months before. When there are not a sufficient number of good reference frames for a certain facility, we used images taken 1 year after the SN discovery that are confirmed to have little signal of SN 2018kp.

An aperture diameter of 2 $\times$ seeing size was adopted to extract magnitudes of sources on the images, using the PS1 catalog as photometry reference (Chambers et al. 2017). The

PS1 adopts *ugrizy* filters. Therefore, when calibrating the images taken in $BVRI$, we to converted the PS1 magnitudes to $BVRI$ following Tonry et al. (2012). As comparison stars, we used stars that have 14 - 19 mag in each band filter, and are inside a 10 arcmin radius circle from the host galaxy. Zero point of an image was obtained by taking a $3-\sigma$ clipped mean values of the zero points from the reference stars, and the error of the zero point is taken as the root-mean-square (rms) of the zero-points. Typical standard deviation value of zero points is 0.02 mag. Then, from the difference images, we extracted fluxes of SN 2018kp with the same aperture.

3.2.4 Host Galaxy Extinction

For the Milky Way galactic reddening, we adopt $E(B-V) = 0.026$ (Schlafly & Finkbeiner 2011). The Galactic extinction corrections are then calculated with this $E(B-V)$ value and the galactic extinction curve of Cardelli et al. (1989) and $R_V = 3.1$. We estimated the host galaxy extinction value with two different methods. The first method uses the SN light curve where the host extinction is embedded in the multi-band light curve fitting. We used the SN(oo)PY2 fitting program (hereafter, SNPY; Burns et al. 2011b) with the EBV_COLOR2 model2, and obtained the R_V and $E(B-V)$ values during the fitting by setting them as free parameters. For the second method, we used the fact that the intrinsic $(B-V)_{peak}$ value is well known, and calculated $E(B-V)$ by comparing the observed $(B-V)_{peak}$ with the intrinsic $(B-V)_{]\mathrm{peak}}$ (Phillips et al. 1999). These two methods give $E(B-V)_{host,SNPY} = 0.608 \pm 0.007$ and $E(B-V)_{host,color} = 0.603 \pm 0.007$, and the two estimates agree with each other within errors. For our analysis below, we adopt the $E(B-V)$ value from SNPY. From the SNPY fitting we also got $R_V = 1.721 \pm 0.134$. Considering that NGC 3367 is a barred spiral galaxy like the Milky Way galaxy, we used the Galactic extinction curve from Fitzpatrick (1999), to obtain the host galaxy extinction corrected magnitudes.

3.3 Results

Table 3.2 presents the result of photometry of SN 2018kp. Note that these magnitudes in Table 3.2 are not corrected for Milky Way Galactic extinction nor host galaxy extinction. The light curves of SN 2018kp in all the filters are shown in Figure 3.3. As comparison, we plotted the SN 2011fe light curve, , and the comparison shows that the light curve shape of SN 2018kp resembles that of SN 2011fe.

3.3.1 Light Curve

The light curves are fitted with SNPY (Burns et al. 2011b, 2014). For the fitting, we used the data points from -10 to +40 days from the $B-$band peak epoch. SNPY has a number of fitting models, and we used the EBV_MODEL2 and MCMC fitting model which can fit the host galaxy extinction parameters simultaneously with a model from Folatelli et al. (2010). Also, we derive other parameters of SN Ia based on Prieto et al. (2006), as they appear in Equation 3.1.

$$m_X(t) = T_Y(t', \Delta m_{15}) + M_Y(\Delta m_{15}) + \mu + R_X E(B-V)_{gal} + R_Y E(B-V)_{host} + K_{X,Y} \tag{3.1}$$

Here, X, Y are the observed filters, Δm_{15} is the decline rate parameter from Phillips et al. (1999), m is the observed apparent magnitudes at a time t, $R_{X,Y}$ is the total to selective absorption and $K_{X,Y}$ is the k-correction term. NGC 3367 is close to our Galaxy, therefore, we neglect k-correction term. The fitted results are summarized in Table 3.1 and Figure 3.4 is for the SNPY model fit results of the SN 2018kp light curve.
During the fitting, we assumed $H_0 = 70\,km\,s^{-1}\,Mpc^{-1}$, and the distance modulus is found to be 33.44. $T_{B,Max}$ is MJD = 58159.614±0.064 and the rise time (from estimated explosion time to $T_{B,Max}$), t_{rise} is 18.28 ± 0.540 days. We also found Δm_{15} = 1.027 ± 0.005, $M_{B,Max}$ value of 14.682 ± 0.101, and $M_{B,Max}$ = -19.75 mag. As we mentioned above, $E(B-V)$ is found to be 0.608.
Compared to SN 2011fe (Pereira et al. 2013), SN 2018kp has $\Delta m_{15} = 1.103$, $M_{B,Max} =$

-19.75 than $M_{B,Max} = 19.10$ of SN 2011fe, indicating that SN 2018kp is brighter than SN 2011fe. The stretch parameter $S_{BV} = 0.963$ is similar to the SN 2011fe of 0.969. Figure 3.5 shows the distribution of $M_{B,Max}$ versus Δm_{15} of various SNe Ia. The SN 2018kp locates in the region of normal SNe Ia, and it has properties consistent with the Phillips relation area (Alsabti & Murdin 2017). Furthermore, we can see that SN 2018kp is a bit brighter than SN 2011fe.

3.3.2 Early Light Curve

We examine the early light curve carefully to determine the progenitor star property of SN 2018kp. Figure 3.6 shows the early light curve in $V-$ and $R-$bands. We emphasize that the R-band has an extensive coverage in early epochs, and can be used to set a useful limit on the companion star size from SHE.

To analyze the data, we first try a single power-law fitting of the light curve with the luminosity evolving as $\sim t^{\alpha}$. The power law fit can tell us if an additional SHE component is necessary, and an estimate of the first light epoch (defined as the start of the emission originating from the radio-active decay). We tried both a fireball model with $\alpha = 2$, and also setting α free. For the fitting, data points at MJD < 58156 days is used (roughly within 14 days from the discovery report).

We find that both the fittings with the fixed and free α give reasonable fits to the early light curve data with the reduced χ^2 of about 0.7 to 2.5. The α values are found to be $\alpha = 1.6 \pm 0.1$ for the $V-$band, and $\alpha = 1.7 \pm 0.1$ for the R-band. The first light time inferred from these fits are MJD = 58139.773 for the $\alpha = 2$ fit, and MJD = 58140.863 days for the free α fit.

However, from a close examination of the $R-$band light curve, we find that the fixed α fit is only marginally consistent with the non-detections upper limits before the first detection. Also, the first detection point lie above the free α power-law best fit light curve, providing a possibility that the excess is caused by SHE.

To further investigate what is a possible amount of SHE allowed by the first detection point, we plot the SHE model of Kasen (2010). on both V and R band early

Table 3.1. Parameters and values estimated from analysis of SN 2018kp

Parameter	Value	Error	Unit	Method
DM(μ)	34.441	0.165	Mag	SNPY
$T_{B.Max}$	58159.614	0.064	MJD	SNPY
$E(B-V)$	0.608	0.007	Mag	SNPY
Δm_{15}	1.027	0.005	Mag	SNPY
R_V	1.721	0.134		SNPY
S_{BV}	0.963	0.030		SNPY
B_{Max}	14.682	0.101	Mag	SNPY
t_0	58140.863	0.146	MJD	power law fit
α	1.64	0.100		power law fit
t_{rise}	18.281	0.540	Day	power law fit
M_{Ni}	0.684	0.104	$M_\odot$	Bolometic LC
M_{ej}	1.121	0.022	$M_\odot$	Bolometic LC
E_k	1.23	0.24	10^{51} ergs	Bolometic LC

Note. — For μ, we assume $H_0 = 70 km/s/Mpc$. S_{BV} is the color stretch from Burns et al. (2011b)

light curves. We find that a model with the companion star radius of 4 $R_{\odot}$ fits the first detection point well, suggesting that this can be an upper limit on the companion star size. Note that the SHE is not isotropic in the Kasen (2010) model, and the plotted model curve is for the optimal viewing angle for detecting SHE. If a more common angle is adopted (usually about 10 times less luminous than SHE from the optimal viewing angle), a larger companion star size is allowed. This model is plotted too, suggesting that the maximally allowed companion size is 700 $R_{\odot}$.

Piro & Nakar (2014) argued that the power index should not be exactly 2 rather than ~ 1.5 since early light curve is dominated by Ni decay, the slope α may depends on nickel distribution and mixing degree or asymmetric geometry of explosion. Also there are pieces of evidence indicating that the single power law index of SNe Ia distributes from 1.0 - 2.5 (Miller et al. 2018). So $\alpha = 1.47$ is plausible. We drive the explosion time $t_0 = 58140.863$ which is identical to the first light time. The rise time t_{rise} from explosion time to $T_{B,Max}$ is 18.75 $\pm$ 0.540. Firth et al. (2015) compiled 18 early light curve and found that mean rise time of them as 18.98 $\pm$ 0.54 which is consistent well with the value of SN 2018kp.

3.3.3 Bolometric Light curve

We constructed the bolometric luminosity light curve using SNPY. SNPY can reconstruct the bolometric luminosity light curve from the light curve fitting parameters and utilizing model SED (SED method; Hsiao et al. 2017), and also provide the light curve point at each epoch utilizing B and V band data points. Both methods are used. Figure 3.7 shows the bolometric luminosity light curve from SNPY. We derived the explosion parameters such as the nickel mass M_{Ni}, ejeta mass M_{ej} and kinetic energy E_k following the ways described in Scalzo et al. (2019). There are statistical relations between color stretch value and the explosion parameters extracted from CSP-I + CfA SN Ia data set (Hicken et al. 2009). SN 2018kp values follow that relation well with other normal type Ia SNe. We got the values of $M_{Ni} = 0.684 \pm 0.104$ $M_{\odot}$, $M_{ej} = 1.121 \pm 0.022$ $M_{\odot}$ and $E_k = 1.23 \pm 0.24 \times 10^{51}$ ergs, assuming an expansion velocity

of 10,500 km/s. These results suggested that SN 2018kp is a sub-Chandrasekhar mass progenitor star explosion. Compared to SN 2011fe ($M_{Ni} = 0.42$, $M_\odot$, $M_{ej} = 1.24$ $M_\odot$), from Scalzo et al. (2014), SN 2018kp resembles SN 2011fe on light curve and on explosion parameters from the bolometric light curve. M_{Ni} of SN 2011fe is 0.44, a bit less than SN 2018kp. E_k of SN 2011fe is 1.17×10^{51} $ergs$, similar to SN 2018kp.

3.4 Discussion

SN 2018kp appears to have somewhat large host galaxy extinction value $E(B-V)_{host} = 0.608$ which corresponds to $A_V = 1.00$ and $A_B = 1.61$ given R_V of 1.7. We examined late phase color curve to infer the host galaxy extinction value through the Lira law of Phillips et al. (1999) on Figure 3.8. It is known that the late time slope of SN Ia $B-V$ color (from B band peak to 80 days) depends on the dust extinction in line of sight. From fitting of the late $B-V$ color curve, we obtained $E(B-V)_{host} = 0.603 \pm 0.021$ that agrees with other methods. We suspect that SN 2018kp is located in a star forming region suffering a large extinction values. Burns et al. (2014) found that regions with a larger $E(B-V)$ value tend to have a lower R_V. For $E(B-V)_{host} = 0.603$, their calculated value is $R_V = 1.7$, which validates our estimates. If we take $R_V = 3.1$ of Milky Way, we get $A_V = 3.1 \times 0.6 = 1.9$ which is larger than A_V from $R_V = 1.7$ by 0.9. If this is true, the peak luminosity of SN 2018kp would be much brighter, and SN 2018kp becomes a bright outlier from the Phillips relation. The host galaxy extinction can play a large role in estimation of physical parameters, that might contribute distance measurement and explosion parameters. From early light curve analysis, radius constrain of size upper limit can be set 4 $R_\odot$, which can rule out giant star or supergiant companion star. Note that fitting Kasen (2010) model we took optimal angle giving maximum value. Both DD scenario, or SD scenario of main sequence or subgiant star is plausible.

Piro & Nakar (2014) argued that Ni-decay powered SNe have dark phase $\sim$ 2 days because of existence of γ-ray photon diffusion time inside optically thick photosphere. If exact explosion time closer to first light time (MJD = 58142.247) upper limit can be

bigger than estimated value. We plot $(V-R)_0$ color comparing with the Kasen (2010) models which have different mass companion stars on Figure 3.9. SN 2018kp color curve looks similar to SN 2011fe. However, to verify the companion size or existence of interaction, unfortunately we missed earlier data close to explosion time which is able to decide model dependency. We could not found early excess such as shock cooling emission feature in early time light curve, but the earliest point slightly brighter than single power law. That is on -12 days from $T_{B,Max}$, error of that point is large of 0.28, so missing data points to confirm early excess makes it hard for us to look into further. Moreover recent studies focused on early time light curve shed light on physical properties of progenitor star like Ni mixing, explosion mechanism, CSM-ejecta interaction (Noebauer et al. 2017; Könyves-Tóth et al. 2020). To verify diverse models related those physical properties, photometric data that is closer to explosion time is necessary.

3.5 Conclusion

In this paper, we present the results of photometric analaysis of optical light curve of SN 2018kp including early phase. Data coverage of NGC 3367 with daily cadence provides well sampled optical light curve of SN 2018kp. The explosion time t_0 is 58140.261 from single power law fit, earlier than first light time by 2 days. Long term light curve fitting gives us the distance modulus to NGC 3367 of 33.31 with $H_0 = 70$ km/s/Mpc. Host galaxy extinction $E(B-V)_{host} = 0.608 \pm 0.007$ and its reddening parameter $R_V = 1.721 \pm 0.134$ are derived. The other light curve parameters we computed indicate that SN 2018kp is normal type Ia SN such as SN 2011fe. Most of all, we set constraint the size of progenitor system upper limit by 4 $R_\odot$. That can rule out giant or supergiant star, but main sequence or subgiant star companion WD may be the companion star of its progenitor. There were potential shock cooling emission feature was shown. We look forward to have more samples catching very early phase close to explosion time to study the appropriate properties of SN Ia progenitor system.

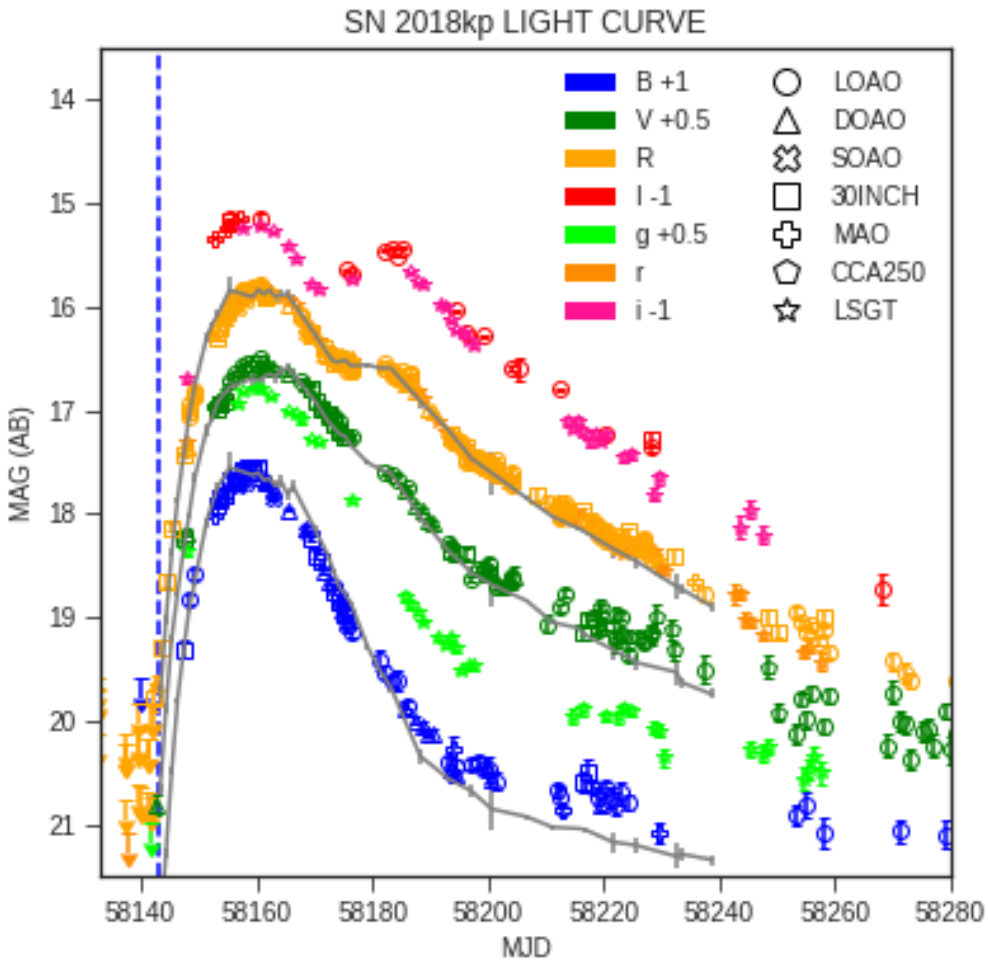

Figure 3.3. Multi-band light curve of SN 2018kp. The gray lines are the SN 2011fe BVR light curve (Vinkó et al. 2012) for comparison.

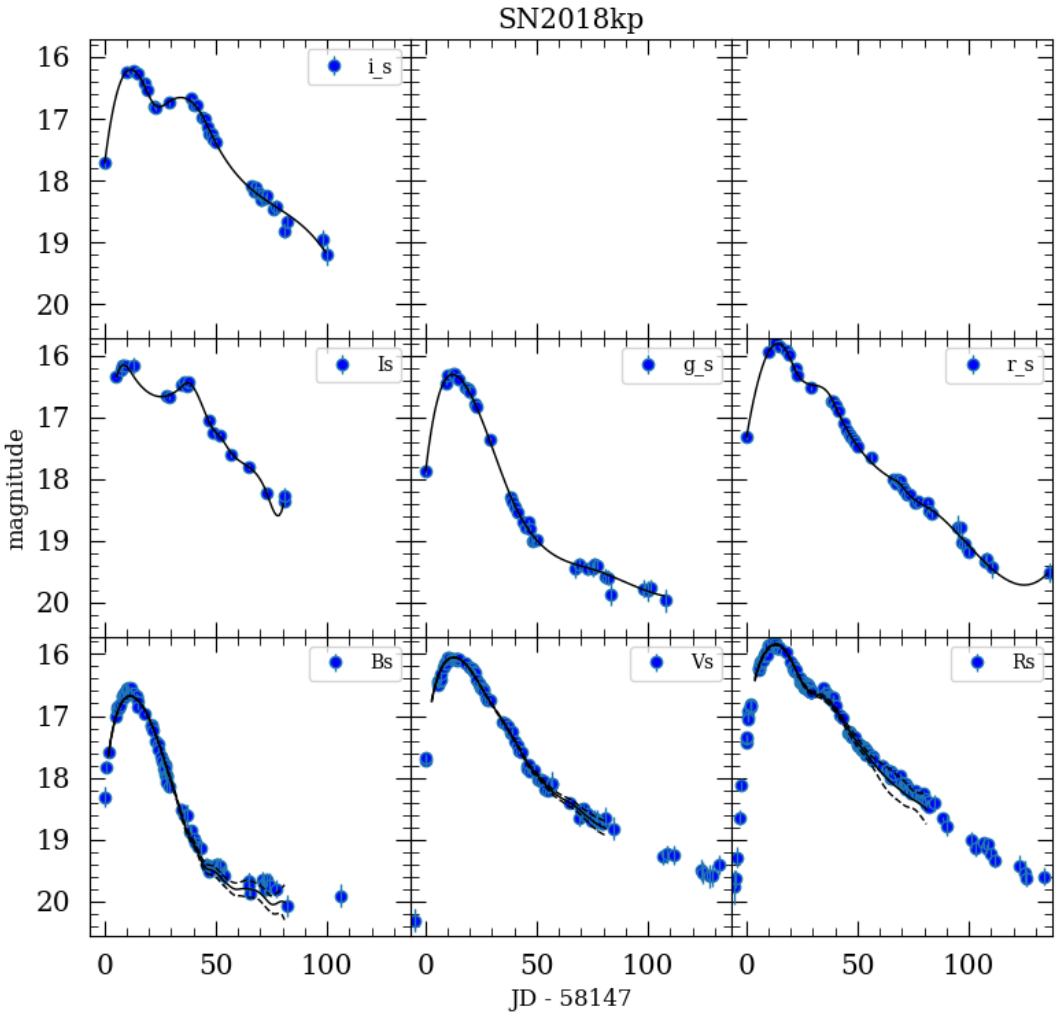

Figure 3.4. Light curve fitting with SNPY.

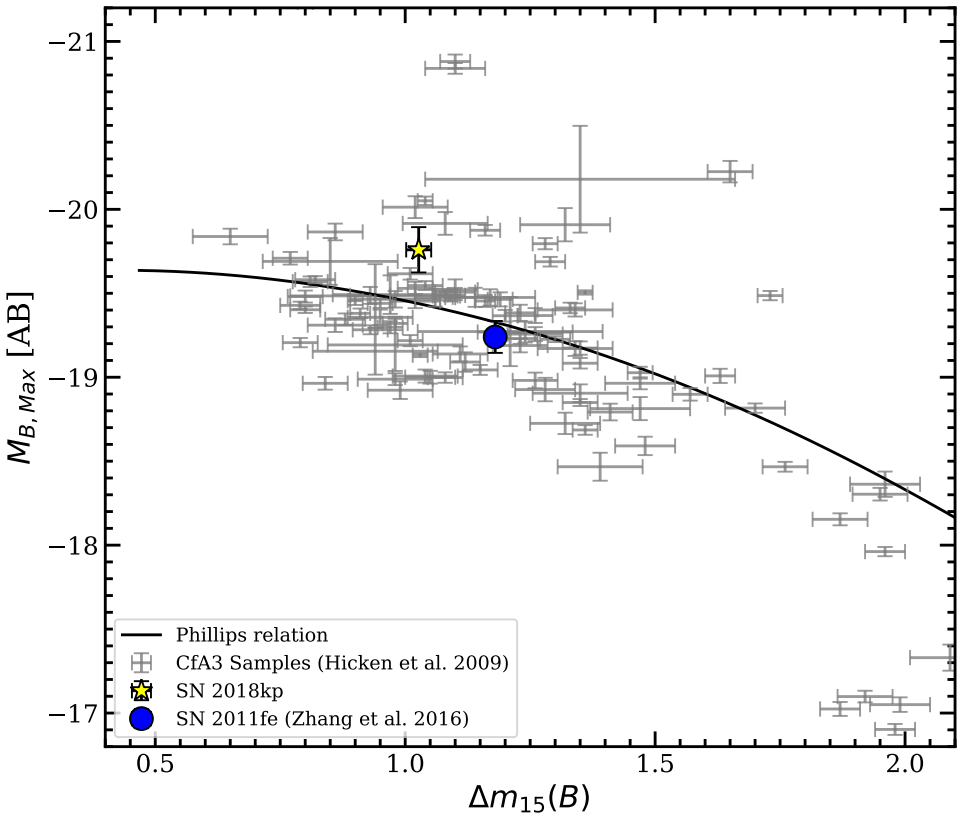

Figure 3.5. The distribution of Δm_{15} versus $M_{B,Max}$, adopted from Alsabti & Murdin (2017). Red Star show the position of SN 2018kp.

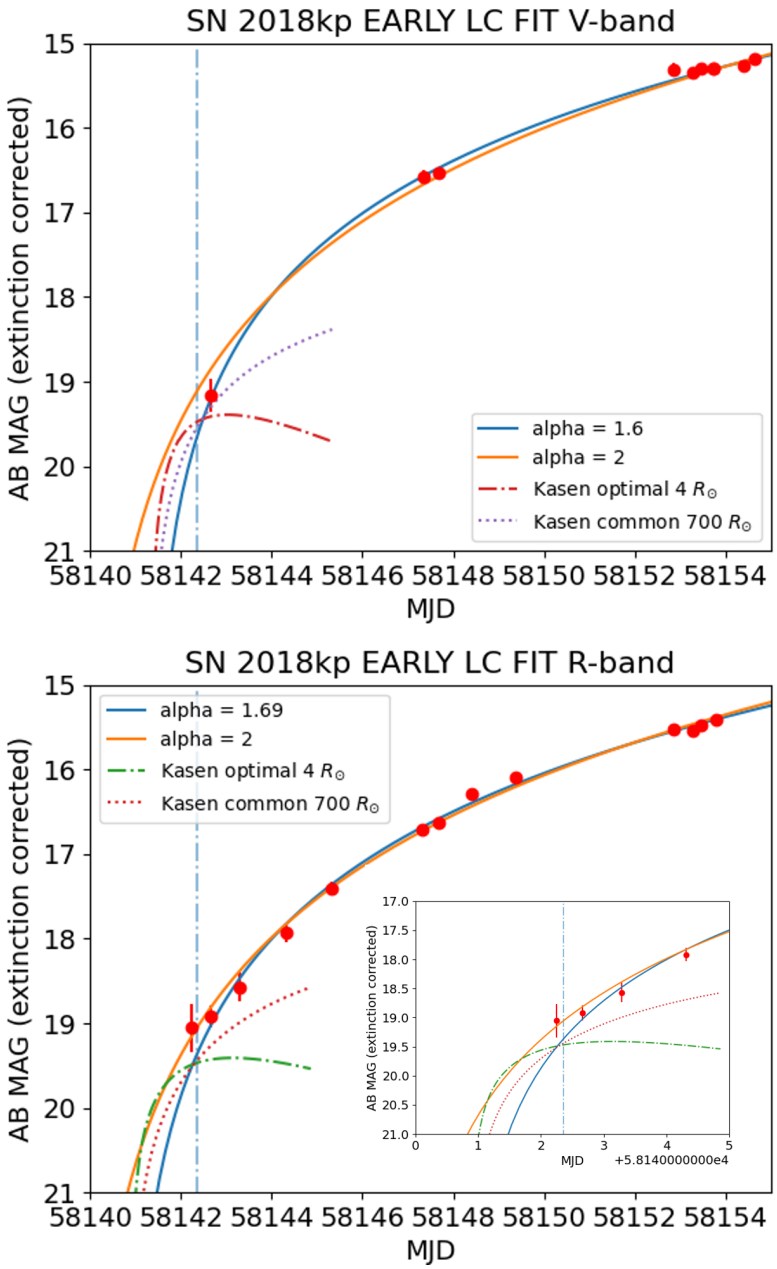

Figure 3.6. The early light curves of SN 2018kp. The upper is for $V-$ band, and the lower is for the $R-$band. In R band, the magnified region around the first light is shown in inset. The orange solid lines are single power law model line of $\alpha = 2$ and free α. Blue vertical dash dotted line is the discovery date. The data points denoted by red circles are corrected for the MW and host galaxy extinctions. The dot-dashed line is from the model of 4 $R_\odot$ Kasen (2010) in optimal angle. The dot-dashed line is from the model of 700 $R_\odot$ in common angle Kasen (2010).

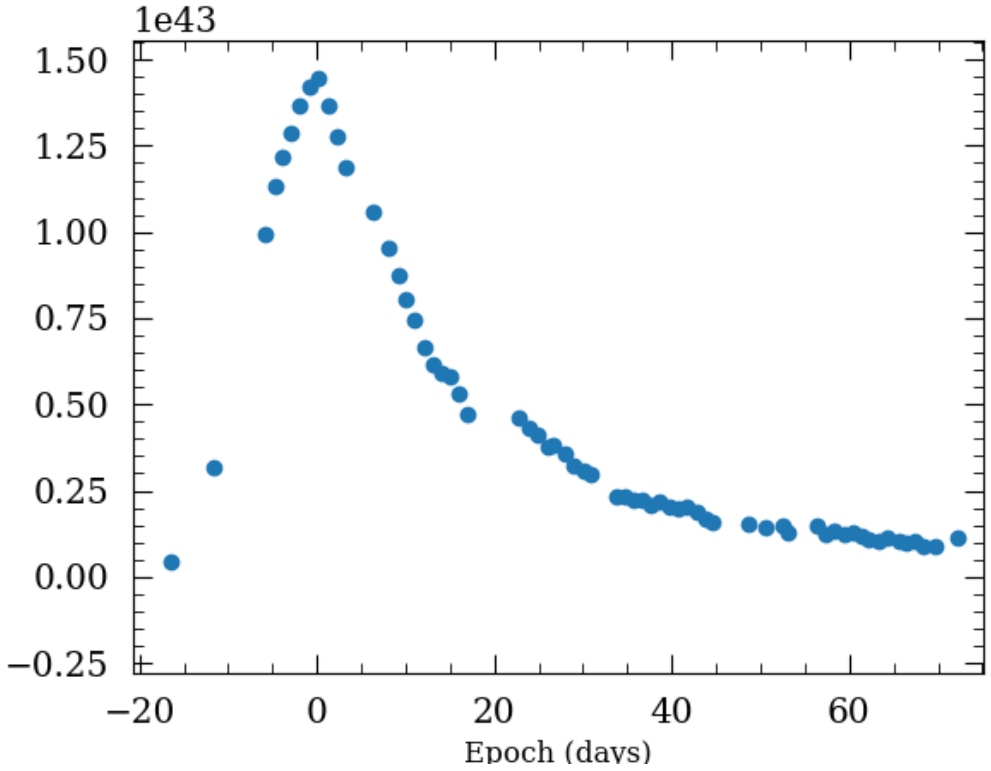

Figure 3.7. Bolometric luminosity light curve from SNPY. The blue dots are points from the model based on the spectral template of Hsiao et al. (2007).

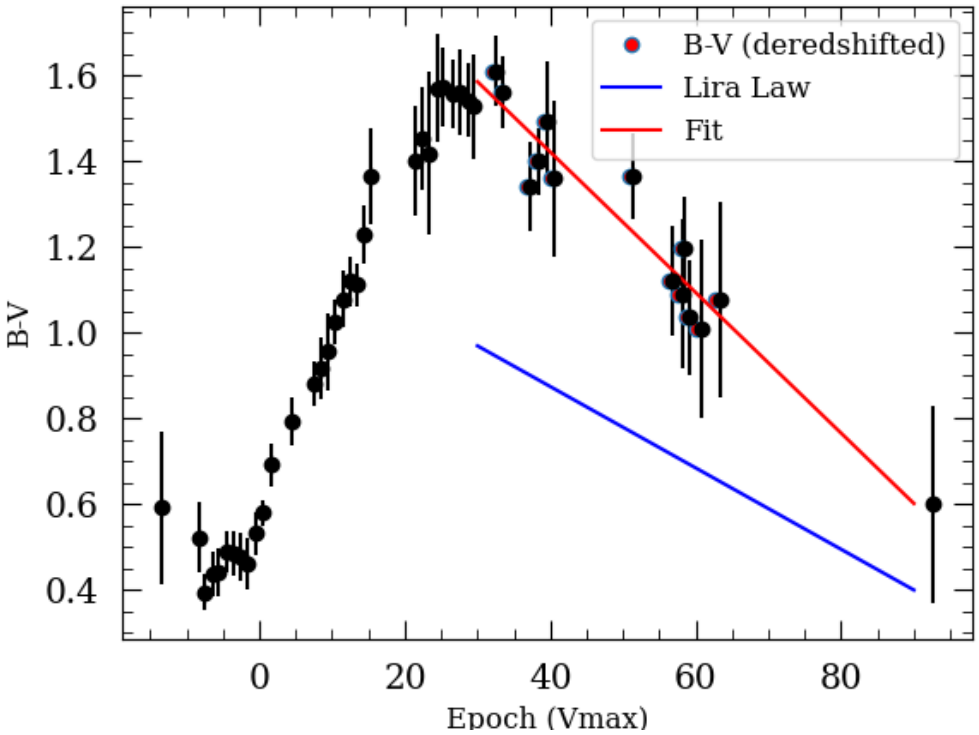

Figure 3.8. $B-V$ color Curve of SN 2018kp. The blue and red lines are the $B-V$ color slope (the Lira relation) without extinction, and the color curve with $E(B-V) = 0.6$, respectively.

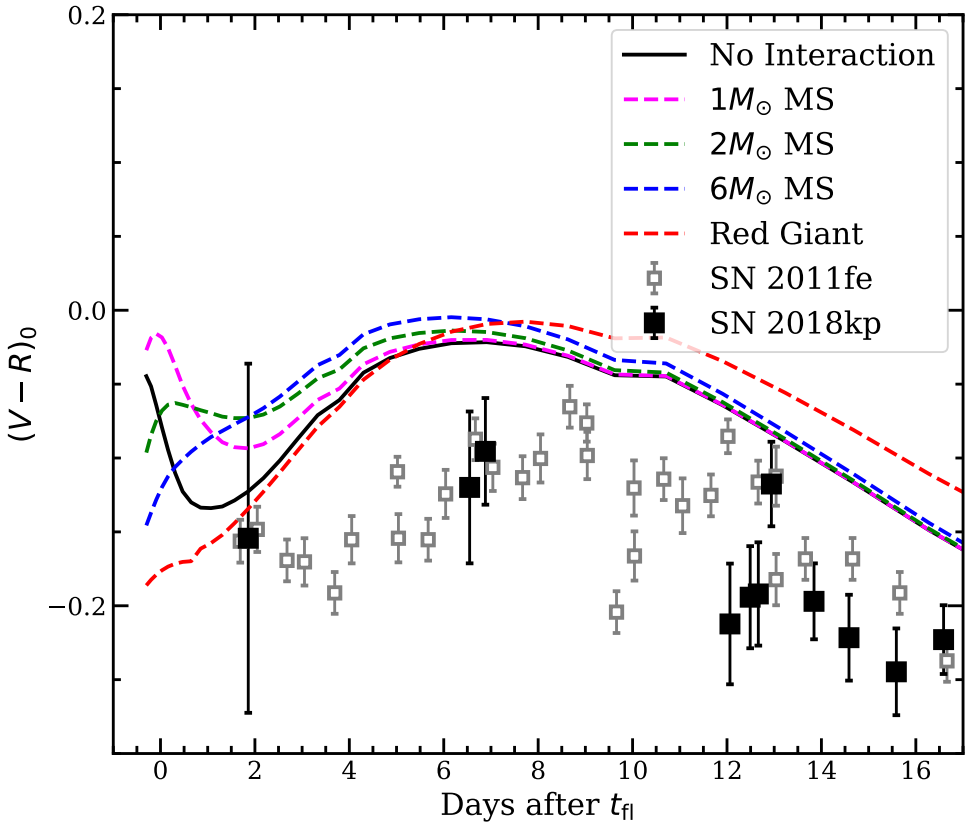

Figure 3.9. $(V-R)_0$ curve comparison with Kasen (2010) model, grey square shows the color of SN 2011fe, black square shows SN 2018kp color. The color itself looks like SN 2011fe.

Table 3.2. Photometry of SN 2018kp

MJD	MAG	ERROR	UL5	OBS	FILTER
58126.32			18.15	LOAO	R
58128.70			22.26	DOAO	R
58131.30			20.86	LOAO	R
58132.26			20.13	LOAO	R
58137.38			20.75	MCD30INCH	R
58137.62			21.07	LSGT	r
58139.29			20.60	MCD30INCH	R
58139.93			19.58	MAO_FLI	B
58139.93			20.65	MAO_FLI	R
58141.31			20.69	MCD30INCH	R
58141.60			20.99	LSGT	g
58141.82			19.50	SOAO	R
58142.24			19.84	MCD30INCH	R
58142.25	19.77	0.28	20.43	MCD30INCH	R
58142.66	20.31	0.19	22.13	DOAO	V
58142.66			21.53	DOAO	B
58142.66	19.64	0.14	21.79	DOAO	R
58143.29	19.29	0.17	20.44	MCD30INCH	R
58144.32	18.64	0.11	20.41	MCD30INCH	R
58145.31	18.13	0.08	20.30	MCD30INCH	R
58147.33	17.42	0.05	19.92	MCD30INCH	R
58147.34	18.31	0.17	19.40	MCD30INCH	B
58147.35	17.73	0.09	19.72	MCD30INCH	V
58147.64	17.87	0.08	19.91	LSGT	g
58147.65	17.32	0.05	19.85	LSGT	r
58147.65	17.7	0.09	19.50	LSGT	i
58147.68	17.35	0.04	21.21	DOAO	R
58147.68	17.68	0.06	21.07	DOAO	V
58148.40	17.83	0.10	19.72	LOAO	B
58148.41	17.01	0.05	20.19	LOAO	R
58149.37	17.58	0.10	19.17	LOAO	B
58149.37	16.81	0.07	19.04	LOAO	R
58152.86	17.00	0.02	19.78	MAO_FLI	B
58152.86	16.24	0.02	20.72	MAO_FLI	R

Table 3.2 (cont'd)

MJD	MAG	ERROR	UL5	OBS	FILTER
58152.86	16.46	0.08	20.70	MAO_FLI	V
58152.86	16.34	0.03	20.37	MAO_FLI	I
58153.27	16.26	0.04	19.64	MCD30INCH	R
58153.28	16.91	0.08	19.34	MCD30INCH	B
58153.29	16.49	0.06	19.56	MCD30INCH	V
58153.45	16.20	0.04	19.91	MCD30INCH	R
58153.46	16.44	0.06	19.72	MCD30INCH	V
58153.47	16.85	0.07	19.45	MCD30INCH	B
58153.74	16.16	0.03	21.31	DOAO	R
58153.74	16.87	0.04	21.14	DOAO	B
58153.74	16.44	0.04	21.14	DOAO	V
58153.80	16.13	0.04	20.48	SOAO	R
58154.40	16.81	0.07	19.77	MCD30INCH	B
58154.41	16.41	0.06	20.06	MCD30INCH	V
58154.64	16.32	0.04	21.29	DOAO	V
58154.64	16.83	0.05	21.28	DOAO	B
58154.65	16.09	0.03	21.23	DOAO	R
58154.88	16.10	0.02	20.93	MAO_FLI	R
58154.88	16.24	0.08	20.13	MAO_FLI	I
58155.33	16.17	0.05	20.31	MCD30INCH	B
58155.35	16.67	0.11	18.61	MCD30INCH	V
58155.38	16.68	0.04	20.53	LOAO	B
58155.38	16.21	0.04	20.81	LOAO	V
58155.39	16.16	0.03	20.64	LOAO	I
58155.39	16.03	0.03	21.02	LOAO	R
58155.39	16.01	0.04	20.51	LOAO	R
58156.32	16.69	0.07	19.73	MCD30INCH	B
58156.38	16.64	0.04	20.78	LOAO	B
58156.39	16.15	0.05	20.89	LOAO	V
58156.39	15.96	0.04	20.39	LOAO	R
58156.63	16.44	0.03	19.90	LSGT	g
58156.78	16.01	0.03	21.17	SOAO	R
58156.92	16.14	0.05	20.90	MAO_FLI	V
58156.92	16.66	0.07	19.89	MAO_FLI	B

Table 3.2 (cont'd)

MJD	MAG	ERROR	UL5	OBS	FILTER
58156.93	16.16	0.04	20.59	MAO_FLI	I
58157.36	16.57	0.10	18.38	MCD30INCH	B
58157.38	16.57	0.04	21.03	LOAO	B
58157.39	15.86	0.02	21.21	LOAO	R
58157.39	16.06	0.04	21.11	LOAO	V
58157.63	16.32	0.02	21.14	LSGT	g
58157.64	15.94	0.02	20.94	LSGT	r
58157.64	16.24	0.03	20.35	LSGT	i
58158.23	16.55	0.06	19.96	MCD30INCH	B
58158.37	16.56	0.03	21.14	LOAO	B
58158.38	16.05	0.05	20.67	LOAO	V
58158.38	15.85	0.02	20.97	LOAO	R
58159.27	16.60	0.06	20.65	MCD30INCH	B
58159.38	16.56	0.04	20.10	LOAO	B
58159.38	16.09	0.05	19.68	LOAO	V
58159.38	15.82	0.04	20.55	LOAO	R
58159.65	16.29	0.03	20.86	LSGT	g
58160.38	15.85	0.04	19.78	LOAO	R
58160.39	16.16	0.13	17.34	LOAO	I
58160.39	15.82	0.04	19.88	LOAO	R
58160.58	16.09	0.03	21.41	DOAO	V
58160.58	16.64	0.04	21.23	DOAO	B
58160.58	15.83	0.02	21.49	DOAO	R
58160.64	16.30	0.02	21.53	LSGT	g
58160.65	15.79	0.02	21.19	LSGT	r
58160.65	16.23	0.04	20.39	LSGT	i
58161.36	16.08	0.06	17.60	CCA250	V
58161.36	15.90	0.05	18.95	MCD30INCH	R
58161.57	16.09	0.04	22.25	DOAO	V
58161.57	16.70	0.04	22.09	DOAO	B
58161.58	15.91	0.02	22.35	DOAO	R
58161.61	16.07	0.04	20.74	DOAO	V
58161.61	16.68	0.05	21.46	DOAO	B
58161.61	15.89	0.02	21.31	DOAO	R

Table 3.2 (cont'd)

MJD	MAG	ERROR	UL5	OBS	FILTER
58161.65	16.08	0.04	21.87	DOAO	V
58161.65	15.89	0.02	22.04	DOAO	R
58161.65	16.68	0.04	21.87	DOAO	B
58162.56	16.38	0.02	21.47	LSGT	g
58162.56	15.85	0.02	21.08	LSGT	r
58162.57	16.28	0.04	20.30	LSGT	i
58162.59	16.77	0.04	21.98	DOAO	B
58162.59	16.09	0.04	21.92	DOAO	V
58162.59	15.89	0.02	22.12	DOAO	R
58162.65	16.85	0.05	19.40	SOAO	B
58165.56	16.51	0.02	21.44	LSGT	g
58165.56	15.93	0.02	21.03	LSGT	r
58165.57	16.41	0.05	20.29	LSGT	i
58165.59	16.14	0.04	21.76	DOAO	V
58165.59	16.96	0.04	21.65	DOAO	B
58165.59	15.97	0.02	21.95	DOAO	R
58166.56	16.54	0.01	21.42	LSGT	g
58166.57	15.99	0.02	20.94	LSGT	r
58166.57	16.54	0.04	20.12	LSGT	i
58167.49	16.22	0.05	20.28	LOAO	V
58167.49	16.11	0.03	20.75	LOAO	R
58167.55	16.59	0.11	17.71	LSGT	g
58168.63	16.19	0.02	22.10	DOAO	R
58168.63	16.24	0.04	21.95	DOAO	V
58168.63	17.14	0.04	21.74	DOAO	B
58168.68	17.16	0.07	17.15	SOAO	B
58168.69	16.24	0.08	16.16	SOAO	R
58169.34	16.28	0.03	20.79	MCD30INCH	R
58169.35	16.28	0.05	20.58	MCD30INCH	V
58169.36	17.23	0.06	20.71	MCD30INCH	B
58169.47	16.30	0.05	20.70	MCD30INCH	V
58169.48	16.25	0.04	20.64	MCD30INCH	R
58169.53	16.78	0.02	21.27	LSGT	g
58169.54	16.21	0.02	20.79	LSGT	r

Table 3.2 (cont'd)

MJD	MAG	ERROR	UL5	OBS	FILTER
58169.55	16.79	0.04	20.09	LSGT	i
58170.31	16.42	0.06	20.18	MCD30INCH	V
58170.32	17.40	0.07	20.50	MCD30INCH	B
58170.54	16.82	0.02	21.49	LSGT	g
58170.55	16.32	0.02	21.01	LSGT	r
58170.56	16.83	0.04	20.43	LSGT	i
58171.34	17.46	0.07	20.13	MCD30INCH	B
58171.35	16.48	0.06	19.85	MCD30INCH	V
58171.36	16.40	0.03	20.69	MCD30INCH	R
58171.56	17.55	0.05	21.43	DOAO	B
58171.57	16.47	0.04	21.43	DOAO	V
58171.57	16.40	0.02	21.66	DOAO	R
58171.58	16.46	0.03	21.65	SOAO	R
58172.23	16.45	0.04	20.48	MCD30INCH	R
58172.24	16.54	0.06	20.31	MCD30INCH	V
58172.61	17.65	0.06	20.95	DOAO	B
58172.61	16.55	0.04	21.02	DOAO	V
58172.61	16.48	0.03	21.30	DOAO	R
58173.31	16.55	0.04	20.42	MCD30INCH	R
58173.33	17.74	0.09	20.24	MCD30INCH	B
58173.45	16.49	0.03	20.97	LOAO	R
58173.45	17.71	0.06	20.71	LOAO	B
58173.45	16.59	0.05	20.96	LOAO	V
58173.45	16.51	0.04	20.43	LOAO	R
58174.32	16.52	0.04	20.23	MCD30INCH	R
58174.33	17.85	0.12	19.40	MCD30INCH	B
58174.43	17.80	0.05	20.81	LOAO	B
58174.57	17.94	0.08	19.38	SOAO	B
58174.59	17.81	0.07	20.81	DOAO	B
58174.59	16.71	0.04	20.92	DOAO	V
58174.66	17.86	0.07	21.05	DOAO	B
58174.66	16.49	0.03	21.23	DOAO	R
58175.19	16.55	0.04	19.83	MCD30INCH	R
58175.20	17.97	0.15	19.46	MCD30INCH	B

Table 3.2 (cont'd)

MJD	MAG	ERROR	UL5	OBS	FILTER
58175.39	16.58	0.04	19.86	LOAO	R
58175.39	17.97	0.08	20.03	LOAO	B
58175.39	16.75	0.05	20.27	LOAO	V
58175.39	16.56	0.04	20.39	LOAO	R
58175.39	16.56	0.04	19.90	LOAO	R
58175.40	16.64	0.03	20.03	LOAO	I
58175.57	18.01	0.07	20.76	DOAO	B
58175.57	16.52	0.03	20.97	DOAO	R
58175.58	18.08	0.12	19.13	SOAO	B
58175.59	16.50	0.03	21.16	SOAO	R
58176.33	18.14	0.10	19.90	LOAO	B
58176.34	16.61	0.04	20.27	LOAO	R
58176.37	16.75	0.05	20.09	LOAO	V
58176.38	16.68	0.03	19.98	LOAO	I
58176.38	16.60	0.04	20.22	LOAO	R
58176.54	17.37	0.06	19.68	LSGT	g
58176.54	16.53	0.04	19.48	LSGT	r
58176.55	16.74	0.06	18.97	LSGT	i
58182.32	18.53	0.12	19.84	LOAO	B
58182.33	16.60	0.04	20.42	LOAO	R
58182.33	17.10	0.05	20.22	LOAO	V
58182.33	16.46	0.03	20.20	LOAO	I
58183.31	18.61	0.11	20.28	LOAO	B
58183.32	16.63	0.04	20.28	LOAO	R
58183.32	17.13	0.05	20.06	LOAO	V
58183.32	16.43	0.03	20.38	LOAO	I
58184.32	18.61	0.18	19.34	LOAO	B
58184.33	17.17	0.06	19.81	LOAO	V
58184.33	16.67	0.03	20.76	LOAO	R
58184.33	16.50	0.03	20.25	LOAO	I
58185.31	16.43	0.03	19.38	LOAO	I
58185.58	18.87	0.12	21.49	DOAO	B
58185.59	17.28	0.04	21.65	DOAO	V
58185.59	16.73	0.02	21.90	DOAO	R

Table 3.2 (cont'd)

MJD	MAG	ERROR	UL5	OBS	FILTER
58185.65	18.29	0.10	19.96	LSGT	g
58185.66	16.73	0.04	19.78	LSGT	r
58186.21	16.71	0.03	20.59	LOAO	R
58186.21	18.85	0.07	20.84	LOAO	B
58186.21	17.25	0.06	20.45	LOAO	V
58186.65	18.37	0.10	19.78	LSGT	g
58186.66	16.74	0.03	20.12	LSGT	r
58186.66	16.67	0.03	20.00	LSGT	i
58187.56	18.99	0.07	21.94	DOAO	B
58187.56	17.41	0.04	22.05	DOAO	V
58187.56	16.82	0.02	22.09	DOAO	R
58187.65	18.45	0.05	21.07	LSGT	g
58187.66	16.81	0.02	20.87	LSGT	r
58187.66	16.77	0.04	20.32	LSGT	i
58188.56	17.47	0.04	21.64	DOAO	V
58188.56	19.06	0.09	21.47	DOAO	B
58188.65	18.54	0.04	21.19	LSGT	g
58188.65	16.89	0.03	20.89	LSGT	r
58188.66	16.78	0.04	20.29	LSGT	i
58189.70	19.12	0.07	21.74	DOAO	B
58189.71	17.56	0.04	21.69	DOAO	V
58189.72	16.98	0.02	21.79	DOAO	R
58190.51	17.58	0.04	21.61	DOAO	V
58190.51	19.14	0.11	21.03	DOAO	B
58190.51	17.02	0.02	21.91	DOAO	R
58191.55	18.69	0.06	20.97	LSGT	g
58191.56	17.10	0.02	21.21	LSGT	r
58191.57	16.97	0.04	20.61	LSGT	i
58192.51	18.77	0.05	21.52	LSGT	g
58192.52	17.20	0.02	21.02	LSGT	r
58192.53	17.00	0.03	20.49	LSGT	i
58193.32	17.80	0.06	20.55	LOAO	V
58193.32	19.41	0.12	20.66	LOAO	B
58193.32	17.28	0.05	20.11	LOAO	R

Table 3.2 (cont'd)

MJD	MAG	ERROR	UL5	OBS	FILTER
58193.36	17.86	0.08	20.17	MCD30INCH	V
58193.51	18.70	0.05	21.43	LSGT	g
58193.52	17.27	0.02	21.05	LSGT	r
58193.53	17.14	0.04	20.57	LSGT	i
58193.59	19.46	0.10	21.89	DOAO	B
58193.59	17.79	0.04	22.02	DOAO	V
58193.60	17.26	0.02	22.13	DOAO	R
58193.92	17.28	0.03	20.73	MAO_FLI	R
58194.34	17.29	0.03	20.94	LOAO	R
58194.34	19.43	0.10	21.05	LOAO	B
58194.35	17.04	0.04	20.23	LOAO	I
58194.51	18.80	0.05	21.41	LSGT	g
58194.52	17.32	0.02	21.03	LSGT	r
58194.52	19.51	0.10	21.88	DOAO	B
58194.52	17.89	0.04	21.83	DOAO	V
58194.53	17.24	0.03	20.52	LSGT	i
58194.53	17.32	0.02	21.98	DOAO	R
58195.27	17.32	0.03	20.95	LOAO	R
58195.52	19.01	0.07	21.42	LSGT	g
58195.52	17.36	0.02	21.04	LSGT	r
58195.53	17.25	0.03	20.55	LSGT	i
58196.27	17.24	0.04	20.68	LOAO	I
58196.37	17.88	0.10	19.99	MCD30INCH	V
58196.38	17.35	0.04	20.49	MCD30INCH	R
58196.51	18.98	0.05	21.52	LSGT	g
58196.52	17.41	0.03	20.96	LSGT	r
58196.53	17.33	0.04	20.39	LSGT	i
58197.25	19.41	0.10	21.13	LOAO	B
58197.26	17.47	0.03	21.00	LOAO	R
58197.26	17.44	0.05	20.47	LOAO	R
58197.52	18.98	0.06	21.17	LSGT	g
58197.53	17.47	0.03	20.82	LSGT	r
58197.53	17.38	0.04	20.23	LSGT	i
58198.24	18.03	0.05	20.88	LOAO	V

Table 3.2 (cont'd)

MJD	MAG	ERROR	UL5	OBS	FILTER
58198.24	17.50	0.03	21.00	LOAO	R
58198.24	19.40	0.09	20.69	LOAO	B
58199.23	19.48	0.09	20.75	LOAO	B
58199.24	17.53	0.02	21.05	LOAO	R
58199.24	18.03	0.05	21.05	LOAO	V
58199.25	17.28	0.03	20.52	LOAO	I
58199.49	19.42	0.12	21.52	DOAO	B
58199.49	18.04	0.05	21.56	DOAO	V
58199.50	17.53	0.02	21.55	DOAO	R
58199.59	18.05	0.05	21.94	DOAO	V
58199.60	17.55	0.03	21.88	DOAO	R
58200.21	17.49	0.05	20.49	LOAO	R
58200.32	17.52	0.04	20.56	MCD30INCH	R
58200.49	19.57	0.13	21.50	DOAO	B
58200.49	18.05	0.05	21.51	DOAO	V
58200.50	17.58	0.03	21.77	DOAO	R
58201.32	17.58	0.05	20.52	MCD30INCH	R
58201.42	19.58	0.17	20.69	LOAO	B
58201.42	18.20	0.07	20.71	LOAO	V
58201.42	17.59	0.05	20.78	LOAO	R
58201.50	17.59	0.06	20.46	DOAO	R
58202.52	17.62	0.04	21.08	DOAO	R
58202.52	18.21	0.07	20.98	DOAO	V
58203.52	17.66	0.05	20.68	DOAO	R
58203.52	17.65	0.08	20.02	LSGT	r
58204.27	17.71	0.08	19.56	LOAO	R
58204.27	18.11	0.09	19.94	LOAO	V
58204.28	17.60	0.06	19.86	LOAO	I
58204.28	17.65	0.06	20.05	LOAO	R
58204.47	18.10	0.19	19.64	DOAO	V
58208.29	17.81	0.11	19.09	MCD30INCH	R
58210.40	17.88	0.10	19.42	LOAO	R
58212.21	17.91	0.03	20.92	LOAO	R
58212.21	19.67	0.13	20.65	LOAO	B

Table 3.2 (cont'd)

MJD	MAG	ERROR	UL5	OBS	FILTER
58212.25	18.41	0.07	20.65	LOAO	V
58212.25	19.74	0.20	20.38	LOAO	B
58212.26	17.80	0.04	20.49	LOAO	I
58212.26	18.02	0.04	20.82	LOAO	R
58212.79	19.86	0.10	22.81	MAO_SNUCAM	B
58212.79	18.01	0.01	21.85	MAO_SNUCAM	R
58213.19	17.94	0.04	21.19	LOAO	R
58213.56	18.00	0.04	20.22	LSGT	r
58213.57	18.10	0.08	19.92	LSGT	i
58214.55	19.46	0.15	20.59	LSGT	g
58214.56	18.07	0.04	20.32	LSGT	r
58214.56	18.17	0.08	19.93	LSGT	i
58215.56	18.01	0.05	20.29	LSGT	r
58215.57	18.10	0.09	19.80	LSGT	i
58216.25	17.98	0.06	22.39	MCD30INCH	R
58216.27	18.65	0.13	20.10	MCD30INCH	V
58216.55	19.39	0.13	20.81	LSGT	g
58216.56	18.02	0.04	20.46	LSGT	r
58216.57	18.21	0.09	19.97	LSGT	i
58217.20	18.07	0.06	20.40	MCD30INCH	R
58217.22	18.52	0.11	20.08	MCD30INCH	V
58217.56	18.13	0.04	20.70	LSGT	r
58217.56	18.31	0.10	20.29	LSGT	i
58218.14	19.64	0.12	21.00	LOAO	B
58218.14	18.49	0.06	20.92	LOAO	V
58218.15	18.09	0.04	20.96	LOAO	R
58218.15	18.13	0.06	20.56	LOAO	R
58218.54	18.18	0.04	20.65	LSGT	r
58218.55	18.24	0.09	20.17	LSGT	i
58219.14	19.73	0.15	20.72	LOAO	B
58219.14	18.10	0.05	20.50	LOAO	R
58219.14	18.61	0.08	20.50	LOAO	V
58219.30	18.18	0.07	20.30	MCD30INCH	R
58219.54	18.24	0.04	20.72	LSGT	r

Table 3.2 (cont'd)

MJD	MAG	ERROR	UL5	OBS	FILTER
58219.55	18.15	0.03	22.29	DOAO	R
58219.55	19.80	0.11	22.10	DOAO	B
58219.55	18.58	0.05	22.12	DOAO	V
58219.55	18.30	0.08	20.23	LSGT	i
58220.22	19.65	0.12	20.80	LOAO	B
58220.23	18.59	0.07	21.07	LOAO	V
58220.23	18.18	0.04	21.02	LOAO	R
58220.24	18.22	0.05	20.48	LOAO	I
58220.54	19.46	0.10	21.17	LSGT	g
58220.55	18.25	0.04	20.79	LSGT	r
58220.55	18.24	0.07	20.31	LSGT	i
58221.29	19.73	0.19	20.85	LOAO	B
58221.30	18.25	0.08	20.42	LOAO	R
58222.12	18.70	0.09	20.65	LOAO	V
58222.13	18.22	0.07	20.31	LOAO	R
58222.61	19.46	0.12	21.09	LSGT	g
58223.13	18.22	0.04	20.91	LOAO	R
58223.17	18.66	0.14	19.00	CCA250	V
58223.55	19.38	0.11	21.26	LSGT	g
58223.55	18.38	0.04	20.78	LSGT	r
58223.56	18.46	0.10	20.19	LSGT	i
58224.26	18.70	0.17	18.97	CCA250	V
58224.30	18.28	0.05	20.96	LOAO	R
58224.30	19.80	0.15	20.68	LOAO	B
58224.54	19.40	0.10	21.12	LSGT	g
58224.55	18.35	0.04	20.88	LSGT	r
58224.56	18.43	0.11	20.40	LSGT	i
58225.62	18.29	0.04	21.70	DOAO	R
58226.12	18.70	0.10	20.47	LOAO	V
58226.13	18.31	0.05	20.83	LOAO	R
58226.65	18.30	0.04	22.04	DOAO	R
58227.12	18.74	0.10	20.42	LOAO	V
58227.13	18.25	0.04	20.98	LOAO	R
58227.62	18.34	0.04	21.92	DOAO	R

Table 3.2 (cont'd)

MJD	MAG	ERROR	UL5	OBS	FILTER
58228.13	18.37	0.07	20.33	LOAO	I
58228.13	18.43	0.06	20.79	LOAO	R
58228.27	18.28	0.15	19.66	MCD30INCH	B
58228.28	18.65	0.18	18.82	CCA250	V
58228.54	19.57	0.12	21.09	LSGT	g
58228.54	18.37	0.04	20.93	LSGT	r
58228.55	18.81	0.12	20.44	LSGT	i
58228.63	18.39	0.04	21.79	DOAO	R
58229.54	19.60	0.12	21.10	LSGT	g
58229.54	18.52	0.05	20.70	LSGT	r
58229.55	18.66	0.11	20.28	LSGT	i
58229.69	18.47	0.02	22.23	MAO_SNUCAM	R
58229.69	20.08	0.18	23.06	MAO_SNUCAM	B
58230.54	19.86	0.18	20.84	LSGT	g
58230.54	18.56	0.07	20.40	LSGT	r
58232.17	18.83	0.19	19.08	CCA250	V
58232.18	18.41	0.14	19.53	MCD30INCH	R
58235.68	18.65	0.03	20.86	MAO_SNUCAM	R
58237.30	18.78	0.17	19.89	LOAO	R
58242.53	18.78	0.20	20.06	LSGT	r
58243.52	18.78	0.10	20.35	LSGT	r
58244.52	19.02	0.16	20.74	LSGT	r
58245.53	19.77	0.15	21.18	LSGT	g
58245.54	19.05	0.08	20.67	LSGT	r
58245.54	18.96	0.16	20.14	LSGT	i
58247.51	19.81	0.17	20.96	LSGT	g
58247.52	19.18	0.08	20.52	LSGT	r
58247.52	19.21	0.17	19.93	LSGT	i
58248.24	19.00	0.14	20.56	MCD30INCH	R
58248.51	19.76	0.14	21.10	LSGT	g
58250.26	19.14	0.13	20.52	MCD30INCH	R
58253.27	19.91	0.19	20.72	LOAO	B
58254.15	19.28	0.12	20.93	LOAO	V
58254.15	19.06	0.08	21.09	LOAO	R

Table 3.2 (cont'd)

MJD	MAG	ERROR	UL5	OBS	FILTER
58254.50	19.34	0.11	20.56	LSGT	r
58255.14	19.14	0.08	20.94	LOAO	R
58255.50	19.96	0.18	20.98	LSGT	g
58255.50	19.29	0.12	20.58	LSGT	r
58256.14	19.24	0.15	20.28	LOAO	V
58256.14	19.08	0.08	20.79	LOAO	R
58257.15	19.23	0.08	20.76	LOAO	R
58257.51	19.43	0.16	20.56	LSGT	r
58259.14	19.25	0.15	20.24	LOAO	V
58259.15	19.34	0.12	20.58	LOAO	R
58270.15	19.42	0.17	20.87	LOAO	R
58271.21	19.50	0.17	20.46	LOAO	V
58272.23	19.53	0.18	20.74	LOAO	R
58272.23	19.54	0.18	20.53	LOAO	V
58273.19	19.62	0.15	20.72	LOAO	R
58275.21	19.59	0.19	20.66	LOAO	V
58276.16	19.58	0.18	20.71	LOAO	V
58279.18	19.41	0.16	20.66	LOAO	V
58281.16	19.60	0.15	20.57	LOAO	R
58283.42	19.51	0.15	20.70	LSGT	r

Note. — All magnitudes are presented in AB mag system. UL5 column shows 5 σ upper limit magnitude.

Chapter 4

Photometric analysis of two normal Type Ic SNe, SN 2017ein and SN 2017gax

4.1 Introduction

Type Ib/c supernovae (SNe Ib/c) are core-collapse supernovae (CCSNe) from the explosion of massive stars lacking hydrogen lines and ionized silicon lines in their spectra (Smartt 2009). These spectral features suggest that the progenitor stars of SN Ib/c are massive stars of a significant mass loss history (Eldridge et al. 2013; Maund 2018). In particular, SNe Ic show no helium feature on its spectra, and they are categorized into so called, stripped envelope supernovae (SESNe), and massive evolved Wolf-Rayet (WR) stars or He stars have been believed as the origin of them (see Yoon 2015 for recent review). Debates on the progenitor star of SN Ib/c have been settling down toward the progenitor star system being a low mass binary system in close interaction rather than a single massive star based on several arguments (Yoon 2015, 2017; Prentice et al. 2016) . Examination of deep pre-explosion images has found no progenitor stars with optical magnitudes brighter than -4 to -5 mag (Smith et al. 2011; Eldridge et al. 2013). The relative fraction of SNe Ib/c among CCSNe should be much lower than the

observed value of 25 % if single, massive WR stars ($M \gtrsim 25\,M_{\odot}$) are the SNe Ib/c progenitors (Smith et al. 2011), and the observed relative ratios can be reproduced well if relatively low mass binary systems ($M \lesssim 20\,M_{\odot}$) are the progenitors (Podsiadlowski et al. 1992; De Donder & Vanbeveren 1998; Yoon et al. 2010). The ejecta masses are found to be low at 1 – 4 $M_{\odot}$ (e.g., Ensman & Woosley 1988; Shigeyama et al. 1990; Dessart et al. 2011; Drout et al. 2011; Bianco et al. 2014), which is in line with a low mass binary origin (Yoon et al. 2015).

From observational point of view, recent studies report pieces of evidence that SN Ic progenitor stars are compact objects evolved from binary systems (iPTF13bvn; Cao et al. 2013; Fremling et al. 2014; Eldridge et al. 2015; Kim et al. 2015, PTF10vgv; Corsi et al. 2012, SN 2020oi; Gagliano et al. 2021). Direct progenitor detection will be the best solution for unveiling the progenitor star of SN Ib/c. For SN II, a handful of studies present detections of progenitors in pre-explosion image such as deep *HST* imaging data (Smartt 2009, 2015; Van Dyk 2017). For SNe Ib, the progenitor of iPTF13bvn has been identified (Cao et al. 2013; Folatelli et al. 2016), and the progenitor property is consistent with the low mass binary origin for SNe Ib (Bersten et al. 2014; Eldridge et al. 2015; Kim et al. 2015; Fremling et al. 2016; McClelland & Eldridge 2016; Hirai 2017; Yoon et al. 2017; see also Yoon et al. 2012). Likewise, for SNe Ic, currently the progenitor star of only one event, SN 2017ein, has been claimed to be detected in *HST* pre-explosion images (Van Dyk et al. 2018; Kilpatrick et al. 2018; Xiang et al. 2019). In these works, a bright, blue, point-like source has been discovered at the position of SN 2017ein, in the archived WFPC2 HST image of NGC 3938. The source has been suggested as a progenitor candidate, either a single massive star, or a binary star where its companion star, either O-type or B-type, dominates the brightness. If the former is true, the initial mass of the progenitor is $\sim 50\,M_{\odot}$. If it is a binary system, the initial mass of source would be 60 – 80 $M_{\odot}$. However, it still needs to be confirmed from post-explosion images if the identified blue source is the real progenitor of SN 2017ein. Another way to investigate the progenitor system is the analysis of the early phase light curve. SNe release most of their luminosities mainly from radioactive decay of Ni to Co

elements (Branch & Wheeler 2017). However, it is known that very early light curves of SNe can be dominated by the shock-cooling emission, and thus the early time data have been shown to contain useful information of progenitor system (Rabinak & Waxman 2011; Piro & Nakar 2013, 2014; Sapir & Waxman 2017; Piro et al. 2021). The very early light curve of SNe is characterized with the shock break out (SBO) and shock-heated cooling emission. As the shock travels through the stellar envelope, it heats up the materials in the envelope until it reaches to the optical depth that is comparable to the ratio of the light speed and the sound velocity . Then, photons travel away and the shock dies, creating a short flash of light in UV/X-ray called SBO (Piro & Nakar 2013). The duration of SBO is in general too short, so its detection is challenging. But following the SBO, the heated materials radiate away energy, which can be observed as the shock-heated cooling emission. The shock-heated cooling emission can last hours to days (Refs in IMSNG), and peaks at UV to optical. More importantly, the strength of it scales with the radius of the progenitor star, making it possible to infer the stellar radius before the explosion.

Yet another way of exploring the progenitor star property is to examine early color curve of SNe Ib/Ic. He I lines are formed from non-thermal process, and sensitive to Ni mixing. SN Ic might have helium effectively hidden by weak Ni mixing (Dessart et al. 2012). Yoon et al. (2019) suggested that early time color can be a diagnostic for Ni mixing in SN Ib/c. Also, they showed that strong mixing can make monotonic reddening color curve in SN Ic, weak Ni mixing can make non-monotonic color evolution for SN Ib. Once we constrain the Ni mixing, this can teach us if the specific SN Ic had He. So far, very little work exist that constrain the progenitor star properties of SNe Ic through their light curve. In a recent work, it has been suggested that SN 2017ein, a SN Ic, has a bump in the early light curve (Xiang et al. 2019). This was interpreted as the shock-heated cooling emission in its early light curve that suggests the progenitor star radius of $R \simeq 8 \pm 4 R_{\odot}$. The color curve was also examined in Xiang et al. (2019), where they showed that the color curve has a possible early peak which is more consistent with no or little Ni-mixing.

Intensive Monitoring Survey of Nearby Galaxy (IMSNG) is a high cadence (< 8 hrs), intensive monitoring survey of nearby galaxies with high probability of hosting SNe (Im et al. 2019). Since 2014, IMSNG has been carried out using a global network of 1-m class telescopes, to catch the early light curves of SNe and constrain their progenitor star properties. In 2017, two SNe Ic appeared in the IMSNG galaxies, namely SN 2017ein in NGC 3938 and SN 2017gax in NGC 1672, allowing us to study their progenitor stars though their early light and color curves. Here we present our analysis of the light and color curves of these two SNe Ic, from which we provide constraints on progenitor systems. All magnitude in this paper are presented in the AB system.

4.2 Observation and Photometry Analysis

IMSNG has been performing daily monitoring of 60 of galaxies at < 50 Mpc with expected high supernova rate using small telescopes around the world, covering both northern and southern hemisphere. These targets were chosen to have bright NUV flux which can be an indicator for the current star formation rate. The targets are limited to be at < 50 Mpc, so that the shock-heated emission from a $R \sim 1\,R_{\odot}$ star can be detected at a distance of 50 Mpc with a 1-m telescope. The monitoring observations are carried out either in a single R or r band, or a combination of g & r or B & R depending on the telescope. For more information on IMSNG, see Im et al. (2019).

4.2.1 SN 2017ein

SN 2017ein was discovered in the galaxy NGC 3938 by Ron Arbour (Arbour 2017) on 2017 May 25.99 at the position of R.A. = 11h52m53.25s, Dec=+44d07m26.2s (J2000), in the outskirt of the spiral arm of NGC 3938. NGC 3938 is classified as face-on SA(s)c galaxy, at the distance of 17 Mpc (or the distance modulus of $\mu = 31.17$; Tully 2009) and the redshift of $z = 0.002699$ (Wolfinger et al. 2013). We note that 4 SNe appeared historically in NGC 3938 (SN 1961U; SN II, SN 1964L; SN Ic, SN 2005ay; SN II) (Van Dyk et al. 2018).

After the discovery, its progenitor star candidate in the HST archive image was reported

by Van Dyk et al. (2017). Arbour (2017) reported its spectroscopic classification as SN Ic. NGC 3938 has been regularly observed by IMSNG since 2017 April. As a part of IMSNG, we were able to gather an extensive amount of photometric data using various IMSNG telescopes such as the AZT-22 1.5 m telescope at the Maidanak Astronomical Observatory (hereafter, Maidanak) in Uzbekistan (Im et al. 2010; Ehgamberdiev 2018), the Mt. Lemmon 1 m telescope (hereafter, LOAO) in US (Han et al. 2005; Lee et al. 2010), the 0.8 m telescope (hereafter, 30INCH), and the Wide-field IFU Telescope (hereafter, WIT; Im et al. 2021; Hwang et al. 2021), at the McDonald Observatory in US, the Mt. Sobaek 0.6 m telescope (hereafter, SOAO) and the 1 m telescope of Deokheung Optical Astronomy Observatory (hereafter, DOAO, Im et al. 2021) in Korea. Typical exposure times ranged from 3 min (Maidanak) to 9 min (LSGT), and the seeing values also varied depending on the weather and the telescope. The Maidanak data provide B, R color data from early time, and we observed SN 2017ein with other multi-bands after the discovery report. The observed data were reduced for bias, dark, and flat-field. The data obtained at a nearly the same epoch (e.g., three consecutive 3 min frames) are stacked to create a deeper image after WCS registration. As described below, we adopted the image template subtraction method utilizing *Hotpants* (Becker 2015). The reference images were subtracted from the observed image after convolving it with a point-spread-function (PSF) constructed from the observed image to match the seeing of the observed image. The process is reversed if the observed image has a seeing value better than the reference image. Here, the reference images were created from images taken several months before the SN discovery or about one year after. Only the images under the best seeing and other observing conditions are used for the reference image construction. This process yields a difference image. Observing logs are given in Table 4.3 and 4.4, along with the light curve data for each filter. Photometric calibration is conducted by adopting stars near the target (typically $\sim$5 arcminutes from the target) as photometric reference stars. The photometry of these reference stars is taken from the public Pan-STARRS 1 (PS1) catalog (Chambers et al. 2017). We transformed the PS1 *gri* magnitudes to BVR magnitudes following Tonry et al.

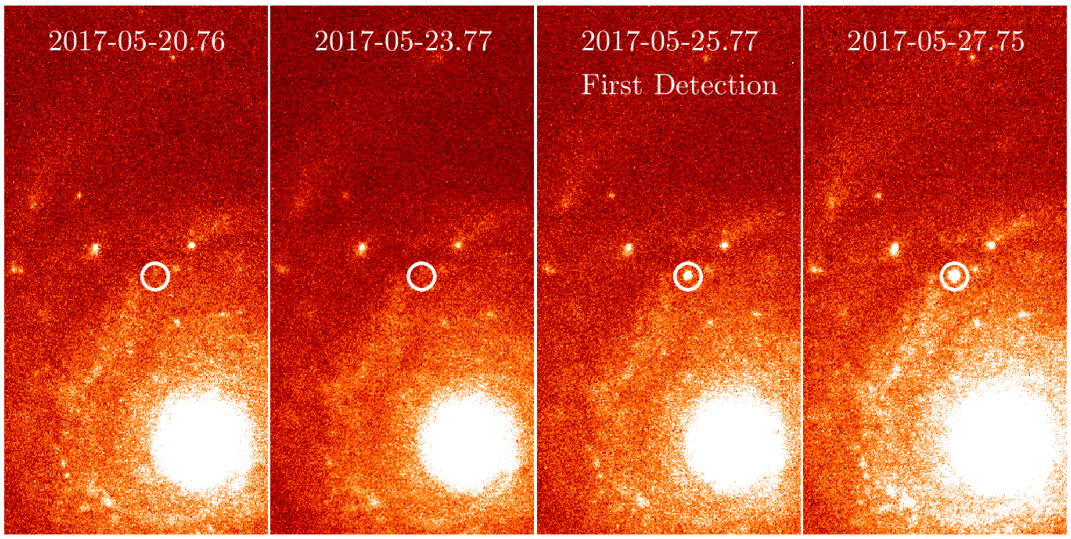

Figure 4.1. The Maidanak images are shown in R-band.

(2012). Our photometry of SN 2017ein agrees with the photometry of Van Dyk et al. (2018) and Kilpatrick et al. (2018) within ~ 0.05 mag.

In our data, on May 24.66 with DOAO, SN 2017ein was not detected, but on May 25.77 at Maidanak data its appearance was clearly recorded in B, R images. This is ahead by 5.3 hrs of the Arbour's discovery (Im et al. 2017). The first detection magnitudes are $B = 18.22$ and $R = 17.89$ mags. Figure 4.1 illustrates the emergence of SN 2017ein in IMSNG observation. After the SN discovery, SN 2017ein had been monitored intensively in $BVRI$ bands with the IMSNG telescopes. There is a gap in the observation for 90 days in the late time light curve because the Moon was too close to NGC 3938 at that period.

4.2.2 SN 2017gax

SN 2017gax was discovered by Valenti et al. (2017) at NGC 1672 on 2017-08-14 17:05:16 (UT). Its coordinate is RA = 04:45:49.430 and DEC = -59:14:42.56 (J2000), and the SN is located in the west side of the bar region of host galaxy. Jha (2017) classified SN 2017gax as a SN Ic spectroscopically. NGC 1672 has no historical supernovae, and is classified as a barred spiral galaxy ($z = 0.0044$) at the distance of 11.70 Mpc (Bottinelli

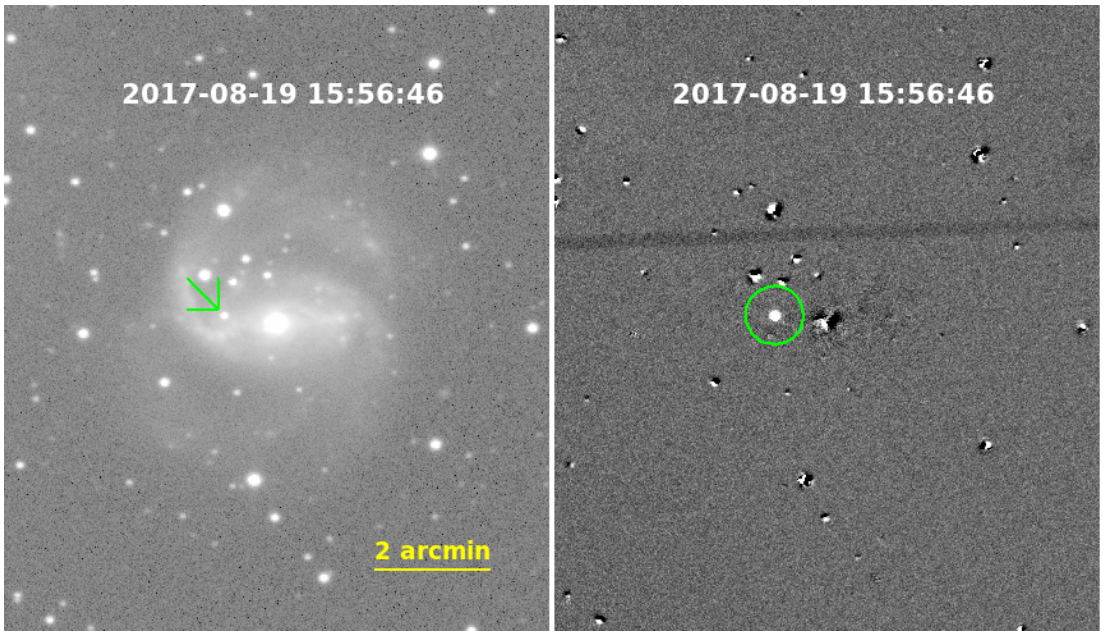

Figure 4.2. SN 2017gax discovery. Non-detection and detection images from LSGT observations.

et al. 1984). Since 2015, we have been monitoring NGC 1672 with the Lee Sang Gak Telescope (LSGT; Im et al. 2015) as a part of IMSNG. LSGT is a robotically operated 0.43 m telescope, equipped with a deep depletion chip CCD camera, SNUCAM-II (Choi & Im 2017). Our last non-detection was on 2017-08-10T18:23:07 (UT) in r-band. The first light recorded in our data was on 2017-08-13T03:58:28 in r band which is ahead of the discovery time by 0.96 day. Figure 4.2 shows the position of SN 2017gax in the images before and after the subtraction.

At each epoch, we obtained 3-5 images per filter with 3 min per frame. These images were stacked to a combined image per filter. The IMSNG monitoring was done in r-band every night, and multi-band g, i images have been taken twice a week before the discovery. The $griz$-band monitoring has been conducted since the discovery. All the images were calibrated using standard IRAF pacakages for bias, dark and flat correction. The pre-processed images were registered based on WCS with the astrometry.net software (Lang et al. 2010). The registered images were stacked for each epoch by SWarp (Bertin

2010). For the image subtraction, we followed the same procedures as SN 2017ein. We performed an aperture photometry on the SN and photometry calibration stars, taking an optimal aperture diameter of a double of the seeing size. Photometry calibration is done using the same method as we adopted for SN 2017ein, except for using the catalog data from the SkyMapper DR2 (Onken et al. 2019). When necessary, we transformed the SkyMapper gri mags to BVR mags, using Tonry et al. (2012).

4.2.3 Extinction correction

We used the Milky Way color excess values of $E(B-V) = 0.019$ and $E(B-V) = 0.021$ for SN 2017ein and SN 2017gax (Schlafly & Finkbeiner 2011). For SN 2017ein, we adopt the host galaxy color excess value of $E(B-V) = 0.34$ and $R_V = 2.6$ (Kilpatrick et al. 2018). For SN 2017gax, we estimated $E(B-V)$ from the intrinsic color of SN Ic (Drout et al. 2011; Lyman et al. 2016). Drout et al. (2011) showed that SNe Ic have $V-R = 0.24$ at +10 days after V_{max}. Our measurements on that epoch was $(g-r) = 0.5$. Converting $g-r$ to $V-R$, we deduced $E(V-R) = 0.26 \pm 0.15$ and $A_V = 1.04$ for NGC 1672 taking $R_V = 3.1$ assuming Cardelli et al. (1989) extinction law.

4.3 Results

4.3.1 Light Curves

The multi-band light curves of SN 2017ein and SN 2017gax are given in Figures 4.3 and 4.4. These light curves are similar to SN 2013ge as mentioned in Xiang et al. (2019), and their light curve analysis results are given below.

The measurement of light curve parameters was done with a polynomial fitting of n=7 degree, which provides the peak luminosity, the peak epoch, Δm_{15}. The derived parameters are given in Table 4.1 and 4.2. For SN 2017ein, the B band peak date and magnitudes are 57910.663 ± 0.140 and 15.801 ± 0.012. The V band peak date and magnitude are 57912.333 ± 0.376 and 14.036 ± 1.508. The R band peak date and

magnitude are 57914.176 ± 0.093 and 14.949 ± 0.030. For SN 2017gax, the g band peak date and magnitudes are 57993.693 ± 0.098 and 13.926 ± 0.105. The r band peak date and magnitude are 57996.925 ± 0.049 and 13.812 ± 0.001. The i band peak date and magnitude are 57997.473 ± 0.100 and 13.880 ± 0.001. Note that SN 2017ein was not observable around V_{max} time due to a bad weather, and this makes a larger uncertainty in the derived values than SN 2017gax. The two SNe are found to have the peak absolute magnitudes of M_V = -18.3 M_g = -17.54 after the extinction correction. These values are in the range of typical SN Ic (-17 to -19; Drout et al. 2011; Bianco et al. 2014). The light curve widths Δm_{15} also agree with normal SNe Ic distribution that ranges from 0.6 to 1.2. The explosion times are estimated by a single power law fit to the light curve and the analysis of the early light curve, and it will be described in detail later. The rise times t_{rise} from explosion to V and g band peak (SN 2017ein; 57912.333, SN 2017gax; 57993.693) are 15.37 ± 0.42 days and 15.31 ± 0.51 days.
The R(or r)-band light curves of the two SNe agree very well when shifted to match each other as shown on Figure 4.5. SN 2017ein declines slightly faster than SN 2017gax. About 60 days after the peak luminosity, the light curve slopes change, showing γ-ray escape. SN 2017ein's late time slope is steeper than SN 2017gax, meaning more efficient γ-ray escape which seem related to the low ejecta mass M_{ej}.

4.3.2 Bolometeric Light Curves

We constructed bolometric light curves of the two SNe applying the prescription of Lyman et al. (2014). They provide the bolometric correction fit parameters for SE SNe on Table 2 in their paper, which are reproduced in the equations 4.1 and 4.2. The peak bolometric luminosities are found to be 1.05 × 10^{42} $erg^{-1}s^{-1}$ and 2.1 × 10^{42} $erg^{-1}s^{-1}$ for each, which are consistent with typical peak bolometric luminosities of SNe Ic (Prentice et al. 2016).

$$BC_B = -0.029 - 0.302 \times (B-R) - 0.224 \times (B-R)^2, \quad rms = 0.069 \tag{4.1}$$

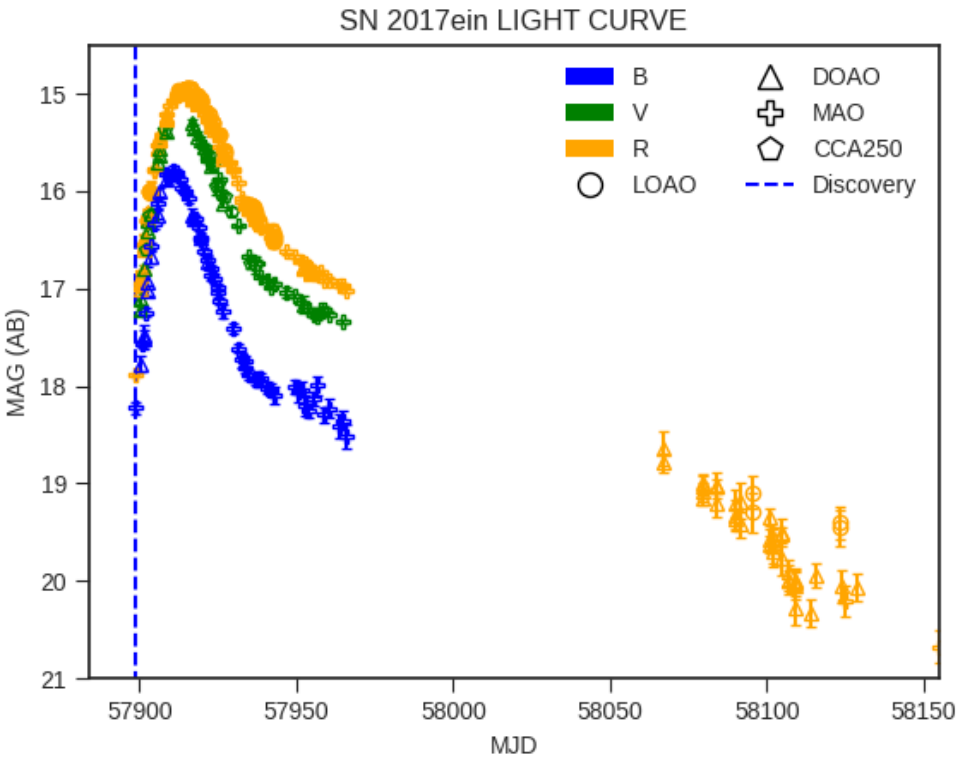

Figure 4.3. Multi-band light curves of SN 2017ein

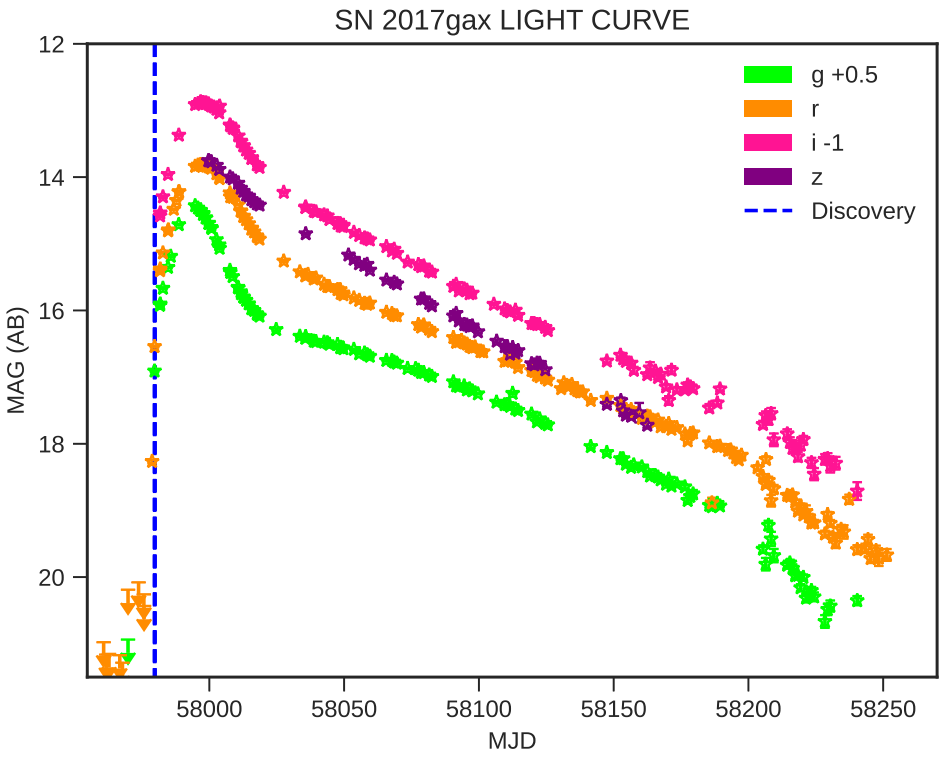

Figure 4.4. Multi-band light curves of SN 2017gax. The vertical dashed line indicates the epoch of the discovery, and the 3-σ upper limits are marked with the downward arrows.

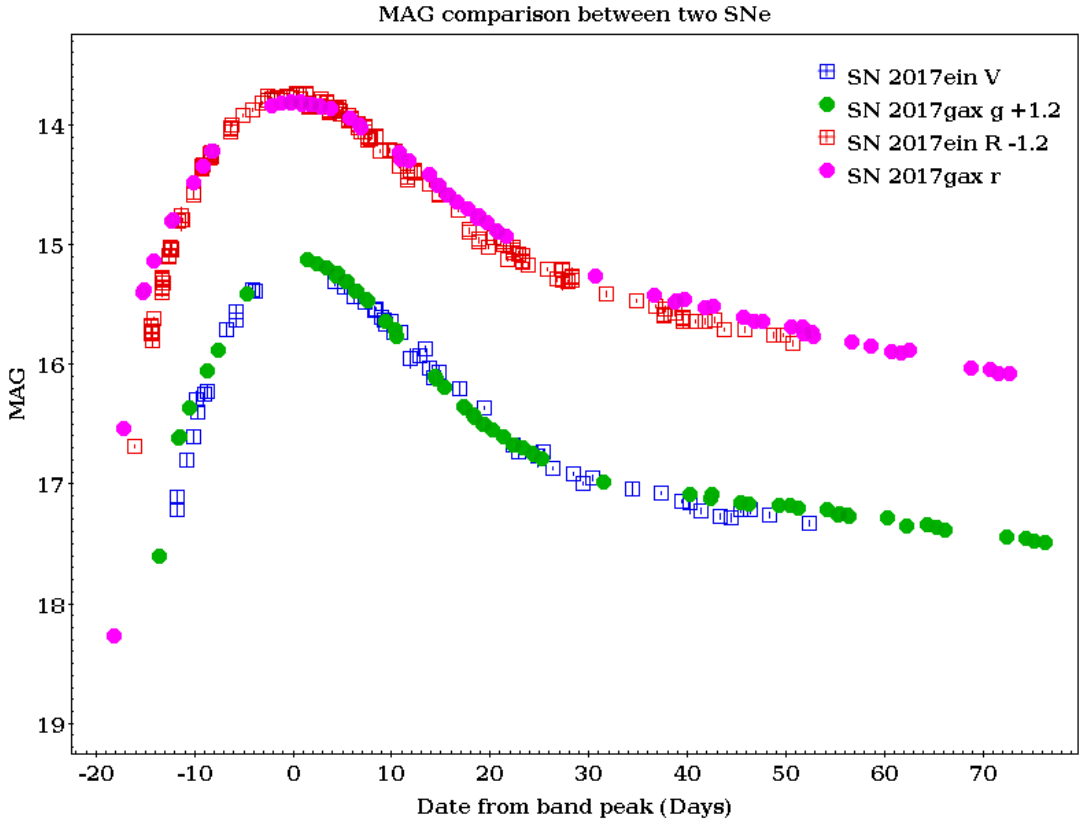

Figure 4.5. Matching light curves of SN 2017ein VR band and SN 2017gax gr band. SN 2017gax data points of V band are shifted in the date and the peak magnitudes to the SN 2017ein g band light curves. SN 2017ein data points of R band are shifted in the date and the peak magnitudes to the SN 2017gax r band light curves. The time of zero is chosen to be the epoch of the light curve peak. SN 2017gax has little broader light curves than SN 2017ein.

Table 4.1. Physical Parameters and values estimated from analysis of SN 2017ein.

Parameter	Value	Error	Unit	Note
DM(μ)	31.17	0.10	Mag	Tully et al. 2009
$T_{B.Max}$	57910.663	0.140	MJD	Polyfit
B_{Max}	15.801	0.012	Mag	Polyfit
$\Delta m_{15}, B$	1.348	0.022	Mag	Polyfit
$T_{V.Max}$	57912.333	0.376	MJD	Polyfit
V_{Max}	14.036	1.508	Mag	Polyfit
$\Delta m_{15}, V$	1.108	0.007	Mag	Polyfit
$T_{R.Max}$	57914.176	0.093	MJD	Polyfit
R_{Max}	14.949	0.030	Mag	Polyfit
$\Delta m_{15}, R$	0.823	0.009	Mag	Polyfit
E(B-V)	0.34	0.07	Mag	Kilpatrick et al. 2019
R_V	2.6	0.134		Kilpatrick et al. 2019
t_0	57896.887	0.204	MJD	power law fit
α	1.14	0.08		power law fit, R-band
t_{rise}	15.37	0.42	Day	power law fit
M_{Ni}	0.085	0.08	$M_\odot$	Bolometic LC
M_{ej}	2.03	0.32	$M_\odot$	Bolometic LC
E_k	1.056	0.2	10^{51} ergs	Bolometic LC

Table 4.2. Physical Parameters and values estimated from analysis of SN 2017gax

Parameter	Value	Error	Unit	Note
DM(μ)	30.35		Mag	NED mean
$T_{g.Max}$	57993.693	0.098	MJD	Polyfit
g_{Max}	13.926	0.105	Mag	Polyfit
$\Delta m_{15}, g$	1.027	0.005	Mag	Polyfit
$T_{r.Max}$	57996.925	0.049	MJD	Polyfit
r_{Max}	13.812	0.001	Mag	Polyfit
$\Delta m_{15}, r$	0.716	0.004	Mag	Polyfit
$T_{i.Max}$	57997.473	0.100	MJD	Polyfit
i_{Max}	13.880	0.001	Mag	Polyfit
$\Delta m_{15}, i$	0.632	0.007	Mag	Polyfit
E(g-r)	0.26	0.15	Mag	Drout et al. 2011
R_V	3.1			cardelli et al. 1989
t_0	57978.55	0.015	MJD	power law fit
α	0.94	0.014		power law fit
t_{rise}	15.31	0.51	Day	power law fit
M_{Ni}	0.04	0.07	$M_\odot$	Bolometic LC
M_{ej}	2.53	0.046	$M_\odot$	Bolometic LC
E_k	1.5	0.6	10^{51} ergs	Bolometic LC

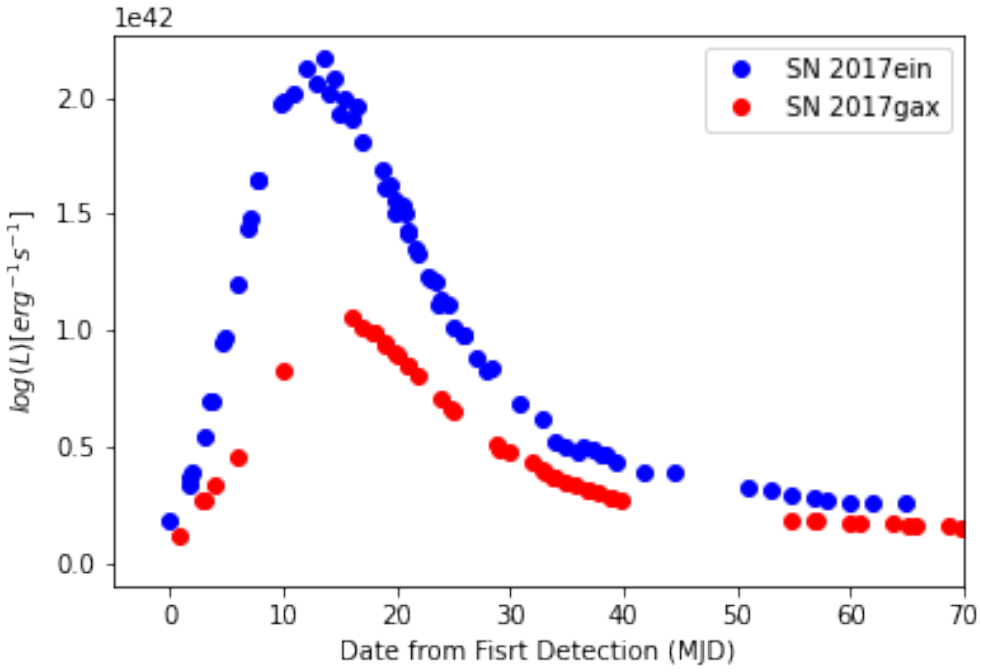

Figure 4.6. Bolometric light curve of SN 2017ein and SN 2017gax.

$$BC_g = 0.054 - 0.195 \times (g-r) - 0.719 \times (g-r)^2, \quad rms = 0.076 \tag{4.2}$$

We estimated physical parameters such as the Ni mass, M_{Ni}, the ejecta mass, M_{ej} and the kinetic energy, E_k of the explosion and the progenitor properties. Based on the relations of Prentice et al. (2016), we obtain M_{Ni} = 0.085 and 0.04 $M_\odot$, M_{ej} = 2.03 and 2.53 $M_\odot$ and E_k = 1.05 and 1.50 × 10^{51} erg for SN 2017ein and SN 2017gax, respectively. Our parameter values for SN 2017ein agree with the values in Xiang et al. (2019). From the ejecta mass, it seems that these SNe are from low-mass binary progenitor systems, because a single massive star progenitor would have a final mass lower limit of $> 5\ M_\odot$ (Yoon 2015). The peak bolometric luminosity of SN 2017ein is about twice larger than SN 2017gax, although the ejecta mass and the kinetic energy of SN 2017gax are larger than SN 2017ein. This suggests that the Ni mass takes a bigger role in energy radiation for SN 2017ein than SN 2017gax via radioactive decay.

4.3.3 Early Light Curve and Constraints on Progenitor Star Size

As mentioned earlier, the early light curve of SNe can be used to constrain the progenitor star size through the analysis of the early SHE component. Below we discuss this issue for both supernovae.

4.3.4 SN 2017ein

SN 2017ein has been claimed to show SHE component in the early epoch data, which gives the progenitor star size of $R = 8 \pm 4R_{\odot}$ (Xiang et al. 2019). We re-visit this suggestion by utilizing the IMSNG data and the data published in Xiang et al. (2019). Our data coverage of the early SN emission has an advantage of near simultaneous B and R-band coverage with the first epoch lagging only about 0.4 day to the first ATLAS data which was taken with a clear filter that covers a very wide wavelength range. Therefore, our data enable us to examine the early evolution of the light curve in detail free from uncertainties governing the shape of the SN SED in early phase. Figure 4.7 and 4.8 show the B and R band early light curves of SN 2017ein. These data are fitted with a single power law function of $L \propto t^{\alpha}$. The fitting is done in several ways. First, we used all the data from the first detection till MJD = 58907 days (roughly the first 10 days). Another fitting was performed by excluding the first detection data from the fit, assuming that the first detection data are affected by SHE. We performed the fitting using a fixed $\alpha = 2$ and also setting the α value free. After the power-law fit, we examined if the first detection data can be explained by SHE models.

Figure 4.7 shows the fitting results for the B-band light curve. B-band best-fit result gives best fit of α=1.14 (case 2). when excluding the first detection point, and $\alpha = 4.29$ when including the first detection point (case 1). Also, a fixed power law function with $\alpha = 2$ can reproduce the detection points. However, Both fits that includes the first detection points fail to reconcile the last non-detection point, suggesting that another component is necessary.

The R-band light curve was fitted in a similar way. The best fit result of $\alpha = 1.46$ single power law explains all data points. Figure 4.8 shows the fitting results for the

R-band light curve. The first light time of R-band fit is two days ahead of B-band best fit result. We set the explosion time of SN 2017ein of MJD=57896.886.
To find a possible SHE feature in early light curve and place a constraint on the progenitor star radius, we overplot the Rabinak & Waxman (2011) model model (hereafter, RW model) SHE light curves as was done in SN 2015F (Im et al. 2015b). We find that the first data points in $B-$ and $R-$bands can be explained well with SHE model of a progenitor radius of $R \sim 1 - 2\,R_{\odot}$, but a SHE model with $R \sim 8\,R_{\odot}$ gives SHE too strong to explain the data. In particular, the excess emission is evident in B-band data. Therefore, we conclude that the early light curve of SN 2017ein suggests a progenitor with a raidus of $1 - 2\,R_{\odot}$.

4.3.5 SN 2017gax

Figure 4.9 shows the case of SN 2017gax. Blue line is single power law fit of $\alpha = 0.94$, dotted and dashed lines are same as above. Setting $\alpha = 2$, the line of fit overshoot the upper limit before the first light time. So we chose $\alpha = 0.94$ fit here. The explosion time is 4.5 hours before the first light time. The Best constraint is the lines of 3 $R_{\odot}$ closest to data point. However there is a gap between the last non-detection limit and the first detection during $\sim$ 2.5 days. We plotted 0.5 $R_{\odot}$ model lines starting from MJD $\sim$ 57976 in case of possible SHE. Normally, a SN Ic progenitor star with not much helium left, it is expected to be very compact. Whether detection limit or detected magnitude, if we have data point in time gap, it could give more stringent condition. Some of SNe Ic are known to have compact progenitor stars. The SN Ib iPTF13bvn progenitor star is reported as compact as a few solar radius (Cao et al. 2013). Xiang et al. (2019) suggested SN 2017ein stellar envelope size limit is lower than $8 \pm 4\ R_{\odot}$. The PTF10vgv is also one of compact WR star progenitor SN Ic, it has similar physical properties SN 2017ein, SN 2017gax and SN 2007gr (Corsi et al. 2012). In summary, SN 2017ein and SN 2017gax look like to have compact WR star progenitor systems of low mass binary stars. Based on the theoretical study, initial masses of SNe Ic progenitor stars in low mass binary progenitor systems of these SNe may be $10 < M_{ZAMS} < 20$

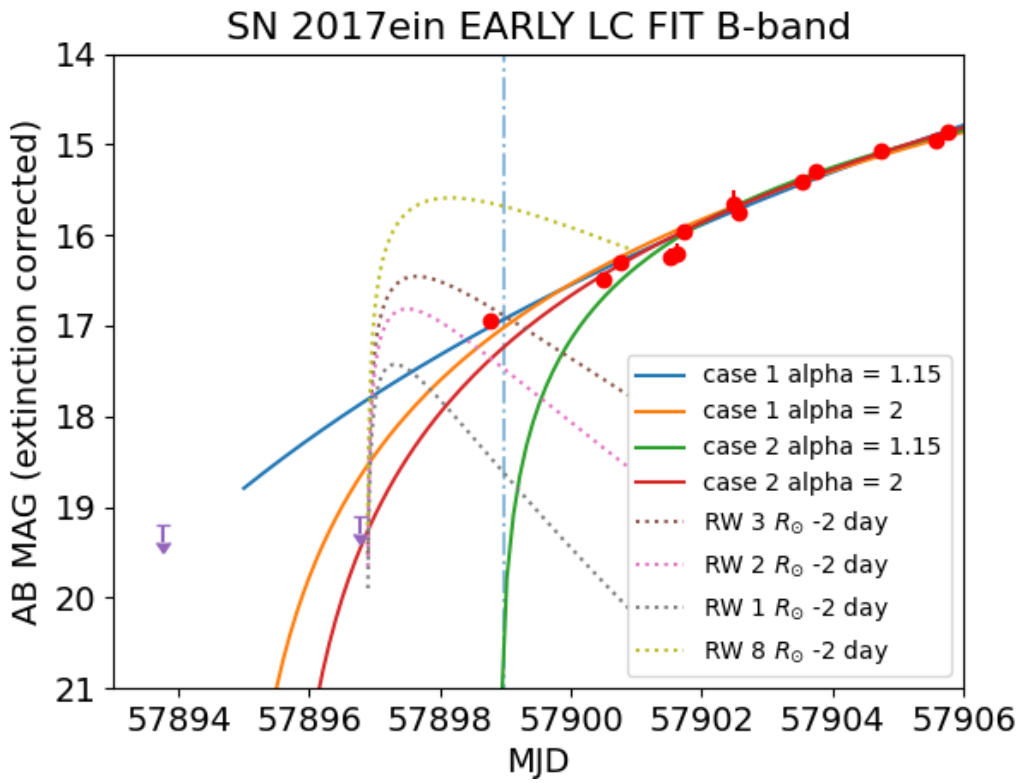

Figure 4.7. SN 2017ein B-band early light curve fitting.

$M_\odot$ (Yoon 2017).

4.3.6 Color Evolution

Color evolution of two SNe are shown in Figure 4.10, 4.11 with V-band peak as vertical line. $B-V$ of SN 2017ein and $g-r$ SN 2017gax colors show interesting features. Near the first detection, it proceed from red to blue and turns to be red again before V-band maximum. That shapes look like the expected weak/moderate Ni mixing color evolution of Yoon et al. (2019). But early plateau or SBO feature predicted by Yoon et al. (2019) was not found in our data, possibly due to lack of earlier data very close to explosion time. We drew a comparison with models of Yoon et al. (2019) in Figure 4.12. $V-R$ curve of SN 2017ein follows CO core model of 3.93 $R_\odot$ + 1.0 foe E_K + 0.5 f_m Ni mixing degree well. SN 2017ein $V-R$ and SN 2017gax $g-r$ color curves

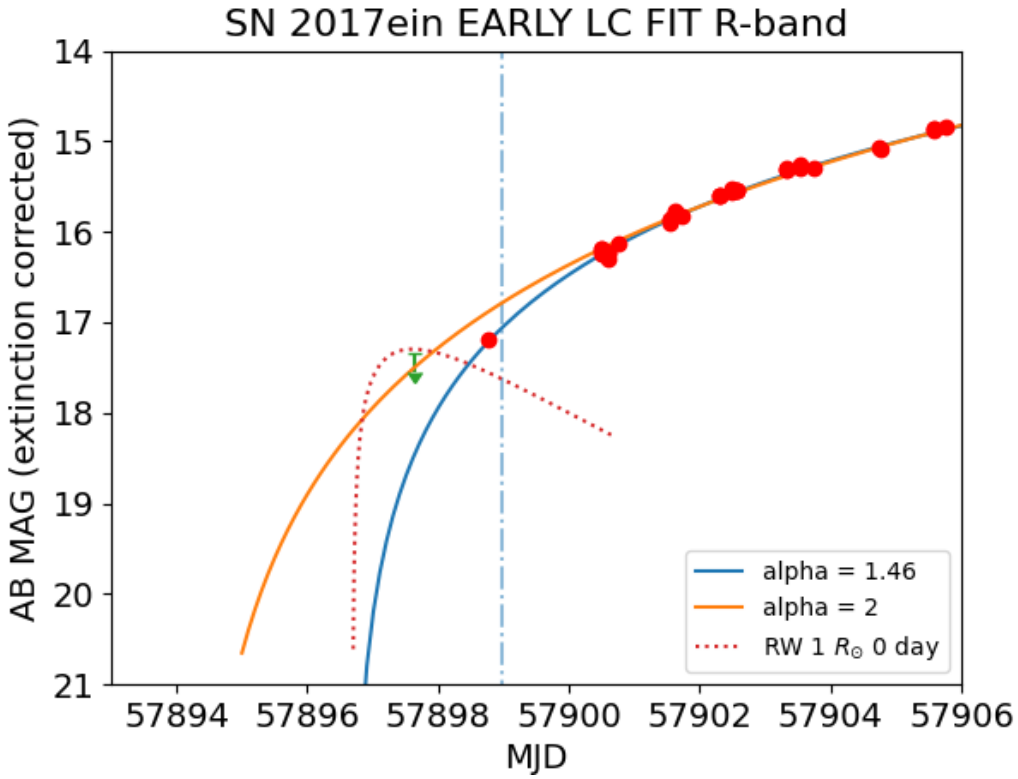

Figure 4.8. SN 2017ein *R*-band early light curve fitting.

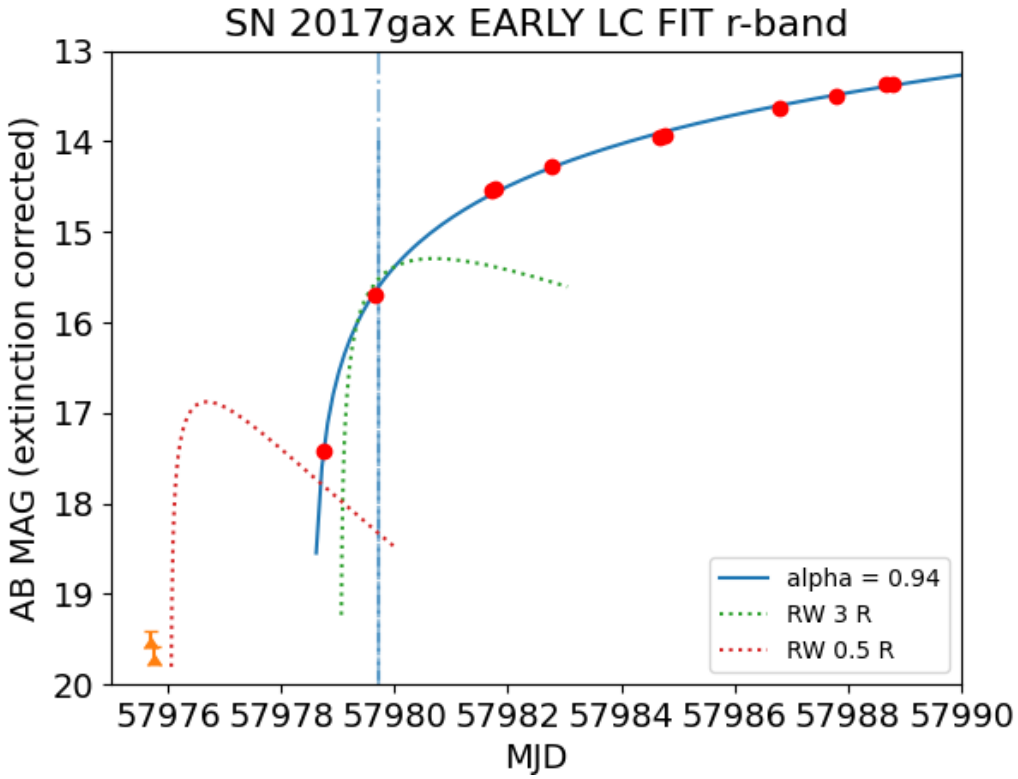

Figure 4.9. SN 2017gax r-band early light curve data fitting.

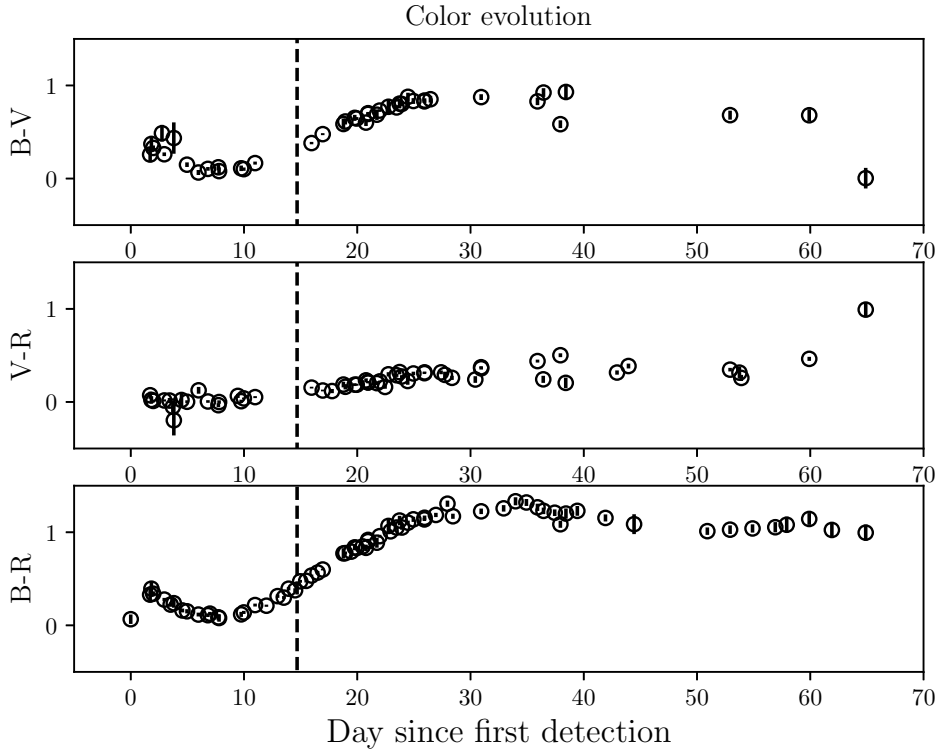

Figure 4.10. Color curve of SN 2017ein

appear to track the model line of CO core configuration very much. Strongly Ni mixing makes SN Ic color increase monotonically to red direction. Weak/moderate Ni-mixed SN Ib shows initial blue-to-red increasing first, red-to-blue decreasing later, and then increasing red direction again after $\sim$ 10 days from explosion. Our two SNe look like the SN Ib color evolution shapes though they are SN Ic. It is hard to attain the information on the helium content form two SNe. But with weak/moderate Ni Mixing, We can not decide that there are no helium on both SN 2017ein and SN 2017gax at all.

4.4 Discussion

SN 2017ein and SN 2017gax turned out to be very similar in photometric aspect, those are SN 2007gr like normal SN Ic supernovae. But SN 2017ein light curve declined a

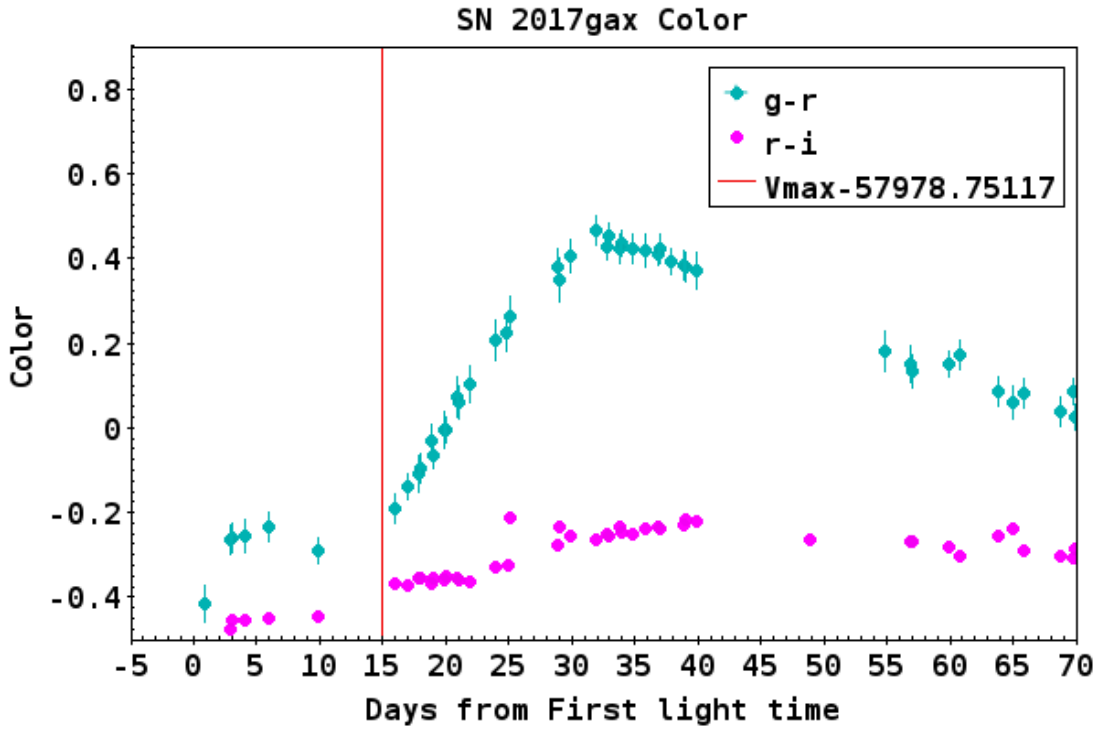

Figure 4.11. Color curve of SN 2017gax

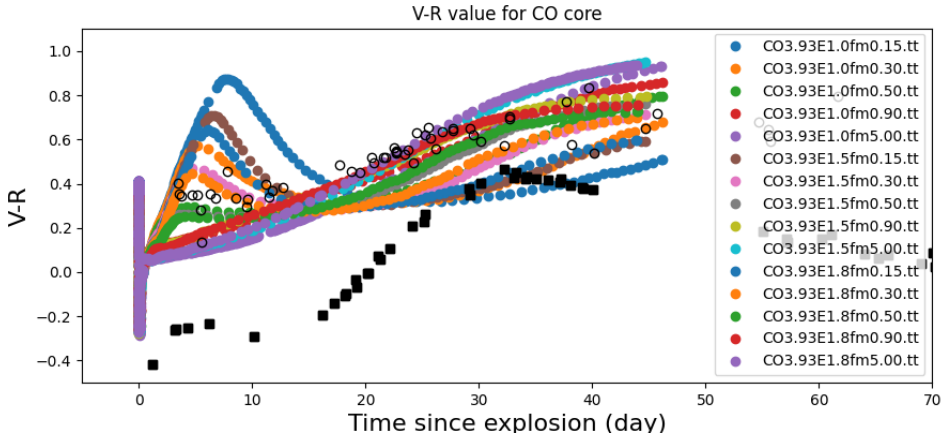

Figure 4.12. Color curve fitting to the model of Yoon et al. (2019)

little faster, differences between them are physical properties such as ejecta mass, kinetic energy and nickel mass. Ni mass difference makes luminosity gap in absolute luminosity and bolometric luminosity. The studies on SN 2017ein predicted that the progenitor system could be very massive initial mass 60-80 $M_{\odot}$ based on stellar evolution model and possible detection of progenitor from pre-explosion HST image (Van Dyk et al. 2018; Kilpatrick et al. 2018). Teffs et al. (2020) suggested that SN 2017ein progenitor system might be relatively low mass binary of 16-20 $M_{\odot}$. Our results also support low mass binary progenitor scenario of type Ic SNe. From similarity of light curves among SN 2017ein, SN 2017gax and SN 2007gr, low mass binary progenitor system is favored to three SNe.

Xiang et al. (2019) claimed that they found shock cooling emission. They used shock cooling + Ni decay model to fit early excess. But our simple single power law fitting and model comparison could not find early excess like that. Because they have 0.4 days earlier data from $ATLAS$ than us close to explosion time. As mentioned above, SN 2017ein and SN 2007gr shows strong Carbon lines revealing that they were compact CO core at final stage of evolution. Therefore, We may conclude that the progenitor stars of SN 2017gax is also compact WR stars exploding as CO core. To confirm the progenitor systems, direct detection of companion star or remnant will be useful at explosion site with deep imaging in future.

We need to keep it in mind that the photometric analysis is very sensitive to large host galaxy extinction value and distance measurement. Stritzinger et al. (2018) suggested that the favored SN Ic host galaxy extinction parameter R_V is 4.3 rather than 3.1. In that case, size constraint will be much larger up to tens of solar radius. Van Dyk et al. (2018) argued that A_V of NGC 3938 can be varied from 1.0 to 1.9. For SN 2017gax, more precise estimate of host galaxy extinction via Na ID EW measure can lead to more precise values. Also distance measurement can make lot of change in size and physical parameters. The literature values from NED varies with standard deviation of 0.1-0.3. This difference can make significant change in our result. Still the progenitor systems of two SNe are likely to be compact CO core evolve from WC star.

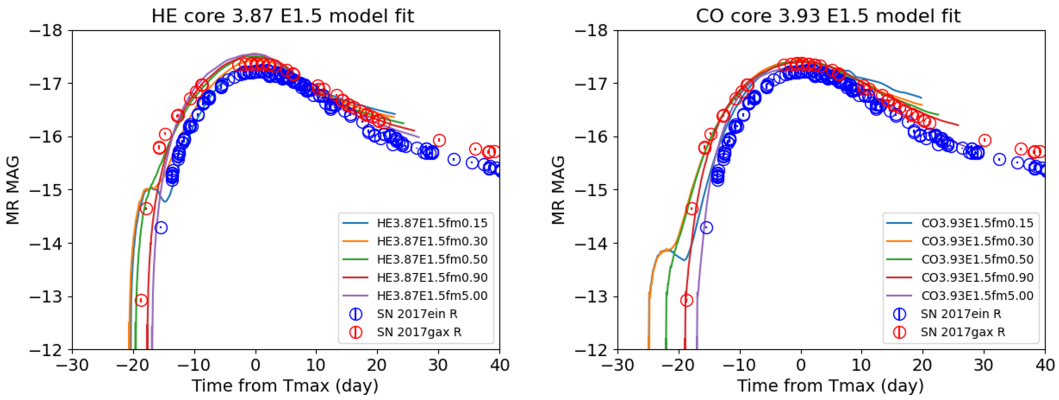

Figure 4.13. *R*-band absolute magnitude comparison to numerical model of Yoon et al. (2019)

Intriguingly, comparison with numerical model data from Yoon et al. (2019) gave us more details on nickel mixing degree and E_k of both SNe. Yoon et al. (2019) provides absolute magnitudes of $BVRI$ band and radius information along time from explosion moment of SN Ib/c progenitor. HE core 3.87 $M_\odot$ and CO core 3.93 $M_\odot$ of three kinds of E_k = 1.0, 1,5 and 1.8 foe set to take Ni mixing degree of 5 steps (fm = 0.15, 0.3; weak, 0.5, 0.9; moderate, 5.0; strong). The expected radius values of all models rise steeply from explosion moment, so that comparison with them to our data is not available. HE core model is closer to our data than CO core model on the whole. Figure 4.13 displays model M_R versus our data of two core models. We compared BVR band absolute magnitude to model prediction. B-band shows 1 mag offset, R-band matched closely with fixing T_{max} date. In magnitude comparison, when E_k of SN 2017ein is 1.5 or 1.8, matched better, that is different from E_k = 1.056 of bolometric luminosity. Mostly fm of SN 2017ein tends to show weak mixing degree (0.15, 0.3), however, in CO core model strong (fm = 5.0) value is favored. SN 2017gax shows moderate Ni mixing degree of fm = 0.5 and 0.9 for all cases. Color evolution in two core models also support that fm of SN 2017ein is weak and fm of SN 2017gax is moderate.

SN 2017ein and SN 2017gax can be explained with an explosion of C/O star with a low

level of nickel mixing and certain degree of He envelope like SN 2007gr (Mazzali et al. 2010). The final mass of two SNe will be in the range 2-7 $M_{\odot}$, taking into account of the result of Woosley et al. (2021). With these range of final mass, single massive WR star model hardly able to reproduce observed features. The stellar evolution model like BPASS (Eldridge et al. 2017) of low mass binary provides more natural explanation. About color evolution, note that $g-$ and $r-$ bands are not completely same. But their central wavelength locate close. The color evolution suggests weak/moderate Ni mixing. No or weak Ni mixing has been suggested as a way to hide He feature in the SN Ic spectrum. SN 2017ein has no or weak Ni mixing. Despite that, we find a compact star size, meaning that He atmosphere must have been minimal or non-existent. This supports the idea that SNe Ic progenitors are in general systems with naked CO core generally. But we can rule out possible hidden He content in these SNe owing to Ni Mixing degree.

4.5 Conclusion

We present optical photometry of two normal SE sNe SN 2017ein and SN 2017gax including early light curve analysis, bolometric light curve and color evolution. SN 2017ein and SN 2017gax light curves are similar to SN 2007gr light curve. Besides physical parameters of them are close to those of SN 2007gr, which means that those are normal type Ic SNe. The size of progenitor system can be limited lower than a few $R_{\odot}$ from early time light curve. So the progenitor systems of two SNe may be compact CO core stars evolved from relatively low mass binary system ($M_{ZAMS} \sim 10 - 20 M_{\odot}$ and final mass $M_f \sim 2 - 6 M_{\odot}$). The color curves of them show that they have suffered from weak/moderate Ni mixing, demonstrating Ib like behavior on color. Thus, the progenitor system might be naked CO core. But there may remain small amount of hidden helium content.

Table 4.3. SN 2017ein photometry

MJD	MAG	ERROR	UL5	OBS	FILTER
57896.76			> 21.70	MAO_FLI	B
57896.76			> 22.14	MAO_FLI	R
57897.62			> 19.27	DOAO	R
57898.76	18.22	0.05	21.64	MAO_FLI	B
57898.77	17.89	0.01	22.11	MAO_FLI	R
57900.48	17.77	0.08	20.48	DOAO	B
57900.48	17.11	0.04	20.73	DOAO	V
57900.48	16.94	0.04	20.37	DOAO	R
57900.49	16.87	0.04	20.26	DOAO	R
57900.59	17.21	0.05	20.01	DOAO	V
57900.59	17.00	0.04	20.22	DOAO	R
57900.60	16.91	0.04	20.21	DOAO	R
57900.75	17.56	0.03	21.98	MAO_FLI	B
57900.75	16.82	0.01	22.37	MAO_FLI	R
57901.52	17.51	0.09	21.23	DOAO	B
57901.53	16.79	0.04	20.20	DOAO	V
57901.53	16.56	0.02	20.681	DOAO	R
57901.62	17.47	0.09	20.05	DOAO	B
57901.63	16.47	0.03	20.93	DOAO	R
57901.73	17.24	0.04	22.06	MAO_FLI	B
57901.73	16.52	0.01	22.40	MAO_FLI	R
57902.20	16.60	0.04	20.18	CCA250	V
57902.29	16.29	0.03	21.37	LOAO	R

Table 4.3 (cont'd)

MJD	MAG	ERROR	UL5	OBS	FILTER
57902.30	16.29	0.04	20.80	LOAO	R
57902.48	16.92	0.15	19.40	DOAO	B
57902.49	16.29	0.07	18.50	DOAO	V
57902.49	16.21	0.04	19.45	DOAO	R
57902.57	17.02	0.05	20.10	DOAO	B
57902.57	16.39	0.04	20.45	DOAO	V
57902.57	16.23	0.03	20.79	DOAO	R
57903.26	16.24	0.05	19.03	CCA250	V
57903.33	16.00	0.03	21.25	LOAO	R
57903.54	16.67	0.06	20.02	DOAO	B
57903.54	16.22	0.04	20.21	DOAO	V
57903.54	15.96	0.06	18.90	DOAO	R
57903.73	16.56	0.03	21.89	MAO_FLI	B
57903.74	15.99	0.01	22.36	MAO_FLI	R
57904.74	16.33	0.04	21.75	MAO_FLI	B
57904.74	15.76	0.01	22.08	MAO_FLI	R
57904.76	15.79	0.01	21.33	MAO_FLI	R
57905.58	16.23	0.03	20.94	DOAO	B
57905.58	15.70	0.04	20.40	DOAO	V
57905.58	15.56	0.03	20.22	DOAO	R
57905.59	15.55	0.02	20.28	DOAO	R
57905.76	16.12	0.04	21.87	MAO_FLI	B
57905.76	15.53	0.01	22.37	MAO_FLI	R

Table 4.3 (cont'd)

MJD	MAG	ERROR	UL5	OBS	FILTER
57906.50	16.00	0.04	20.00	DOAO	B
57906.51	15.55	0.04	20.11	DOAO	V
57906.51	15.45	0.03	19.98	DOAO	R
57906.57	15.62	0.05	18.96	DOAO	V
57906.57	15.45	0.02	20.12	DOAO	R
57908.23	15.37	0.04	19.28	CCA250	V
57908.52	15.87	0.04	20.07	DOAO	B
57908.52	15.38	0.04	20.38	DOAO	V
57908.52	15.23	0.03	20.54	DOAO	R
57908.75	15.81	0.03	21.70	MAO_FLI	B
57908.75	15.20	0.01	21.86	MAO_FLI	R
57909.74	15.84	0.04	21.83	MAO_FLI	B
57909.75	15.11	0.01	22.13	MAO_FLI	R
57910.75	15.78	0.04	21.85	MAO_FLI	B
57910.75	15.07	0.01	22.02	MAO_FLI	R
57911.73	15.80	0.03	21.57	MAO_FLI	B
57911.73	15.01	0.01	22.44	MAO_FLI	R
57912.28	14.99	0.04	20.24	LOAO	R
57912.30	14.99	0.04	20.33	LOAO	R
57912.71	15.88	0.03	21.75	MAO_FLI	B
57912.71	14.98	0.01	22.08	MAO_FLI	R
57913.28	14.97	0.03	20.29	LOAO	R
57913.73	15.96	0.04	21.35	MAO_FLI	B

Table 4.3 (cont'd)

MJD	MAG	ERROR	UL5	OBS	FILTER
57913.73	14.99	0.01	21.76	MAO_FLI	R
57914.26	14.96	0.04	20.69	LOAO	R
57914.73	15.99	0.04	21.76	MAO_FLI	B
57914.73	14.96	0.01	22.15	MAO_FLI	R
57915.27	14.95	0.05	20.81	LOAO	R
57915.72	16.07	0.04	21.84	MAO_FLI	B
57915.72	14.98	0.01	22.30	MAO_FLI	R
57916.25	14.95	0.04	20.44	LOAO	R
57916.54	15.05	0.03	19.54	DOAO	R
57916.55	15.30	0.03	20.25	DOAO	V
57916.55	16.24	0.06	19.69	DOAO	B
57916.55	15.01	0.04	18.62	DOAO	R
57917.54	15.35	0.04	20.17	DOAO	V
57917.55	15.03	0.02	19.87	DOAO	R
57917.55	16.28	0.05	20.22	DOAO	B
57917.71	16.28	0.03	21.80	MAO_FLI	B
57917.71	14.98	0.01	22.30	MAO_FLI	R
57918.24	15.02	0.02	21.24	LOAO	R
57918.55	15.43	0.04	20.43	DOAO	V
57918.55	15.08	0.04	20.18	DOAO	R
57918.71	16.36	0.03	21.91	MAO_FLI	B
57918.72	15.05	0.01	22.35	MAO_FLI	R
57919.25	15.06	0.03	21.46	LOAO	R

Table 4.3 (cont'd)

MJD	MAG	ERROR	UL5	OBS	FILTER
57919.54	16.48	0.05	20.37	DOAO	B
57919.54	15.47	0.04	20.32	DOAO	V
57919.54	15.07	0.02	20.22	DOAO	R
57919.71	15.08	0.01	22.09	MAO_FLI	R
57919.71	16.48	0.04	21.76	MAO_FLI	B
57919.72	15.10	0.01	21.93	MAO_FLI	R
57919.73	16.49	0.04	21.63	MAO_FLI	B
57919.73	15.10	0.01	22.04	MAO_FLI	R
57920.50	15.54	0.03	19.84	DOAO	V
57920.50	15.15	0.03	20.17	DOAO	R
57920.51	15.16	0.03	19.20	DOAO	R
57920.74	15.54	0.01	21.89	MAO_FLI	V
57920.74	16.61	0.03	22.12	MAO_FLI	B
57920.74	15.15	0.01	22.36	MAO_FLI	R
57920.76	15.14	0.01	21.99	MAO_FLI	R
57921.22	15.61	0.05	19.25	CCA250	V
57921.52	16.71	0.06	19.28	DOAO	B
57921.52	15.63	0.04	19.67	DOAO	V
57921.52	15.18	0.03	19.70	DOAO	R
57921.52	15.20	0.03	19.66	DOAO	R
57921.71	16.69	0.02	22.19	MAO_FLI	B
57921.71	15.66	0.01	22.16	MAO_FLI	V
57921.71	15.26	0.00	22.58	MAO_FLI	R

Table 4.3 (cont'd)

MJD	MAG	ERROR	UL5	OBS	FILTER
57922.24	15.25	0.05	20.61	LOAO	R
57922.25	15.63	0.04	19.92	CCA250	V
57922.51	15.73	0.03	20.34	DOAO	V
57922.51	15.32	0.03	20.08	DOAO	R
57922.69	16.85	0.04	21.75	MAO_FLI	B
57922.71	16.79	0.04	22.23	MAO_FLI	B
57922.71	15.32	0.01	22.72	MAO_FLI	R
57923.22	15.73	0.05	19.11	CCA250	V
57923.25	15.29	0.03	21.06	LOAO	R
57923.72	16.89	0.04	22.10	MAO_FLI	B
57923.73	15.41	0.01	22.48	MAO_FLI	R
57924.23	15.95	0.07	17.43	CCA250	V
57924.70	16.99	0.03	21.95	MAO_FLI	B
57924.70	15.42	0.01	22.42	MAO_FLI	R
57924.71	17.04	0.04	21.18	MAO_FLI	B
57924.71	15.40	0.01	22.05	MAO_FLI	R
57925.21	15.92	0.04	19.17	CCA250	V
57925.23	15.41	0.04	19.55	LOAO	R
57925.71	17.12	0.03	22.23	MAO_FLI	B
57925.71	15.87	0.01	22.13	MAO_FLI	V
57925.71	15.54	0.01	22.66	MAO_FLI	R
57926.17	16.03	0.04	19.43	CCA250	V
57926.51	16.11	0.03	20.02	DOAO	V

Table 4.3 (cont'd)

MJD	MAG	ERROR	UL5	OBS	FILTER
57926.51	15.63	0.02	20.21	DOAO	R
57926.73	17.23	0.06	21.01	MAO_FLI	B
57926.73	15.58	0.02	21.53	MAO_FLI	R
57927.13	16.06	0.04	19.86	CCA250	V
57927.22	15.59	0.03	21.16	LOAO	R
57928.73	15.69	0.01	22.30	MAO_FLI	R
57929.19	16.20	0.04	19.90	CCA250	V
57929.70	15.79	0.01	21.99	MAO_FLI	R
57929.71	17.41	0.05	21.58	MAO_FLI	B
57929.71	15.77	0.01	21.79	MAO_FLI	R
57931.69	17.61	0.04	22.16	MAO_FLI	B
57931.69	16.36	0.01	21.97	MAO_FLI	V
57931.70	15.91	0.01	22.47	MAO_FLI	R
57932.74	16.10	0.01	21.95	MAO_FLI	R
57932.74	17.72	0.07	21.70	MAO_FLI	B
57932.75	16.07	0.01	22.14	MAO_FLI	R
57933.69	17.74	0.05	21.59	MAO_FLI	B
57933.70	16.17	0.01	21.99	MAO_FLI	R
57933.70	17.81	0.05	21.65	MAO_FLI	B
57933.71	16.15	0.01	22.05	MAO_FLI	R
57934.68	17.88	0.05	20.76	MAO_FLI	B
57934.68	16.67	0.02	21.51	MAO_FLI	V
57934.69	16.22	0.01	21.84	MAO_FLI	R

Table 4.3 (cont'd)

MJD	MAG	ERROR	UL5	OBS	FILTER
57935.19	16.73	0.05	19.45	CCA250	V
57935.22	16.13	0.03	21.10	LOAO	R
57936.21	16.17	0.03	20.98	LOAO	R
57936.70	17.94	0.04	21.32	MAO_FLI	B
57936.71	16.32	0.01	22.26	MAO_FLI	R
57937.18	16.76	0.08	17.83	CCA250	V
57937.20	16.24	0.06	20.54	LOAO	R
57937.70	17.92	0.07	21.35	MAO_FLI	B
57937.71	16.73	0.02	21.02	MAO_FLI	V
57937.71	16.28	0.02	21.48	MAO_FLI	R
57938.21	16.33	0.05	20.80	LOAO	R
57938.72	17.92	0.05	21.39	MAO_FLI	B
57938.72	16.87	0.01	21.36	MAO_FLI	V
57938.72	16.37	0.01	21.75	MAO_FLI	R
57940.68	18.02	0.06	21.30	MAO_FLI	B
57940.69	16.92	0.01	21.18	MAO_FLI	V
57940.69	16.40	0.01	21.75	MAO_FLI	R
57941.70	18.03	0.06	21.39	MAO_FLI	B
57941.70	16.99	0.01	21.31	MAO_FLI	V
57941.71	16.48	0.01	21.81	MAO_FLI	R
57942.21	16.41	0.06	20.09	LOAO	R
57942.71	18.09	0.09	21.16	MAO_FLI	B
57942.72	16.95	0.02	21.07	MAO_FLI	V

Table 4.3 (cont'd)

MJD	MAG	ERROR	UL5	OBS	FILTER
57942.72	16.50	0.01	21.56	MAO_FLI	R
57943.21	16.46	0.05	20.04	LOAO	R
57946.71	17.03	0.05	20.46	MAO_FLI	V
57946.72	16.61	0.02	21.03	MAO_FLI	R
57949.68	18.00	0.06	21.43	MAO_FLI	B
57949.68	17.07	0.01	21.29	MAO_FLI	V
57949.68	16.67	0.01	21.97	MAO_FLI	R
57950.69	18.06	0.09	21.51	MAO_FLI	B
57951.69	18.03	0.07	21.47	MAO_FLI	B
57951.69	17.14	0.01	21.52	MAO_FLI	V
57951.69	16.71	0.01	21.89	MAO_FLI	R
57952.51	17.15	0.09	19.60	DOAO	V
57952.52	16.79	0.04	20.20	DOAO	R
57952.68	18.19	0.10	21.41	MAO_FLI	B
57952.68	16.73	0.02	21.82	MAO_FLI	R
57953.67	18.25	0.07	21.38	MAO_FLI	B
57953.67	17.22	0.01	21.41	MAO_FLI	V
57953.67	16.77	0.01	21.86	MAO_FLI	R
57954.50	16.84	0.04	20.14	DOAO	R
57955.68	18.12	0.07	21.39	MAO_FLI	B
57955.68	17.27	0.01	21.44	MAO_FLI	V
57955.68	16.84	0.01	21.92	MAO_FLI	R
57956.68	17.99	0.09	21.35	MAO_FLI	B

Table 4.3 (cont'd)

MJD	MAG	ERROR	UL5	OBS	FILTER
57956.69	17.28	0.02	21.49	MAO_FLI	V
57956.69	16.84	0.02	21.93	MAO_FLI	R
57957.67	17.21	0.02	20.63	MAO_FLI	V
57957.67	16.83	0.02	21.77	MAO_FLI	R
57958.67	18.29	0.07	21.33	MAO_FLI	B
57958.68	17.21	0.03	21.30	MAO_FLI	V
57958.68	16.91	0.01	21.86	MAO_FLI	R
57960.67	18.22	0.09	21.26	MAO_FLI	B
57960.68	17.25	0.02	21.35	MAO_FLI	V
57960.68	16.90	0.02	21.79	MAO_FLI	R
57963.66	18.41	0.12	21.10	MAO_FLI	B
57963.67	16.96	0.02	21.60	MAO_FLI	R
57964.66	18.35	0.09	21.21	MAO_FLI	B
57964.66	17.33	0.02	21.24	MAO_FLI	V
57964.66	16.96	0.01	21.78	MAO_FLI	R
57965.66	18.51	0.12	21.11	MAO_FLI	B
57965.66	17.02	0.02	21.68	MAO_FLI	R
58066.82	18.78	0.10	20.58	DOAO	R
58079.84	19.14	0.06	22.38	DOAO	R
58083.87	19.02	0.07	22.01	DOAO	R
58089.85	19.36	0.09	21.75	DOAO	R
58091.83	19.41	0.13	21.52	DOAO	R
58095.44	19.08	0.17	20.94	LOAO	R

Table 4.3 (cont'd)

MJD	MAG	ERROR	UL5	OBS	FILTER
58100.79	19.62	0.08	22.27	DOAO	R
58101.89	19.54	0.09	21.81	DOAO	R
58104.88	19.52	0.08	21.84	DOAO	R
58106.78	19.99	0.10	22.35	DOAO	R
58108.87	19.99	0.09	22.43	DOAO	R
58113.85	20.32	0.14	22.42	DOAO	R
58115.85	19.93	0.12	22.17	DOAO	R
58123.47	19.45	0.19	20.85	LOAO	R
58123.87	20.04	0.16	21.40	DOAO	R
58124.88	20.19	0.15	21.58	MAO_FLI	R
58128.71	20.06	0.14	22.31	DOAO	R
58154.95	20.67	0.16	21.76	MAO_FLI	R

Table 4.4. SN 2017gax photometry

MJD	g	g err	r	r err	i	i err	z	z err
57969.83	>20.67		>20.03					
57973.74			>20.07					
57975.71			>20.25					
57975.77			>20.43					
57978.75			18.26	0.04				
57978.75			18.26	0.04				
57979.67	16.41	0.03	16.54	0.03				
57981.70	15.42	0.03	15.4	0.02	15.58	0.03		
57981.77	15.4	0.03	15.38	0.02	15.54	0.03		
57982.78	15.17	0.03	15.14	0.02	15.29	0.03		
57984.66	14.85	0.02	14.80	0.03	14.96	0.03		
57984.78			14.79	0.02				
57986.78			14.48	0.02				
57987.79			14.35	0.02				
57988.67	14.21	0.02	14.22	0.02	14.37	0.03		
57988.78			14.22	0.03				
57994.72	13.93	0.02	13.84	0.02	13.91	0.03		
57995.77	13.96	0.03	13.82	0.02	13.90	0.03		
57996.64	14.00	0.03	13.82	0.03	13.88	0.03		
57996.77	14.00	0.03	13.81	0.02	13.87	0.03		
57997.64	14.06	0.03	13.81	0.03	13.88	0.03		
57997.77	14.04	0.02	13.83	0.02	13.88	0.03		
57998.64	14.11	0.03	13.83	0.03	13.89	0.03		

Table 4.4 (cont'd)

MJD	g	g err	r	r err	i	i err	z	z err
57998.77	14.11	0.02	13.83	0.02	13.89	0.02		
57999.65	14.19	0.03	13.84	0.03	13.9	0.03	13.75	0.03
57999.77	14.19	0.03	13.85	0.03	13.91	0.04	13.75	0.03
58000.67	14.25	0.03	13.87	0.03	13.93	0.03	13.77	0.04
58002.64	14.44	0.04	13.95	0.03	13.98	0.04	13.82	0.04
58003.64	14.52	0.03	14.01	0.03	14.03	0.03	13.88	0.03
58003.81	14.57	0.03	14.02	0.04	13.93	0.04		
58007.65	14.9	0.03	14.24	0.03	14.22	0.04	14.0	0.04
58007.77	14.93	0.04	14.29	0.04	14.23	0.03		
58008.65	14.99	0.03	14.3	0.03	14.26	0.03	14.03	0.04
58010.74	15.16	0.03	14.41	0.02	14.38	0.04		
58011.60	15.22	0.02	14.51	0.02	14.46	0.03	14.17	0.03
58011.74	15.25	0.02	14.51	0.02	14.47	0.03		
58012.60	15.30	0.03	14.59	0.02	14.53	0.03	14.21	0.03
58012.74	15.30	0.03	14.58	0.02	14.53	0.04		
58013.60	15.35	0.03	14.64	0.02	14.59	0.03	14.27	0.03
58014.60	15.40	0.03	14.70	0.03	14.64	0.02	14.28	0.03
58015.60	15.47	0.02	14.78	0.02	14.72	0.03	14.34	0.03
58015.74	15.47	0.03	14.76	0.02	14.71	0.04		
58016.61	15.5	0.02	14.82	0.02			14.37	0.03
58017.61	15.55	0.03	14.88	0.02	14.81	0.03	14.4	0.04
58017.74	15.56	0.02	14.89	0.03	14.81	0.03		
58018.59	15.58	0.04	14.93	0.02	14.85	0.04	14.42	0.03

Table 4.4 (cont'd)

MJD	g	g err	r	r err	i	i err	z	z err
58027.60			15.26	0.03	15.23	0.03		
58033.58	15.89	0.04	15.42	0.03				
58035.62	15.92	0.03	15.48	0.03	15.46	0.04		
58035.75	15.89	0.03	15.47	0.03	15.45	0.04	14.85	0.03
58036.60			15.46	0.04				
58038.74	15.96	0.02	15.53	0.02	15.51	0.03		
58039.56	15.97	0.02	15.51	0.02	15.52	0.02		
58042.56	15.98	0.03	15.61	0.02	15.57	0.03		
58043.77	15.98	0.03	15.64	0.03	15.58	0.07		
58044.56	16.01	0.03	15.64	0.02	15.64	0.03		
58047.56	16.01	0.03	15.69	0.02	15.69	0.03		
58048.56	16.06	0.02	15.69	0.02	15.70	0.03		
58048.73	16.05	0.02	15.75	0.03	15.73	0.03		
58049.56	16.06	0.03	15.74	0.02	15.74	0.03		
58049.74	16.07	0.02	15.77	0.02	15.72	0.04		
58053.62	16.08	0.02	15.81	0.02	15.83	0.03	15.23	0.04
58055.59	16.15	0.02	15.85	0.02	15.87	0.03	15.3	0.04
58057.59	16.14	0.03	15.89	0.03	15.91	0.03	15.32	0.04
58058.59	16.16	0.03	15.91	0.03	15.93	0.03	15.31	0.05
58059.52	16.19	0.04	15.89	0.03	15.94	0.03	15.39	0.03
58065.68	16.25	0.03	16.03	0.03	16.04	0.03	15.54	0.04
58067.74	16.25	0.03	16.05	0.03	16.11	0.03		
58068.54	16.27	0.03	16.07	0.02	16.08	0.04	15.58	0.03

Table 4.4 (cont'd)

MJD	g	g err	r	r err	i	i err	z	z err
58069.55	16.29	0.02	16.08	0.02	16.14	0.03	15.6	0.04
58077.54	16.40	0.02	16.21	0.02	16.31	0.03		
58078.55	16.43	0.02	16.25	0.02	16.34	0.03	15.83	0.04
58079.55	16.43	0.02	16.22	0.02	16.33	0.04	15.83	0.05
58081.55	16.47	0.02	16.28	0.02	16.41	0.03	15.89	0.03
58082.55	16.49	0.02	16.32	0.02	16.42	0.04	15.93	0.05
58090.54	16.57	0.04	16.41	0.04	16.64	0.04	16.08	0.04
58091.54	16.63	0.04	16.48	0.04	16.61	0.03	16.04	0.04
58092.54	16.64	0.03	16.47	0.03	16.71	0.04	16.16	0.03
58093.56			16.45	0.03				
58094.54	16.63	0.03	16.49	0.02	16.68	0.04	16.21	0.04
58095.55	16.69	0.02	16.50	0.02	16.70	0.03	16.22	0.03
58096.55	16.68	0.02	16.54	0.02	16.75	0.03	16.24	0.04
58097.55	16.71	0.02	16.56	0.03	16.74	0.03	16.23	0.04
58098.60			16.55	0.02				
58100.59			16.62	0.02				
58101.59			16.62	0.03				
58109.55	16.91	0.02	16.76	0.02	16.98	0.04	16.54	0.04
58110.55	16.91	0.02	16.75	0.02	17.00	0.04	16.54	0.05
58111.54	16.94	0.02	16.74	0.03	17.02	0.04	16.66	0.05
58113.53	16.98	0.03	16.78	0.03	17.0	0.05	16.64	0.05
58114.52	17.00	0.03	16.86	0.03	17.07	0.05	16.6	0.04
58119.53	17.05	0.04	16.9	0.04	17.20	0.05	16.8	0.04

Table 4.4 (cont'd)

MJD	g	g err	r	r err	i	i err	z	z err
58120.54			16.92	0.04	17.20	0.05	16.82	0.05
58121.54	17.17	0.04	16.97	0.04	17.21	0.05	16.79	0.05
58122.54	17.13	0.04	16.99	0.03	17.21	0.05	16.79	0.04
58124.57	17.19	0.03	17.01	0.03	17.25	0.05	16.89	0.05
58125.57	17.22	0.03	17.05	0.03	17.30	0.05		
58130.51			17.17	0.04				
58131.51			17.08	0.02				
58132.50			17.12	0.03				
58133.50			17.14	0.03				
58134.50			17.11	0.02				
58135.49			17.18	0.03				
58136.49			17.20	0.02				
58137.49			17.22	0.03				
58138.50			17.22	0.02				
58141.51	17.54	0.05	17.35	0.04				
58147.47	17.63	0.05	17.32	0.04	17.76	0.06	17.41	0.06
58152.53	17.72	0.04	17.43	0.03	17.67	0.06		
58153.53	17.72	0.03	17.45	0.03	17.73	0.06	17.51	0.06
58154.52	17.81	0.03	17.48	0.03	17.76	0.05	17.57	0.06
58156.48	17.85	0.02	17.49	0.03	17.79	0.05	17.59	0.06
58157.47	17.82	0.03	17.53	0.03	17.9	0.1		
58160.47	17.85	0.03	17.62	0.03				
58162.46	17.92	0.02	17.58	0.02	17.96	0.05	17.72	0.07

Table 4.4 (cont'd)

MJD	g	g err	r	r err	i	i err	z	z err
58163.49	17.98	0.03	17.60	0.03	17.86	0.17		
58165.46	17.98	0.03	17.67	0.02	17.91	0.05		
58166.46	18.0	0.03	17.64	0.03	18.01	0.06		
58167.46	18.04	0.03	17.74	0.03	17.96	0.06		
58169.44	18.11	0.03	17.74	0.03	18.15	0.07		
58170.44	18.03	0.05	17.70	0.04	18.35	0.13		
58171.45	18.13	0.04	17.78	0.03	17.90	0.12		
58173.45	18.10	0.04	17.76	0.04	18.19	0.07		
58176.44	18.15	0.05	17.85	0.05	18.19	0.08		
58177.47	18.35	0.08	17.96	0.06	18.12	0.08		
58178.46	18.29	0.09	17.85	0.06	18.15	0.09		
58179.47	18.25	0.12	17.84	0.06	18.17	0.09		
58185.47	18.42	0.06	17.99	0.04	18.46	0.12		
58186.45	18.44	0.06	18.89	0.15				
58188.44	18.39	0.03	18.04	0.03	18.39	0.07		
58189.45	18.43	0.03	18.04	0.03	18.18	0.07		
58192.44			18.10	0.04				
58193.43			18.09	0.03				
58194.42			18.14	0.04				
58195.41			18.21	0.04				
58196.41			18.24	0.04				
58197.41			18.17	0.04				
58203.41			18.36	0.08				

Table 4.4 (cont'd)

MJD	g	g err	r	r err	i	i err	z	z err
58205.40	19.08	0.11	18.49	0.06	18.71	0.11		
58206.42	19.31	0.19	18.61	0.09	18.58	0.12		
58206.52			18.24	0.1				
58207.42	18.72	0.13	18.55	0.11	18.63	0.16		
58208.42	18.93	0.21	18.85	0.17	18.55	0.17		
58209.42	19.18	0.20	18.67	0.11	18.94	0.19		
58214.39	19.32	0.10	18.77	0.08	18.85	0.14		
58215.39	19.29	0.10	18.79	0.08	18.98	0.15		
58216.39	19.37	0.12	18.77	0.08	19.07	0.16		
58217.38	19.48	0.09	18.87	0.07	19.06	0.13		
58218.38	19.47	0.08	19.01	0.07	19.19	0.14		
58219.38	19.66	0.11	18.93	0.07	19.02	0.14		
58220.38	19.50	0.09	19.07	0.07	18.94	0.11		
58221.38	19.82	0.13	19.02	0.18				
58222.40	19.78	0.12	19.09	0.09				
58223.39	19.70	0.11	19.19	0.09	19.28	0.15		
58224.39	19.80	0.13	19.19	0.09	19.46	0.18		
58228.38	20.17	0.19	19.35	0.1	19.23	0.16		
58229.38	19.98	0.17	19.06	0.08	19.22	0.16		
58230.38	19.93	0.17	19.19	0.1	19.33	0.20		
58231.38			19.40	0.13				
58232.37			19.49	0.15	19.29	0.19		
58234.38			19.28	0.13				

Table 4.4 (cont'd)

MJD	g	g err	r	r err	i	i err	z	z err
58235.37			19.32	0.20				
58236.37								
58237.37			18.83	0.14				
58238.37								
58240.37	19.85	0.14	19.59	0.13	19.71	0.27		
58243.36			19.57	0.14				
58244.36			19.44	0.14				
58245.36			19.72	0.13				
58247.35			19.60	0.15				
58248.35			19.72	0.23				
58251.36			19.67	0.18				

Chapter 5

Conclusion

In this thesis, we presented three part of studies. First, we reported establishment of observational systems of IMSNG, especially on SNUCAM-II. By performing the SNe monitoring program, we obtained useful data that caught early time of SNe. Among the SNe caught early in IMSNG, we presented the early light curves analysis of a SN Ia, SN 2018kp, and two SNe Ic, SN 2017ein and SN 2017gak.

In Chapter 2, the characteristics and the performance of the SNUCAM-II system are presented, that is installed on LSGT at the Siding Spring Observatory in Australia. This upgraded system is more powerful than the front-illuminated CCD camera systems that have been in use earlier, with QE of $> 80\%$ from 400–900 nm, factors of a few to tens improvement at short and long wavelengths. SNUCAM-II also boasts 18 filters, *ugriz* and 13 medium band pass filters from 400 nm to 1100 nm having 50 nm band width for the characterization of SEDs of many different kinds of sources. Under the adopted operation parameters, the CCD gain is 1.15 ± 0.03 e^-/ADU, the readout time is 0.9 sec for the 1k $\times$ 1k frame. The readout noise is 6.0 e^-, and the dark current is 0.2 e^-/sec at -70°C. The SNUCAM-II system shows a good linearity (better than 98% at the currently measurable limit) ranging from tens of ADU $\sim$ 60000 ADU. The shutter pattern was also examined, and we find no visible shutter pattern in images even with exposure time as short as 0.1 s. Photometric calibration parameters were derived from the analysis of the data of a standard star and reference stars in the vicinity of NGC

6902, showing that SNUCAM-II on LSGT can reach the magnitude limit of $g = 19.91$ AB mag and z =18.20 AB mag at 5-σ with 180 sec exposure time for point source detection. With its high sensitivity at short and long wavelengths, the availability of many medium-band filters, and the robotic operation capability, SNUCAM-II on LSGT can be used to perform unique scientific projects such as photometric reverberation mapping of AGNs and intensive monitoring of galaxies to catch the early light curve of SNe.

Next, the results of photometric analaysis of optical light curve of SN 2018kp including early phase are described. Data coverage of NGC 3367 with daily cadence provides well sampled optical light curve of SN 2018kp. The explosion time t_0 is 58140.261 from single power law fit, earlier than first light time by 2 days. Long term light curve fitting gives us the distance modulus to NGC 3367 of 33.31 with $H_0 = 70$ km/s/Mpc. Host galaxy extinction $E(B-V)_{host} = 0.608 \pm 0.007$ and its reddening parameter $R_V = 1.721 \pm 0.134$ are derived. The other light curve parameters we computed indicate that SN 2018kp is normal type Ia SN such as Sn 2011fe. Most of all, we set constraint the size of progenitor system upper limit by 4 $R_\odot$. That can rule out giant or supergiant star, but main sequence or subgiant star companion WD may be the companion star of its progenitor. There were potential shock cooling emission feature was shown. We look forward to have more samples catching very early phase close to explosion time to study the appropriate properties of SN Ia progenitor system.

Finally, optical photometry of two normal SE sNe SN 2017ein and SN 2017gax are presented, including early light curve analysis, bolometric light curve and color evolution. SN 2017ein and SN 2017gax light curves are similar to SN 2007gr light curve. Besides physical parameters of them are close to those of SN 2007gr, which means that those are normal type Ic SNe. The size of progenitor system can be limited lower than a few $R_\odot$ from early time light curve. So the progenitor systems of two SNe may be compact CO core stars evolved from low mass binary system ($M_{ZAMS} \sim 10 - 20 M_\odot$ and final mass $M_f \sim 2 - 6 M_\odot$). The color curves of them show that they have suffered from weak/moderate Ni mixing, demonstrating Ib like behavior on color. Thus, the

progenitor system might be naked CO core. But there may remain small amount of hidden Helium content.

IMSNG project is proven to be very effective for transient study as shown by our SNe progenitor research. Target-selected and high-cadence monitoring with well-programmed observation, using small telescope network enable us to catch the emergency of SNe. The early time light curves, though they are a small set of photometric data points, lead us to look deeper and closer into the progenitor star of SNe. From 2014 to 2018, 14 SNe have been discovered in IMSNG target galaxies. More and better extended and elaborate data of SNe will be accumulated. There are a number of worldwide small telescope networks currently. Many international collaborations and active researches, on various subjects of time-domain astronomy and multi-messenger astronomy (MMA), are in process.

In upcoming era of LSST soon, with the great power of light gathering and the enormous data product, we are able to see deeper and further in the sky. It is obvious that time-domain astronomy and multi messenger astronomy will highly benefit by LSST. But small telescopes have merits of wide-fast sky coverage and available telescope time. Moreover, the worldwide network of telescopes are capable of rapid follow-up observation and constant monitoring of high cadence. With these merits, small telescope network such as IMSNG can play important role in transient research, complementing LSST at different depth and time scale.

Bibliography

Alsabti, A. W., & Murdin, P. 2017

Arbour, R. 2017, Transient Name Server Discovery Report, 2017-588, 1

Arcavi, I., et al. 2011, ApJ, 742, L18

Bai, Y., Zou, H., Liu, J., & Wang, S. 2015, ApJS, 220, 6

Barbary, K., et al. 2016, Zenodo

Becker, A. 2015, arXiv:1504.004

Bertin, E., & Arnouts, S., 1996, A&AS, 117,

Bertin, E., & Arnouts, S. 1996, A&AS, 117, 393

Bertin, E. 2010, arXiv:1010.063

Bertin, E. 2010, arXiv:1010.068

Bloom, J. S., et al. 2012, ApJ, 744, L17

Bianco, F. B., et al. 2014, ApJS, 213, 19

Botticella, M. T., et al. 2012, A&A, 537, A132

Bottinelli, L., Gouguenheim, L., Paturel, G., & de Vaucouleurs, G. 1984, A&AS, 56, 381

Branch, D. & Wheeler, J. C. 2017, ISBN 978-3-662-55052-6. Springer-Verlag GmbH Germany, 2017

Burns et al. 2011b, AJ, 141, 19

Burns et al. 2014, ApJ, 789, 32

Cao, Y., Kasliwal, M. M., Arcavi, I., et al. 2013, ApJ, 775, L7

Cardelli, J. A., Clayton, G. C., & Mathis, J. S. 1989, ApJ, 345, 245

Chambers, K. C., et al. 2017, VizieR Online Data Catalog, II/349

Chevalier, R. A., & Fransson, C. 2008, ApJ, 683, L135

Choi, C., & Im, M. 2017, JKAS, 50, 71

Choi, N., Park, W.-K., Lee, H.-I., Ji, Tae-Geun: Jeon, Y., & Im, Myungshin: Pak, S. 2015, JKAS, 48, 177

Choi, C., Im, M., Jeon, Y., & Ibrahimov, M., 2012, JKAS, 45, 7

Choi, C., Im, M., 2016, GRB Coordinates Network, 19358, 1

Chomiuk, L., Soderberg, A. M., Moe, M., et al. 2012, ApJ, 750, 164

Clocchiatti, A., & Wheeler, J. C. 1997, ApJ, 491, 375

Coelho, R. C. V., Calvão, M. O., Reis, R. R. R., & Siffert, B. B. 2015, European Journal of Physics, 36, 015007

Colgate, S. A., & McKee, C. 1969, ApJ, 157, 623

Crowther, P. A. 2007, ARA&A, 45, 177

Corsi, A., Ofek, E. O., Gal-Yam, A., et al. 2012, ApJ, 747, L5

Crts, N. M. A. 2018, Transient Name Server Discovery Report, 2018-116, 1

Dessart, L., et al. 2012, MNRAS, 424, 2139.

Drake, A. J., et al. 2009, ApJ, 696, 870

Drout, M. R., Soderberg, A. M., Gal-Yam, A., et al. 2011, ApJ, 741, 97

Ehgamberdiev, S. 2018, Nature Astronomy, 2, 349

Eldridge, J. J., Fraser, M., Smartt, S. J., Maund, J. R., & Crockett, R. M. 2013, MNRAS, 436, 774

Eldridge, J. J., Fraser, M., Maund, J. R., & Smartt, S. J. 2015, MNRAS, 446, 2689

Eldridge, J. J., Stanway, E. R., Xiao, L., et al. 2017, PASA, 34 e058,

Ensman, L., & Burrows, A. 1992, ApJ, 393, 742

Filippenko, A. V. 1997, ARA&A, 35, 309

Firth, R. E., Sullivan, M., Gal-Yam, A., et al. 2015, MNRAS, 446 3895,

Fitzpatrick, E. L. 1999, PASP, 111, 63,

Fremling, C., Sollerman, J., Taddia, F., et al. 2014, A&A, 565, A114

Folatelli, G., Phillips, M. M., Burns, C. R., et al. 2010, AJ, 139 120,

Fukugita, M., et al. 1996, AJ, 111, 1748

Gagliano, A., Izzo, L., Kilpatrick, C. D., et al. 2021, arXiv e-prints, arXiv:2105.09963.

Gal-Yam, A. 2012, Science, 337, 927,

Garnavich, P. M., Tucker, B. E., Rest, A., et al. 2016, ApJ, 820, 23

Gezari, S., Jones, D. O., Sanders, N. E., et al. 2015, ApJ, 804, 28

Gil de Paz, A., Boissier, S., Madore, B. F., et al. 2007, ApJS, 173 185,

Graur, O., Bianco, F. B., Huang, S., et al. 2017, ApJ, 837, 120

Gunn, J. E., & Stryker, L. L. 1983, ApJS, 52, 121

Han, W., Mack, P., Lee, C.-U., et al. 2005, PASJ, 57, 821

Hwang, S., Im, M., Taak, Y. C., et al. 2021, ApJ, 908, 113

Henden, A. A., et al. 2016, VizieR Online Data Catalog, 2336,

Hicken, M., et al. 2009, ApJ, 700, 331,

Hosseinzadeh, G., Sand, D. J., Valenti, S., et al. 2017, ApJ, 845, L11.

Howell, S. B., Ellis, R., Huchra, J., et al. 2006, Handbook of CCD astronomy, 2nd ed., Cambridge University Press.

Howell, D. A. 2011, Nature Communications, 2, 350,

Hsiao, E. Y., Conley, A., Howell, D. A., et al. 2007, ApJ, 663, 1187,

Im, M., Ko, J., Cho, Y., et al. 2010, JKAS, 43, 75,

Im, M., Choi, C., & Kim, K. 2015a, JKAS, 48, 207

Im, M., et al. 2015b, ApJS, 221, 22

Im, M., Yoon, Y., Lee, S.-K. J., et al. 2017, ApJ, 849, L16,

Im, M., Choi, C., Lee, S.-Y., et al. 2017, The Astronomer's Telegram, 10481

Im, M., Choi, C., Hwang, S., et al. 2019, JKAS, 52, 11,

Im, M. et al. 2021, in press

Jeon, Y., et al. 2016, JKAS, 49, 25

Jha, S. 2017, Transient Name Server Classification Report, 2017-870, 1

Jha, S. W., Maguire, K., & Sullivan, M. 2019, Nature Astronomy, 3, 706.

Kasen, D. 2010, ApJ, 708, 1025,

Kilpatrick, C. D., Takaro, T., Foley, R. J., et al. 2018, MNRAS, 480, 2072,

Kim, E., Park, W.-K., Jeong, H., et al. 2011, JKAS, 44, 115,

Kim, H.-J., Yoon, S.-C., & Koo, B.-C. 2015, ApJ, 809, 131,

Kim, S., et al. 2016, PASP, 128, 115004

Kim, J., Im, M., Choi, C., & Hwang, S. 2019, ApJ, 884, 103,

Kim, Y.-L., Kang, Y., & Lee, Y.-W. 2019, JKAS, 52, 181.

Klotz, A., Vachier, F., & Boër, M. 2008, Astronomische Nachrichten, 329, 275

Könyves-Tóth, R., et al. 2020, ApJ, 892, 121

Kurucz, R. L., 1993, ASPC, 44, 87

Lang, D., Hogg, D. W., Mierle, K., Blanton, M., & Roweis, S. 2010, AJ, 139, 1782

Lee, I., Im, M., & Urata, Y. 2010, JKAS, 43, 95

Li, W., Wang, X., Vinkó, J., et al. 2019, ApJ, 870, 12

Lim, J., Chang, S., Pak, S., et al. 2013, JKAS, 46, 161

Lu, N. Y., Hoffman, G. L., Groff, T., et al. 1993, ApJS, 88, 383. doi:10.1086/191826

Lyman, J. D., Bersier, D., & James, P. A. 2014, MNRAS, 437, 3848,

Lyman, J. D., Bersier, D., James, P. A., et al. 2016, MNRAS, 457, 328

Maoz, D., Mannucci, F., & Nelemans, G. 2014, ARA&A, 52, 107

Margutti, R., Parrent, J., Kamble, A., et al. 2014, ApJ, 790, 52

Marion, G. H., Brown, P. J., Vinkó, J., et al. 2016, ApJ, 820, 92

Maund, J. R. 2018, MNRAS, 476, 2629

Mazzali, P. A., Maurer, I., Valenti, S., Kotak, R., & Hunter, D. 2010, MNRAS, 408, 87

Miller, A. A., Cao, Y., Piro, A. L., et al. 2018, ApJ, 852, 100,

Minkowski, R. 1941, PASP, 53, 224

Moles, M., et al. 2008, AJ, 136, 1325

Nakar, E., & Sari, R. 2010, ApJ, 725, 904

Nakar, E., & Piro, A. L. 2014, ApJ, 788, 193

Neill, J. 2018, Transient Name Server Classification Report, 2018-129, 1

Noebauer, U. M., Kromer, M., Taubenberger, S., et al. 2017, MNRAS, 472, 2787

Nomoto, K. 1982, ApJ, 253, 798

Nugent, P. E., Sullivan, M., Cenko, S. B., et al. 2011, Nature, 480, 344

Onken, C. A., Wolf, C., Bessell, M. S., et al. 2019, PASA, 36, e033

Park, W.-K., et al. 2012, PASP, 124, 839

Perlmutter, S., et al. 1999, ApJ, 517, 565

Pereira, R., et al. 2013, A&A, 554, A27

Perryman, M. A. C., et al. 1997, A&A, 323L, 49P

Phillips, M. M., Lira, P., Suntzeff, N. B., et al. 1999, AJ, 118, 1766,

Piro, A. L., & Nakar, E. 2013, ApJ, 769, 67,

Piro, A. L., & Nakar, E. 2014, ApJ, 784, 85,

Piro, A. L., Haynie, A., & Yao, Y. 2021, ApJ, 909, 209,

Podsiadlowski, P., Joss, P. C., & Hsu, J. J. L. 1992, ApJ, 391, 246

Prentice, S. J., Mazzali, P. A., Pian, E., et al. 2016, MNRAS, 458, 2973

Prieto, J. L., Rest, A., & Suntzeff, N. B. 2006, ApJ, 647, 501,

Rabinak, I., & Waxman, E. 2011, ApJ, 728, 63,

Rabinak, I., Livne, E., & Waxman, E. 2012, ApJ, 757, 35,

Riess, A. G., et al. 1998, AJ, 116, 1009,

Salpeter, E. E. 1955, ApJ, 121, 161

Sana, H., de Mink, S. E., de Koter, A., et al. 2012, Science, 337, 444,

Sapir, N., & Waxman, E. 2017, ApJ, 838, 130

Scalzo, R., et al. 2014, MNRAS, 440, 1498

Scalzo, R. A., et al. 2019, MNRAS, 483, 628

Shappee, B. J., et al. 2014, ApJ, 788, 48

Shappee, B. J., et al. 2016, ApJ, 826, 144

Schawinski, K., et al. 2008, Science, 321, 223

Schlafly, E. F., & Finkbeiner, D. P. 2011, ApJ, 737, 103

Skrutskie, M. F., et al. 2006, AJ, 131, 1163

Smartt, S. J. 2009, ARA&A, 47, 63

Smartt. 2015, PASA, 32, e016

Smith, N., Li, W., Filippenko, A. V., & Chornock, R. 2011, MNRAS, 412, 1522

Soderberg, A. M., et al. 2008, Nature, 453, 469,

Stritzinger, M., et al. 2002, AJ, 124, 2100

Stritzinger, M. D., et al. 2018, A&A, 609, A135

Teffs, J., Ertl, T., Mazzali, P., Hachinger, S., & Janka, T. 2020, MNRAS, 492, 4369

Tonry, J. L., et al. 2012, ApJ, 750, 99

Troja, E., et al. 2017, Nature, 551, 71

Tully, R. B., & Fisher, J. R. 1988

Tully, R. B., Rizzi, L., Shaya, E. J., et al. 2009, AJ, 138, 323

Tutukov, A. V., & Yungelson, L. R. 1981, Nauchnye Informatsii, 49, 3

Valenti, S., Sand, D. J., & Tartaglia, L. 2017, Transient Name Server Discovery Report, 2017-866, 1

Van Dyk, S. D. 2017, Philosophical Transactions of the Royal Society of London Series A, 375, 20160277

Van Dyk, S. D., et al. 2017, The Astronomer's Telegram, 10485, 1

Van Dyk, S. D., et al. 2018, ApJ, 860, 90

Vinkó, J., et al. 2012, A&A, 546, A12

Wheeler, J. C., & Harkness, R. P. 1990, Reports on Progress in Physics, 53, 1467

Whelan, J., & Iben, Icko, J. 1973, ApJ, 186, 1007

Wolf, C., et al. 2003, A&A, 401, 73

Wolfinger, K., Kilborn, V. A., Koribalski, B. S., et al. 2013, MNRAS, 428, 1790. doi:10.1093/mnras/sts160

Woosley, S. E., Sukhbold, T., & Kasen, D. N. 2021, ApJ, 913, 145

Xiang, D., et al. 2019, ApJ, 871, 176

Yaron, O., Prialnik, D., Shara, M. M., & Kovetz, A. 2005, ApJ, 623, 398

Yoon, S.-C. 2015, PASA, 32, e015

Yoon et al. 2017, MNRAS, 470, 3970

Yoon, S.-C., Chun, W., Tolstov, A., Blinnikov, S., & Dessart, L. 2019, ApJ, 872, 174

요 약

초신성은 별의 최후로서 우주에서 가장 강력한 현상 중 하나다. 역사적으로 많은 관측과 이론적인 연구를 통해 많은 물리적 성질들이 드러났다. 그러나 초신성의 모든 성질들이 다 밝혀지지는 않았으며, 특히 모성에 대한 것은 더욱 많은 연구가 필요하다. 초신성의 초기 광도 곡선은 그들의 모성에 관한 많은 정보를 담고 있다. 폭발 직후 충격파로 가열된 복사의 흔적이 광도곡선에 새겨진다. IMSNG (가깝고 밝은, 초신성이 발생할 확률이 높은 은하들에 대한 집중적인 모니터링 탐사연구) 는 초신성의 초기 광도곡선을 얻어 모성에 대한 정보를 얻고 초신성에 대한 이해를 더욱 깊게 하고자 하여 시작되었다. 본 학위 연구 과제에서는 먼저 연구과정 중 시행한 IMSNG의 관측시스템을 구성한 내용을 서술한다. 그리고 IMSNG를 통해 초기 광도 곡선을 얻은 대상들에 대한 분석결과로서, Ia 형 초신성 SN 2018kp와 Ic 형 초신성 SN 2017ein, SN 2017gax에 대해 광도곡선을 통해 이들의 성질을 알아보고 모성에 대한 연구 결과를 제시한다.

첫째로, 가깝고 밝은 은하들 중 초신성이 나타날 확률이 높은 은하들을 선정하여 높은 빈도로 집중적인 관측을 하는 탐사연구를 기획하고 진행하였다. 그 중 호주 사이딩 스프링 천문대에 위치한 이상각 망원경에 2016년 설치한 SNUCAM-II의 특징과 성능을 조사하였다. 이 카메라는 넓은 파장 범위(0.3 μm to 1.1μm)를 고감도 (QE at $>$ 80% over 0.4 to 0.9μm)로 커버한다. SDSS $ugriz$ 필터와 13개의 중간너비 (50nm)의 필터들을 가지고 있어 외부은하 천체에서 태양계 천체에 이르는 다양한 대상에 대한 분광학적 에너지 분포도를 조사할 수 있다. 이상각 망원경과의 조합을 통해 한 픽셀에 대해 0.92 각초에 해당하는 스케일을 가지며, 관측 가능한 면적은 15.7 $\times$ 15.7 각분이다. 점광원에 대한 한계등급은 180초 노출로 g 필터에서는 19.91, z 필터에서는 18.20 AB 등급에 도달할 수 있다.

두번째로, 가까운 은하인 NGC 3367에서 2018년 1월 24일 발견된 보통의 성질을 가지는 Ia 형 초신성 2018kp 의 가시광선 영역 광도곡선을 분석한 결과를 제시한다. NGC 3367은 IMSNG에서 주요 대상으로서 매일 1 번 이상 관측하는 높은 빈도로 모니터링이 이루어지고 있었기에 발견 시기 주변의 유용한 조기광도곡선을 얻을 수 있었다. 조기광도곡선의 분석으로부터 이 초신성의 모성이 화구모형으로 잘 설명이 된다는 것을 볼 수

있었으며, SHE 모델들과의 비교로 부터 모성의 크기가 4 태양 반경보다 작을 것이라는 제한조건을 둘 수 있었다. 이로써 동반성으로 적색거성일 가능성을 배제할 수 있다. 그리고 단일 축퇴성 모델을 지지하는 것으로 예측된다. 여러 물리적 특성들을 보면 이 초신성은 잘 알려진 SN 2011fe 와 같은 보통의 Ia 형 초신성이라는 것을 알 수 있다. 또한 은하까지의 거리를 이 초신성의 광도곡선으로 구해본 결과 Tully-Fisher 방법으로 구한 기존의 거리인 50 Mpc과 일치하는 값을 얻었다.

세번째로, Ic 형 초신성 SN 2017ein 과 SN 2017gax의 광도곡선을 분석한 결과를 제시한다. Ic 형 초신성은 수소선과 헬륨선이 스펙트럼에 나타나지 않는 특성을 가지는 중력붕괴 초신성 중의 하나이다. 이런 특성은 수소나 헬륨이 진화과정에서 벗겨져 나간 별의 폭발 결과로 보고있다. Wolf-Rayet 별들이 질량손실과정을 효율적으로 잘 진행하기에 유력한 후보로 여겨진다. 그러나 이에 대한 직접적인 증거는 아직 발견되지 않았다. 또한 최근 연구 결과에서 헬륨선이 보이지 않는 관측 결과는 니켈의 혼합작용이 비효율적으로 일어나기 때문일 수도 있다는 의견이 있다. Ic 형 초신성의 조기광도곡선에서 색지수의 진화과정이 니켈의 혼합과정이 얼마나 효율적인지를 보여주며 이로써 헬륨이 거의 보이지 않지만 실제로 없는지에 대해 알아볼 수 있다는 모형이 제시되었다. SN 2017ein 과 SN 2017gax 은 각각 NGC 3938 과 NGC 1672 에서 2017년 발견된 Ic 초신성들로 탄소가 많은 것으로 여겨지는 Ic 형 초신성들이다. IMSNG를 통해 이들의 이른 시기 가시광선 영역 광도곡선을 얻었다. 이들을 분석한 결과 강력한 SHE의 흔적을 발견할 수는 없었으나 두 초신성의 모성이 비교적 작은 3 태양반경보다 작을 것이라는 제한 조건을 둘 수 있었다. 또한 이들의 이른 시기 색지수 변화 양상은 보통의 Ic와는 다르게 적색에서 청색으로 다시 청색으로 변화하는 형태를 보이는데, 모델과의 비교로 부터 니켈의 혼합정도가 약하거나 중간정도일 것으로 추정된다. 이는 소량일지라도 초신성의 모성에 헬륨이 존재할 수 있다는 것을 시사한다.

이 학위 연구 과정을 통해 초신성의 조기광도곡선을 얻어 모성에 대한 정보를 얻고자 IMSNG를 시작해 그 시설의 준비와 관측 과정을 수행하였으며 IMSNG를 통해 얻은 조기광도곡선을 통해 초신성들의 모성에 대한 의미있는 연구를 수행할 수 있었다. 대형 망원경의 시대가 도래하는 가운데 이러한 소형망원경을 이용한 연구 결과는 소형망원경의

장점을 새롭게 조명하는 의의를 가진다.

주요어: cosmology: observations – star: evolution – supernova: explosion– telescope: CCD camera – transient: survey

학 번: 2009-30868

감 사 의 글

2006년 석사과정 신입생 13명 중 한 사람으로 지구환경과학부 천문학과 석사과정을 입학했습니다. 그로부터 2021년까지 15년이 되었습니다. 아마 제가 가장 긴 대학원 생활을 한 사람이 아닐까 합니다. 그간 초인적인 인내심으로 봐주신 임명신 교수님께 머리 숙여 감사드립니다. 학위 논문의 긴박한 마감시간까지 너그럽고도 세심하게 봐주신 심사위원 분들께도 감사를 드립니다. 긴 시간을 지내며, 많은 도움을 받고 또 함께 했던 학생들과 직원분들 그리고 교수님들, 모두 제게 주신 도움과 지도에 감사드립니다.

마라톤 인생 살라고 늘 말씀하시던 아버지, 언제나 저를 여전히 아이처럼 봐주시고 감싸주시는 어머님께도 사랑과 감사를 드립니다. 형보다도 더 형 같은 동생에게도 고맙습니다. 그리고 저와 함께 하며, 삶의 이유가 되어주는 가장 가까운 저의 동반자 아내 영희와 딸 이엘이게 감사하다는 말을 남깁니다.

2021년 8월

최 창 수 드림